E.O. Paton Electric Welding Institute of the National Academy of Science of Ukraine
International Association «Welding»
LLC «Scientific Journals»

The Paton Welding Journal

02
2022

International Scientific-Technical and Production Journal
Founded in January 2000 (12 Issues Per Year)

EDITORIAL BOARD

Editor-in-Chief
I.V. Krivtsun — E.O. Paton Electric Welding Institute, Kyiv, Ukraine

Deputy Editor-in-Chief
S.V. Akhonin — E.O. Paton Electric Welding Institute, Kyiv, Ukraine

Deputy Editor-in-Chief
L.M. Lobanov — E.O. Paton Electric Welding Institute, Kyiv, Ukraine

Editorial Board Members

O.M. Berdnikova	E.O. Paton Electric Welding Institute, Kyiv, Ukraine
Chang Yunlong	School of Materials Science and Engineering, Shenyang University of Technology, Shenyang, China
V.V. Dmitrik	NTUU «Kharkiv Polytechnic Institute», Kharkiv, Ukraine
Dong Chunlin	China-Ukraine Institute of Welding of Guangdong Academy of Sciences, Guangzhou, China
A. Gumenyuk	Bundesanstalt für Materialforschung und –prüfung (BAM), Berlin, Germany
V.V. Knysh	E.O. Paton Electric Welding Institute, Kyiv, Ukraine
V.M. Korzhyk	E.O. Paton Electric Welding Institute, Kyiv, Ukraine
V.V. Kvasnytskyi	NTUU «Igor Sikorsky Kyiv Polytechnic Institute», Kyiv, Ukraine
Yu.M. Lankin	E.O. Paton Electric Welding Institute, Kyiv, Ukraine
S.Yu. Maksymov	E.O. Paton Electric Welding Institute, Kyiv, Ukraine
Yupiter HP Manurung	Smart Manufacturing Research Institute, Universiti Teknologi MARA, Shah Alam, Malaysia
M.O. Pashchin	E.O. Paton Electric Welding Institute, Kyiv, Ukraine
Ya. Pilarczyk	Welding Institute, Gliwice, Poland
V.D. Poznyakov	E.O. Paton Electric Welding Institute, Kyiv, Ukraine
U. Reisgen	Welding and Joining Institute, Aachen, Germany
I.O. Ryabtsev	E.O. Paton Electric Welding Institute, Kyiv, Ukraine
V.M. Uchanin	Karpenko Physico-Mechanical Institute, Lviv, Ukraine
Yang Yongqiang	South China University of Technology, Guangzhou, China

Managing Editor
O.T. Zelnichenko — International Association «Welding», Kyiv, Ukraine

Address of Editorial Board
E.O. Paton Electric Welding Institute, 11 Kazymyr Malevych Str. (former Bozhenko), 03150, Kyiv, Ukraine
Tel./Fax: (38044) 200 82 77, E-mail: journal@paton.kiev.ua
https://pwj.com.ua/en, https://patonpublishinghouse.com/eng/journals/tpwj

State Registration Certificate 24933-14873 ПР from 13.08.2021
ISSN 0957-798X, DOI: http://dx.doi.org/10.37434/tpwj

Subscriptions, 12 issues per year:
$384 — annual subscription for the printed (hard copy) version, air postage and packaging included;
$312 — annual subscription for the electronic version
(sending issues in pdf format or providing access to IP addresses).

The content of the journal includes articles received from authors from around the world in the field of welding, metallurgy, material science and selectively includes translations into English of articles from the following journals, published by PWI in Ukrainian:
- Automatic Welding (https://patonpublishinghouse.com/eng/journals/as);
- Technical Diagnostics & Nondestructive Testing (https://patonpublishinghouse.com/eng/journals/tdnk);
- Electrometallurgy Today (https://patonpublishinghouse.com/eng/journals/sem).

© E.O. Paton Electric Welding Institute of NASU, 2022
© International Association «Welding» (Publisher), 2022
© LLC «Scientific Journals», 2022

CONTENTS

ORIGINAL ARTICLES

V.M. Korzhyk, V.Yu. Khaskin, Yao Yuhui, O.I. Demianov, D.V. Stroganov, V.O. Shcheretskyi
INFLUENCE OF ACCOMPANYING COMPRESSING AIR FLOW ON THE COATING STRUCTURE AND PROPERTIES IN PLASMA-ARC SPRAYING BY CONSUMABLE CURRENT-CONDUCTING WIRE* 3

O.P. Voronchuk, O.P. Zhudra, T.V. Kaida, V.O. Kochura, L.M. Kapitanchuk, L.M. Ieremeieva
INFLUENCE OF THE COMPOSITION OF CHARGE COMPONENTS IN FLUX-CORED STRIPS OF C–Fe–Cr–Mo ALLOYING SYSTEM ON CHEMICAL AND STRUCTURAL HETEROGENEITY OF THE DEPOSITED METAL* 11

V.A. Matviichuk, V.M. Nesterenkov, O.M. Berdnikova
ADDITIVE ELECTRON BEAM TECHNOLOGY FOR MANUFACTURE OF METAL PRODUCTS FROM POWDER MATERIALS* 16

K.A. Yushchenko, B.O. Zaderii, I.S. Gakh, G.V. Zviagintseva, T.O. Aleksiienko
DESTRUCTION OF WELDED JOINTS OF SINGLE-CRYSTAL HIGH-TEMPERATURE NICKEL ALLOYS AT TENSILE TESTING* 26

Yu.S. Borysov, N.V. Vihilianska, I.A. Demianov, A.P. Murashov, O.P. Gryshchenko
STUDIES OF COATINGS PRODUCED BY HIGH-VELOCITY OXY-FUEL SPRAYING USING CERMET POWDER BASED ON FeMoNiCrB AMORPHIZING ALLOY* 33

D.I. Malysheva, N.A. Vynogradov, V.Yu. Sysoyev
DESIGN FEATURES OF MOBILE RAIL WELDING MACHINES FOR FLASH BUTT WELDING* 37

M.I. Grechanyuk, V.G. Grechanyuk, I.M. Grechanyuk, V.O. Chornovol
STRUCTURE AND CORROSION PROPERTIES OF COPPER- AND TUNGSTEN-BASED COMPOSITE MATERIALS, PRODUCED BY HIGH-RATE EVAPORATION-CONDENSATION** 43

O.O. Makhnenko, O.V. Makhnenko
CALCULATED ESTIMATION OF LOAD-CARRYING CAPACITY OF THE MAIN SPAN BEAMS OF THE E.O. PATON BRIDGE ACROSS THE DNIPRO IN KYIV BY NONDESTRUCTIVE TESTING RESULTS*** 48

Correction to: Improvement of the mechanical properties and corrosion resistance of laser welds on thick duplex plates by laser cladded buttering. A. Straße, A. Gumenyuk, M. Rethmeier (The Paton Welding J., 1, 18–21, 2022) 54

*Translated Article(s) from «Automatic Welding», No. 2, 2022.

**Translated Article(s) from «Electrometallurgy Today», No. 4. 2021.

***Translated Article(s) from «Technical Diagnostics & Nondestructive Testing», No. 4, 2021.

https://doi.org/10.37434/tpwj2022.02.01

INFLUENCE OF ACCOMPANYING COMPRESSING AIR FLOW ON THE COATING STRUCTURE AND PROPERTIES IN PLASMA-ARC SPRAYING BY CONSUMABLE CURRENT-CONDUCTING WIRE

V.M. Korzhyk[1], **V.Yu. Khaskin**[1], **Yao Yuhui**[2], **O.I. Demianov**[1], **D.V. Stroganov**[1], **V.O. Shcheretskyi**[1]

[1]E.O. Paton Electric Welding Institute of the NASU
11 Kazymyr Malevych Str., 03150, Kyiv, Ukraine
[2]Shenzhen Hanzhizi Technology Co., Ltd. 6th Floor, Building B,
Bantian International Center, 5 Huancheng South Road, Longgang District, Shenzhen,
Guangdong, China

ABSTRACT

The paper is devoted to studying the technological features of plasma-arc spraying by consumable current-conducting wire-anode. The relevance of applying such a process is related to the possibility of spraying directly by atomization of wires without the need to make powder materials from them. Experimental verification of the results of mathematical prediction of the influence of annular protective flow of compressed air, accompanying the particle-loaded plasma jet, on the results of plasma-arc spraying by compact wire anodes was performed. The key role of increasing this flow rate above 20 m^3/h for improvement of the spay-deposited coating formation and quality was established. In spraying of coatings from compact wires porosity decreased with increase of the values of flow rates of accompanying air flow G_2, and achievement of this parameter values within 0.5–2.5 %. Conducted experiments allow producing porefree coatings in spraying with wires from M2 copper, Kh20N80 nichrome, NP1 nickel, AMg63 aluminium-magnesium alloy. Studying these experimental results showed that at increase of the rate of accompanying protective air flow G_2 from 0 to 40 m^3/h, the loss of alloying elements (C, Mn) during spraying by steels wires of 65G and 70 grades decreases by 30–40 % on average. Increase of the parameter of rate G_2 of the air flow accompanying the particle-loaded plasma jet influences improvement of the coating bond strength and wear resistance. So, at G_2 = 20–40 m^3/h the bond strength at tearing off of coatings from steel 70 along the normal reaches 60–70 MPa, and that of coatings from M2 copper is 40–55 MPa. Wear resistance of coatings under the conditions of boundary friction and resistance at cavitation wear increases at G_2 increase from 0 to 40 m^3/h, which is manifested in reduction of such wear from 1.35 to 0.32 mg/min.

KEYWORDS: plasma-arc spraying, compact wires-anodes, accompanying flow, material utilization factor, coating bond strength, wear resistance

INTRODUCTION

At present, there exists a certain number of promising industrial technologies of functional coating deposition [1]. In particular, such technologies are used, which allow spraying compact metal and flux-cored wires by plasma-arc process. At application of such a process arc melting of the wire takes place with formation of liquid metal drops in argon atmosphere [2]. For consumable-wire plasma-arc spraying the plasma arc which runs between the tungsten cathode and the wire, is blown by an intensive accompanying air flow. The argon flow around the arc is fed through a plasma nozzle with small flow rate. Air is fed into the gap between the plasma and protective nozzles at considerable rate [3]. The features of such a process consist in that wire material melting and atomization take place in a shielding argon atmosphere, and melt fragmentation and disperse particle acceleration occur in the plasma jet, compressed by a accompanying air flow, coming out of an annular gap between the plasmatron nozzles. It allows ensuring minimum evaporation losses of wire material and optimum fractional composition of the sprayed dispersed phase, spraying material particles reaching a subsonic speed at the moment of collision with the base, high volume concentration of the sprayed particles and minimum opening angle of the particle-loaded plasma flow [4]. However, there arises the risk of molten wire material saturation with oxygen and nitrogen from the air at its introduction into the zone of the electric arc impact, which may cause disturbance and air penetration into the high-temperature arc. The molten metal drops are also influenced by the conditions of protection of the particle-loaded plasma jet at the working distance between the plasmatron and the sprayed surface [5]. As a result, the chemical composition of the deposited coating may differ considerably from that of the wire fed into the arc. In order to eliminate this phenomenon, it is necessary to create reliable protection of not only the wire fusion zone, but of the entire particle-loaded plasma jet. Solving this problem, as well

Copyright © The Author(s)

as improvement of service characteristics of the coatings, applied by the described method, and strength of their bond with the base is an urgent task.

The objective of the work is studying the influence of shielding gas flow accompanying the particle-loaded plasma jet on the process of plasma-arc spraying by a consumable wire-anode and on the service properties of the coatings which are deposited using this process.

THEORETICAL ANALYSIS OF THE ACCOMPANYING FLOW INFLUENCE ON THE PLASMA FLOW CHARACTERISTICS

The following tasks were solved to achieve the defined objective: analysis of the computational modeling of the process and influence of the rate of the accompanying gas flow on its characteristics, experimental studies of the influence of the accompanying flow of shielding gas on the material utilization factor, as well as such service properties of the coating as porosity, bond strength, and wear resistance.

According to the technological scheme of the process of plasma-arc spraying by wire-anode, the refractory cathode forms an annular electrode nozzle of radius R_n with the channel wall (Figure 1), through which the plasma gas is fed at rate G_1 and the total arc current I flows. Plane $z = 0$ was taken as the start of the computational domain, assuming that it is located at a certain distance from the cathode working edge. It allowed at the first stage excluding the near-cathode processes from consideration and regarding the arc plasma flow in this plane as axisymmetric and unidimensional along OZ axis, and, thus correctly assigning the initial boundary conditions. It is assumed that shielding gas with flow rate G_2 is fed through annular channel R_1–R_2 as an axisymmetric flow at angle α to the system axis of symmetry. Anode wire is located at distance Z_2 from the start of computational domain. It is assumed that the anode current decreases smoothly in the region of anode binding and then (at $z > Z_2$) currentless inertial movement of gas takes place.

At theoretical analysis of the processes of gas heating and movement at plasma-arc atomization of the wire-anode the computational domain can be conditionally divided into three regions (Figure 1): *1* — arc plasma flow region inside the plasmatron nozzle ($0 \le z < Z_1$); *2* — region of external flow of arc plasma and its interaction with the shielding gas flow ($Z_1 \le z \le Z_2$); *3* — region of inertial movement without the current plasma ($z > Z_2$).

The following assumptions were taken for mathematical description of the processes occurring at formation and flowing out of the plasma jet from the plasmatron nozzle:

- the considered plasma system has cylindrical symmetry, and the occurring processes are considered stationary;
- shielding gas is fed as an axisymmetric flow through the annular channel;
- shielding gas flow in the channel is considered laminar and is described by model dependencies;
- plasma is in the state of local thermodynamic equilibrium, plasma self-radiation is volumetric;
- joule heat release is the main mechanism of plasma heating (the work of the pressure forces and viscous dissipation can be neglected), and energy transfer in the arc column takes place due to heat conductivity and convection (natural convection is ignored);

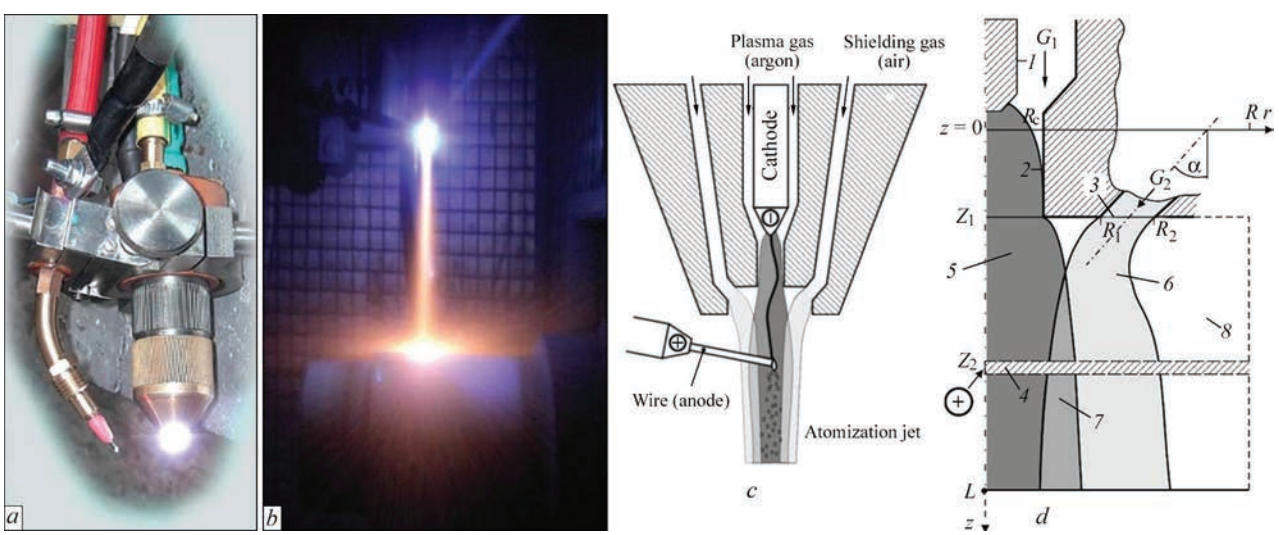

Figure 1. Plasmatron appearance (*a*), visualization (*b*) and technological scheme of the process and scheme of computational mathematical model of heating and movement of gas at plasma-arc spraying of coatings by current-conducting wire-anode: *1* — cathode; *2* — nozzle; *3* — blowing gas feeding channel; *4* — wire-anode' *5* — arc plasma; *6* — blowing gas (accompanying gas flow); *7* — mixing zone; *8* — external gas atmosphere

● plasma flow is viscous, subsonic, flow mode is turbulent;

● external magnetic fields are absent.

At construction of the physico-mathematical model it was assumed that refractory cathode forms an annular electrode nozzle of radius R_n with the channel wall (Figure 1), through which the plasma gas is fed at flow rate $G_1 = 2\pi \int_0^{R_c} \rho u r\, dr$, and the total arc current $I = 2\pi E \int_0^{R_\sigma(z)} \sigma r\, dr$ flows. Plane $z = 0$ located at a certain distance from the cathode working edge, was taken as the start of the computational domain. It allows regarding the arc plasma flow in this plane as axisymmetric and unidimensional along axis *OZ*. Shielding gas is fed at rate G_2 through annular channel R_1–R_2 as an axisymmetric flow at angle α to the system axis of symmetry. Anode wire is located at distance Z_2 from the start of the computational domain. It is assumed that in the region of anode binding the arc current smoothly decreases and furtheron (at $z > Z_2$) currentless inertial movement of gas takes place.

The system of magnetohydrodynamic (MHD) equations in the approximation of turbulent boundary layer for time-average values of plasma temperature and velocity is as follows [3, 4]:

$$\frac{\partial}{\partial z}(\rho u) + \frac{1}{r}\frac{\partial}{\partial r}(r\rho\bar{v}) = 0; \quad (1)$$

$$\rho\left(u\frac{\partial u}{\partial z} + \bar{v}\frac{\partial u}{\partial r}\right) = \frac{1}{r}\frac{\partial}{\partial r}\left(r\bar{\eta}\frac{\partial u}{\partial r}\right) - \frac{\partial}{\partial z}\left(p + \mu_0\frac{H^2}{2}\right); \quad (2)$$

$$\rho C_p\left(u\frac{\partial T}{\partial z} + v\frac{\partial T}{\partial r}\right) = \frac{1}{r}\frac{\partial}{\partial r}\left(r\bar{\chi}\frac{\partial T}{\partial r}\right) + \frac{j^2}{\sigma} - \psi, \quad (3)$$

where T is the average plasma temperature; $\bar{v} = (\rho v + \rho' v')/\rho$, v is the mean radial velocity, r is the mean plasma density, r' and v' are the fluctuations of the density and radial velocity; u is the mean axial velocity of plasma; p is the pressure, which within the plasma-forming channel is defined as $p = p_{ext} - \int_z^{Z_1} \frac{dp_c}{dz} dz + \mu_0 E \int_r^{R_c} \sigma H\, dr$, and in the open area of the arc discharge ($z > Z_i$) $p = p_{ext} + \mu_0 E \int_r^{R_c} \sigma H\, dr$; $C_p(T, p)$ is the specific heat capacity at constant pressure; s is the plasma electric conductivity; j is the vector of electric current density; $\psi(T, p)$ is the bulk density of self-radiation power; $\bar{\eta}$ and $\bar{\chi}$ are the total coefficients of dynamic viscosity and heat conductivity of plasma, which are the sums of molecular and turbulent viscosity and heat conductivity, respectively; μ_0 is the universal magnetic constant; $H = \frac{1}{r} E \int_0^r \sigma r\, dr$ is the azimuthal component of the arc current magnetic field.

The system of MHD equations together with the accompanying relationships, *k-e* model of turbulence and boundary conditions completely defines the thermal and gas-dynamic characteristics of turbulent plasma flow, both in the arc and inertia areas of the flow. These equations make up the base of a unified mathematical model, suitable for calculation of spatial distributions of temperature and velocity of the subsonic plasma flows, which in our case are generated by the plasmatron with a partially open arc in the presence of an accompanying gas flow around the arc.

The developed physico-mathematical model and software for its computer realization were used to conduct numerical analysis of the characteristics of the subsonic turbulent flow of argon plasma, which is generated by the plasmatron with a consumable wire-anode at different modes of its operation (Figures 2, 3). This analysis showed that flow rate G_2 of the gas flow accompanying the particle-loaded plasma one, has a rather substantial impact on velocity u and temperature T of the latter. With increase of value G_2, values u and T grow in direct proportion. It is rational to use the accompanying gas flow with rates G_2 = 20 m^3/h and higher.

Numerical studies in work [3, 4] showed that blowing of the plasma jet by an accompanying flow of cold gas prevents its expansion and essentially increases its extent. So, at a distance of approximately 50 mm from the plasmatron nozzle edge, the width of the plasma flow core, not blown by shielding gas, approximately two times exceeds the respective value for a jet, surrounded by the flow [3]. Argon concentration in the high-temperature core of the plasma jet, surrounded by the accompanying shielding gas, remains high at considerable distances (close to 0.5 at 150 mm distance from the nozzle edge) [4]. As a result, the protected plasma jet preserves its momentum and energy much longer, and practically does not mix with the accompanying gas.

Thus, numerical calculations given in works [3, 4], show that the technological measure of applying an accompanying flow, which compresses the plasma jet, essentially influences the characteristics of particle-loaded plasma jet. A comprehensive assessment of the rationality of application of this technique during plasma-arc spraying with wire-anodes requires a more complete study of its influence both on distribution of plasma temperature and velocity, and on the structure

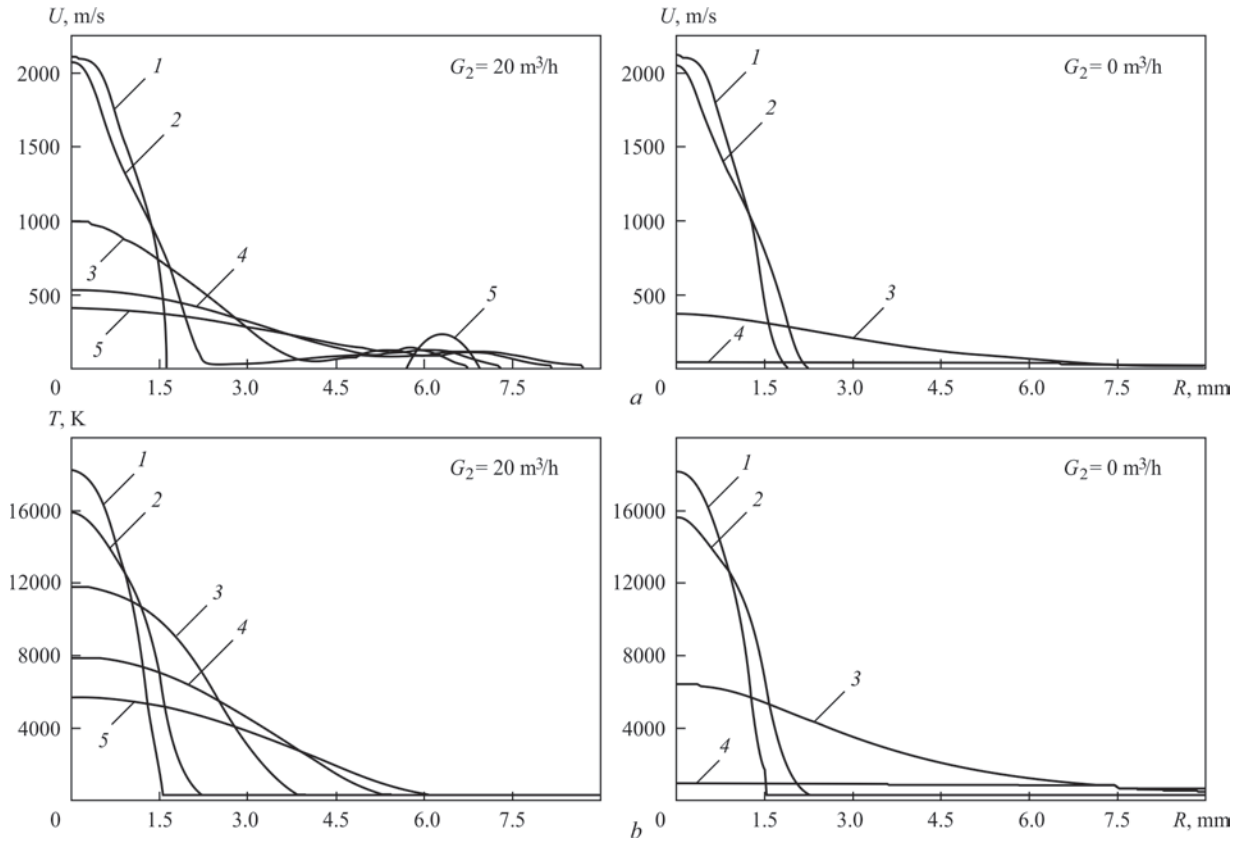

Figure 2. Radial distributions of plasma velocity (*a*) and temperature (*b*) at I = 200 A and G_1 = 1 m³/h in the following regions [3, 4]: *1* — nozzle edge (z = 3 mm); *2* — wire-anode region (z = 9.3 mm); *3* — z = 150 mm; *4* — z = 250 mm

and properties of the spray-deposited coatings from different types of wire materials.

EXPERIMENTAL PROCEDURE

Technological experiments on determination of the influence of the accompanying flow on service properties of the produced coatings were performed, proceeding from the above calculation-based recommendations. A laboratory facility based on Plazer 30PL-W unit (upgraded batch-produced UN-126 unit) was developed for this purpose [6]. This unit was further fitted with equipment to study the micrometallurgical processes, which included thermal vision and original video optic systems for recording the spraying process [7–10]. Carbon steel of grade 20 (GOST 16523–97) was used as the base. Plates from this steel were sprayed with compact wires of 1.2–1.6 mm diameter from steel 70 (GOST 103–2006), 65G (GOST 103–2006), 18Kh15N3M (GOST 103–2006), Kh20N80 nichrome (GOST 12766.1–90), M2 copper (GOST 859–2001) and AMg63 aluminium alloy (GOST 4784–97). Wire from commercial NP1 nickel (GOST 492–2006) was spray-deposited on high-strength VCh 35 cast iron with globular graphite (GOST 7293–85).

The value of breaking stress in "coating-base" composition at normal tear, determined by the "conical pin" procedure, was used to assess the strength of coating bond $\sigma_{b.s}$ with the base [11]. Tribotechni-

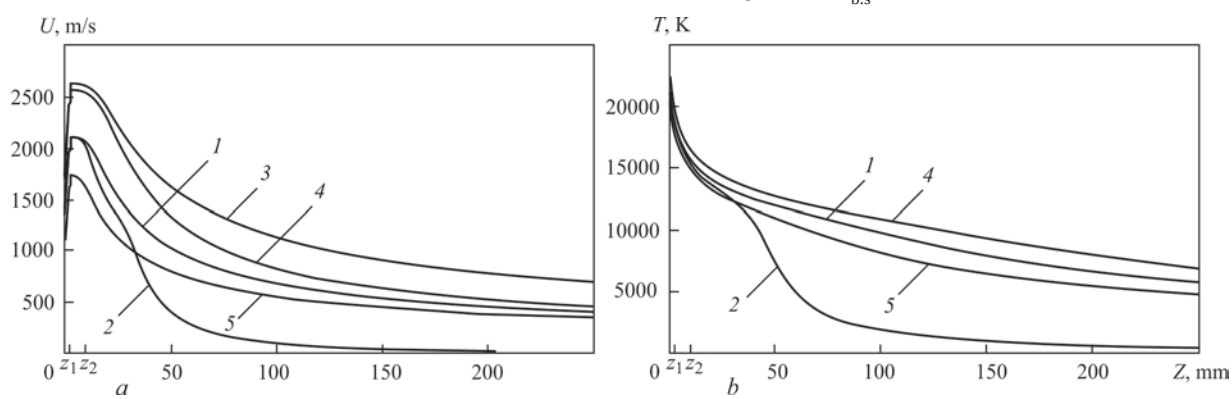

Figure 3. Longitudinal changes of plasma velocity (*a*) and temperature (*b*) on the jet axis at different modes of plasmatron operation [3, 4]: *1* — I = 200 A, G_1 = 1 m³/h, G_2 = 20 m³/h; *2* — I = 200 *A*, G_1 = 1 m³/h, G_2 = 0 m³/h; *3* — I = 200 *A*, G_1 = 1.5 m³/h, G_2 = 20 m³/h; *4* — I = 260 *A*, G_1 = 1 m³/h, G_2 = 20 m³/h; *5* — I = 160 *A*, G_1 = 1 m³/h, G_2 = 20 m³/h

cal testing of coatings was conducted using friction testing machine 2070 CMT-1 under the conditions with limited lubrication and without it by the schemes of "coated disc–block (SCh-20 cast iron, steel 40Kh, copper-asbestos alloy, steel 45)", "cylinder (SChNMD cast iron) — ring (coating)", "plane (steel 20 — after carbonization, bronze, SCh-20) — coating"; "disc–plane" (Amsler procedure), as well as reciprocating motion with 61 mm amplitude, V = 0.023 m/s, P = 11 MPa [12]. Metallographic investigations of the coatings were conducted in optical microscopes MIM-7, MIM-8, Neophot-23 at up to ×1000 magnification. The composition of the etchants and modes of etching of the polished samples were selected according to the recommendations [13].

The cavitation wear resistance was determined by the method of magnetostrictive vibration. Test samples were prepared in keeping with the requirements of ASTM G32-10 standard. Testing was conducted at the frequency of 20 ± 0.1 kHz, amplitude of 55 ± 3 μm and 500 kW power of ultrasonic generator. Water was used as the test solution.

ANALYSIS OF EXPERIMENTAL RESULTS

Compressed air was used as accompanying shielding gas with flow rate G_2 from 0 to 40 m^3/h. First, the impact of rate G_2 on the parameters of the technological mode of spraying was determined, in particular, on the material utilization factor (MUF). For this purpose, value G_2 was varied, leaving other parameters constant: flow rate of plasma gas (argon) G_1 = = 1.5 m^3/h; arc current I = 200 A; spraying distance of 160 mm; wire-anode from steel 70 (1.6 mm diameter). MUF value was determined by the following formula: MUF = $(m_c/m_w)\cdot 100$ %, where m_c is the weight of the coating spray-deposited per a unit of time; m_w is the weight of the wire-anode, spray-deposited per a specified unit of time. It was found that with increase of value G_2 from 0 to 20 m^3/h, MUF is also gradually increased from 52 to 72%. At $G_2 \geq 20$ m^3/h MUF stops growing and a remains stable value of the order of 72 %.

Proceeding from the results of further experiments, it was found that at increase of flow rate values G_2 from 0 to 40 m^3/h, the degree of loss of alloying elements (C, Mn) during spraying with steel 70 wire, decreases by 30–40 % on average, compared with the initial chemical composition of this wire. When spraying with wire from 18Kh15N3M stainless steel, the content of such alloying elements as Ni, Mo, W in the coating remains practically unchanged, compared to their content in the sprayed wire. It was found that at values G_2 = 20–40 m^3/h, oxygen content in the melting zone at the wire-anode tip after an abrupt breaking of the arc is close to these values in spray-deposited coatings for such wire grades with elements with a higher affinity to oxygen, as Kh20N80 and AMg63, and in the case of spraying with copper wire M2 this value in the coating is smaller by 1.5–2.0 times on average.

Spray-deposited coatings, produced by plasma-arc atomization of copper wire-anode of M2 grade, have a dense layered structure, characteristic for plasma coatings (Figure 4). Porosity value mainly is within 0.5–2.5 %. A tendency to lowering of this value with increase of flow rates of the accompanying air flow was established. At values G_2 = 20–40 m^3/h, porefree coating were produced, alongside optimization of such parameters as current, plasma gas flow rate and pressure and spraying distance, at spraying with wires from copper M2 (Figure 4), stainless steel (Figure 5), nichrome, nickel (Figure 6) and AMg63 aluminium-magnesium alloy.

Thickness of the lamellas in the coating is equal to 8–30 μm on average, the lamella interfaces are defectfree (Figure 5). This is an indirect indication of formation of a metallurgical bond between them and realization of a totality of microwelding processes between the earlier solidified layers in the coating and spray-deposited molten particles. Formation of such a bond is possible only under the conditions of increase of the velocity of particle-loaded plasma jet at its acceleration by the accompanying flow. Another indication of the effectiveness of the influence of accom-

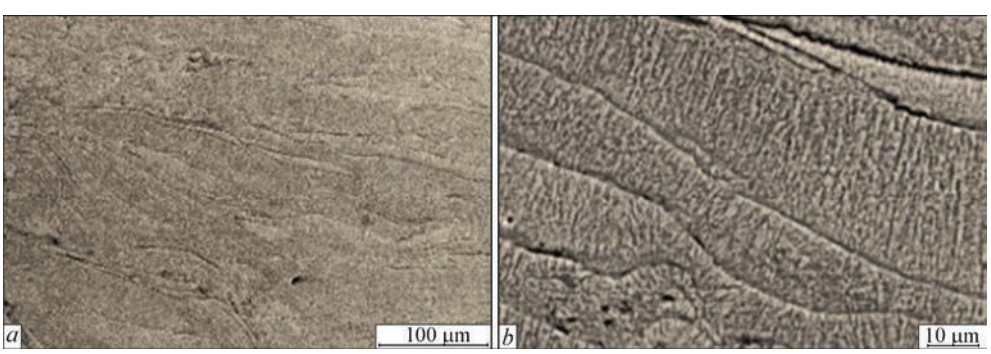

Figure 4. Microstructure of porefree coating from copper wire of grade M2: *a* — before; *b* — after etching

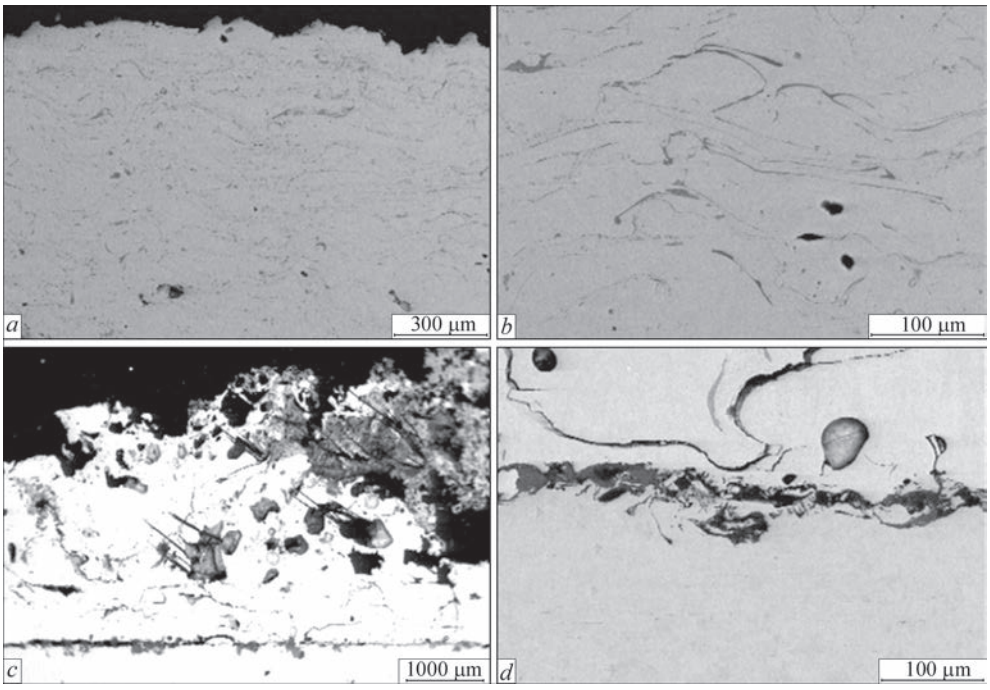

Figure 5. Layer microstructure of coatings, produced by plasma-arc atomization by moving wire-anode from 18Kh15N3M stainless steel, at the following rates of accompanying air flow, compressing the plasma: G_2 = 40 m^3/h (*a*, *b*) and G_2 = 5 m^3/h (*c*, *d*)

panying flow on the process of plasma-arc spraying is minimizing pore formation in the produced layers, which can be clearly traced at comparison of the results of spraying with different rates G_2 of the accompanying air flow (Figure 6).

At determination by the pin procedure of bond strength of coatings spray-deposited by the studied plasma-arc process, it was found that the value of this characteristic is influenced by rate G_2 of the accompanying air flow, coming out of the annular gap between the plasmatron nozzles. Figure 7 shows an example of the influence of rate G_2 of accompanying air flow on bond strength $\sigma_{b.s}$ of coatings produced by plasma-arc spraying with wires (1.6 mm diameter) from steel 70 and M2 copper (tearing along the normal, base is steel 20).

The bond strength of spray-deposited coatings is also influenced by current *I* of the plasma arc. At plasma-arc spraying of wire from steel 70, with increase of current the bond strength $\sigma_{b.s}$ of coatings (tearing along a normal, base is steel 20) first rose, and then somewhat decreased by the end. Spraying was conducted with the following mode parameters: plasma gas (argon) flow rate G_1 = 1.5 m^3/h; rate of accompanying air flow, G_2 = 40 m^3/h; spraying distance of 160 mm. Comparison of the influence of G_1 and G_2 parameters on bond strength showed that the latter of them is more significant.

It is found that the technological parameter of rate G_2 of accompanying annular air flow, coming out of the annular gap between the plasmatron nozzles, influences the increase of coating wear resistance under the conditions of boundary friction and cavitation wear. So, for instance, an increase of coating wear resistance under the conditions of boundary friction and cavitation wear was

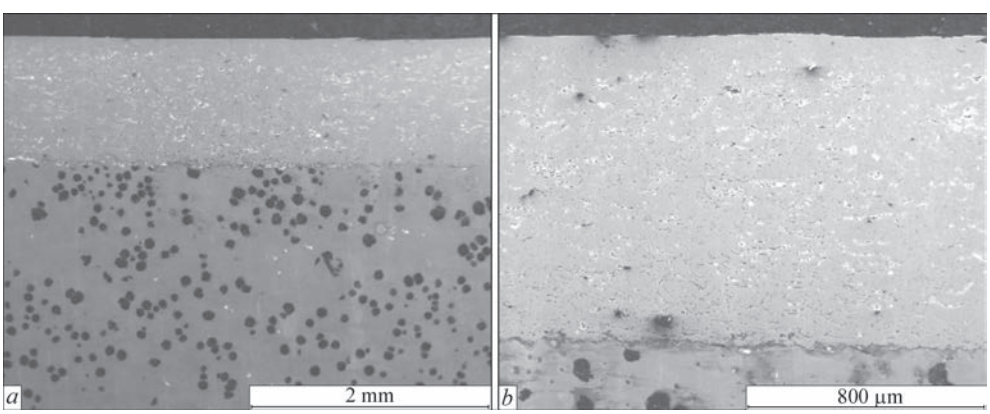

Figure 6. Porefree coating produced by plasma-arc spraying of NP1 nickel wire (base is high-strength cast iron with VCh 35 globular graphite)

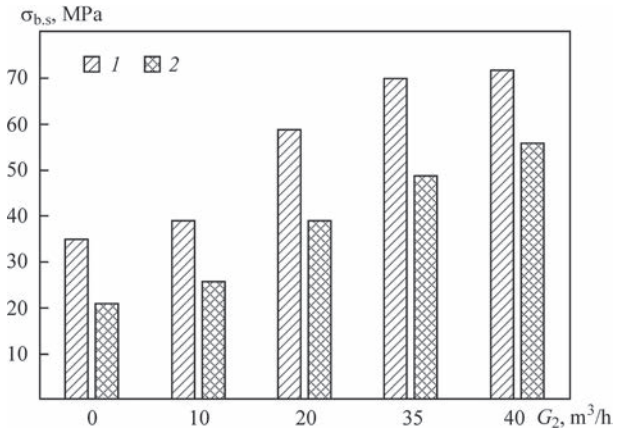

Figure 7. Influence of accompanying air flow rate G_2 on coating bond strength $\sigma_{b.s}$ (steel 20): *1* — steel 70; *2* — copper M2

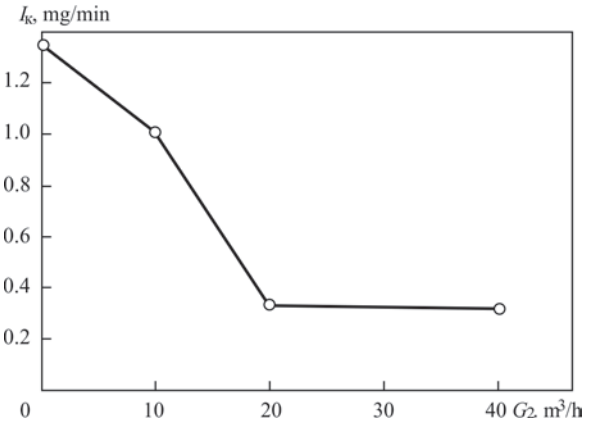

Figure 8. Change of cavitation wear intensity I_c, depending on accompanying flow rate G_2

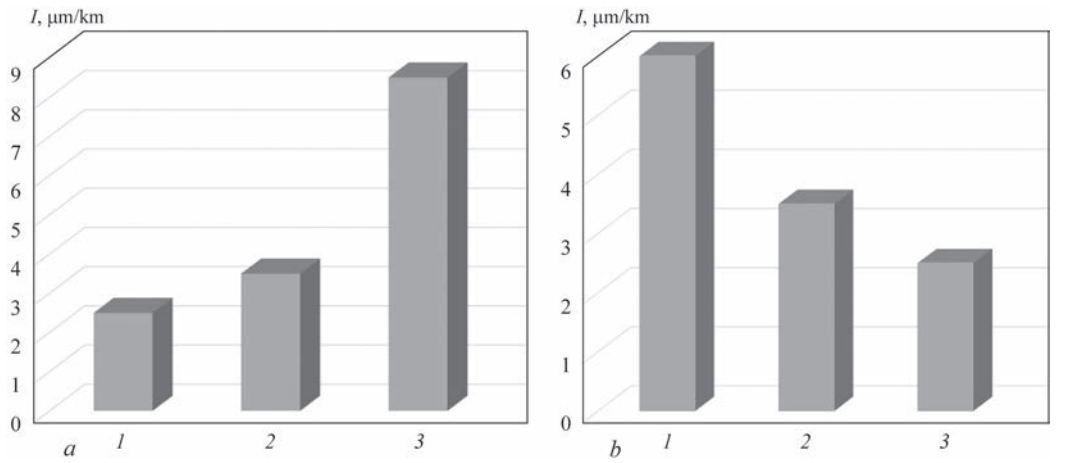

Figure 9. Wear intensity *I* of plasma coatings produced by atomization of wires-anodes (rider is steel 40X; load *P* = 10 MPa; velocity *V* = 1 m/s; lubrication is oil *HC*20, 30 drops/min; friction machine 2070 CMT-1): *a* — from steels 65G (1) and 70 (2) at G_2 = 20 m^3/h, compared to steel 20 after carburization (3); *b* — from steel 70 at accompanying flow rates: G_2 = 5 m^3/h (1); 20 (2); 40 (3)

revealed at G_2 increase from 0 to 35–40 m^3/h (Figure 8). This is attributable to increase of adhesion strength between the coating layers at G_2 increase.

Conducting tribotechnical testing of coatings deposited by plasma-arc atomization of compact metal wires-anodes, showed the positive influence of increase of accompanying flow rate G_2. Under the conditions of friction with limited lubrication by the schemes of coated disc – block, steel 40X)", it was found that coatings from steels 65G and 70 deposited at G_2 = 20 m^3/h have 60–70 % higher resistance than that of steel 20 after carbonization (Figure 9, *a*). At decrease of accompanying flow rate (G_2 = 5 m^3/h) the coating wear resistance decreases, and at increase of the rate (G_2 = 40 m^3/h), it increases (Figure 9, *b*).

CONCLUSIONS

1. Experimental verification of the results of mathematical prediction of the influence of annular shielding flow of compressed air, accompanying the particle-loaded plasma jet, on the results of plasma-arc spraying by compact wires-anodes showed the key role of increasing this flow rate above 20 m^3/h for improvement of formation and quality of the sprayed coatings.

2. A tendency was established to lowering of porosity of sprayed-deposited coatings with increase of the values of accompanying air flow rate G_2 and reaching this parameter values within 0.5–2.5 %, and at G_2 = 35–40 m^3/h porefree coatings were obtained at spraying by wires from M2 copper, Kh20N80 nichrome, NP1 nickel, and AMg63 aluminium-magnesium alloy.

3. It was confirmed that at increase of accompanying shielding air flow rate G_2 from 0 to 20–40 m^3/h, the loss of alloying elements (C, Mn) during spraying by steel wires of grades 65G and 70 decreases by 30–40 % on average. Here, oxygen content in the melting zone at the tip of the wire-anode after an abrupt breaking of the arc for such wire materials as Kh20N80 and AMg63 with elements with a higher affinity to oxygen, is close to these values in spray-deposited coatings, and for the case of spraying by copper wire M2 this value in the coating is smaller by 1.5–2 times on average.

4. The influence of increase of the parameter of rate G_2 of air flow accompanying the particle-loaded plasma jet, on improvement of bond strength and wear resistance of coatings was established. It is shown that at G_2 = 20–40 m^2/h the bond strength at coating tearing from steel 70 along a normal reaches 60–70 MPa, and that of M2 copper coating is 40–35 MPa. An increase of wear resistance of coatings was found under the conditions of boundary friction and cavitation wear at G_2 increase from 0 to 35–40 m^2/h.

REFERENCES

1. Babiak, Z., Wenz, T., Engl, L. (2006) Fundamentals of thermal spraying, flame and arc spraying. *Modern Surface Technology*, Chapter **8**, 119–136. DOI: https://doi.org/10.1002/3527608818.ch8
2. Kawaguchi, Y., Miyazaki, F., Yamasaki, M. et al. (2017) Coating qualities deposited using three different thermal spray technologies in relation with temperatures and velocities of spray droplets. *Coatings*, 27(**7**), 1–10. DOI: https://doi.org/10.3390/coatings7020027
3. Kharlamov, M.Yu., Krivtsun, I.V., Korzhik, V.N. et al. (2007) Mathematical model of arc plasma generated by plasmatron with anode wire. *The Paton Welding J.*, **12**, 9–14.
4. Kharlamov, M.Yu., Krivtsun, I.V., Korzhik, V.N. et al. (2008) Effect of the type of concurrent gas flow on characteristics of the arc plasma generated by plasmatron with anode wire. *The Paton Welding J.*, **6**, 14–18.
5. Ab, O. (2015) Atmospheric plasma spray process and associated spraying jet. In: *Proc. of Intern. Conf. on Thermal Spraying*, **77**, 012008, 35–42.
6. Korzhik, V.N., Korob, M.F. (2012) Mechanized line Plazer 30PL-W for plasma-arc wire spraying of coatings on large-sized parts of “shaft” type. *Svarshchik*, 86(**4**), 13–15 [in Russian].
7. Gulyaev, I.P., Gulyaev, P.Yu., Korzhik, V.N. et al. (2015) Experimental investigation of process of plasma-arc wire spraying. *The Paton Welding J.*, **3–4**, 36–41.
8. Gulyaev, I., Dolmatov, A., Kharlamov, M. et al. (2015) Arc-plasma wire spraying: An optical study of process phenomenology. *J. of Thermal Spray Technology*, 24(**11**), 1566–1573.
9. Dolmatov, A.V., Gulyaev, I.P., Gulyaev, P.Yu., Iordan, V.I. (2016) Control of dispersed-phase temperature in plasma flows by the spectral-brightness pyrometry method. In: *Proc. of IOP Conf. Series: Materials Science and Engineering*, **110**, 012057, 1–6.
10. Dolmatov, A.V., Gulyaev, I.P., Jordan, V.I. (2015) The optical control system of dispersed phase properties in thermal spray process. In: *Proc. of IOP Conf. Series: Materials Science and Engineering*, **81**, 012041. DOI: https://doi.org/10.1088/1757-899X/81/1/012041
11. Lunev, V.M., Nemashkalo, O.V. (2010) Adhesion characteristics of coatings and methods of their measurement. *Fizicheskaya Inzheneriya Poverkhnosti*, 8(**1**), 64–71 [in Russian].
12. Ashok Kumar, R.T., Nagendra, I.J., Uvaraj, Naik (2021) A study on tribological behavior of thermally sprayed coatings. *J. of Advancements in Material Engineering*, 6(**1**), 1–11.
13. Kovalenko, V.S. (1981) *Metallographic reagents:* Refer. Book. Moscow, Metallurgiya [in Russian].

ORCID

V.M. Korzhyk: 0000-0001-9106-8593,
V.Yu. Khaskin: 0000-0003-3072-6761,
O.I. Demianov: 0000-0001-7184-3839,
D.V. Stroganov: 0000-0003-4194-764X,
V.O. Shcheretskyi: 0000-0002-8561-4444

CONFLICT OF INTEREST

The Authors declare no conflict of interest

CORRESPONDING AUTHOR

V.Yu. Khaskin
E.O. Paton Electric Welding Institute of the NASU
11 Kazymyr Malevych Str., 03150, Kyiv, Ukraine
E-mail: khaskin1969@gmail.com

SUGGESTED CITATION

V.M. Korzhyk, V.Yu. Khaskin, Yao Yuhui, O.I. Demianov, D.V. Stroganov, V.O. Shcheretskyi (2022) Influence of accompanying compressing air flow on the coating structure and properties in plasma-arc spraying by consumable current-conducting wire. *The Paton Welding J.*, **2**, 3–10.

JOURNAL HOME PAGE

https://pwj.com.ua/en

Received: 10.12.2021
Accepted: 31.03.2022

https://doi.org/10.37434/tpwj2022.02.02

INFLUENCE OF THE COMPOSITION OF CHARGE COMPONENTS IN FLUX-CORED STRIPS OF C–Fe–Cr–Mo ALLOYING SYSTEM ON CHEMICAL AND STRUCTURAL HETEROGENEITY OF THE DEPOSITED METAL

O.P. Voronchuk, O.P. Zhudra, T.V. Kaida, V.O. Kochura, L.M. Kapitanchuk, L.M. Ieremeieva

E.O. Paton Electric Welding Institute of the NASU
11 Kazymyr Malevych Str., 03150, Kyiv, Ukraine

ABSTRACT

It is generally known that wear resistance of the deposited layer in the above-mentioned alloys depends on the reinforcing phase characteristics, its concentration and qualities of the matrix alloy. The methods of X-ray structural, metallographic analyses and X-ray microanalysis of metal of 500Kh30M type deposited by flux-cored strips revealed the dependence of the concentration, form, orientation, phase components and integral hardness of the carbides on the method of adding chromium as the main carbide forming element, to the charge. It is found that the maximum concentration of the carbide phase of up to 80–90 % in the deposited layer is achieved at addition of Cr_3C_2 chromium carbide to the flux-cored strip charge. Complex carbide systems — $(CrFe)_7C_3$ are mainly present in the deposited metal for all the samples. Molybdenum does not form any separate carbide compounds, but it is a component in carbides of $(Cr_{2.5}Fe_{4.2}Mo_{0.2})C_3$ type. High concentration of the carbide component leads to carbide washout, in connection with a considerable reduction of the matrix alloy. Optimal concentration of the carbide phase in metal of 500X30M type deposited with flux-cored strip, is achieved by adding a carbide forming element — chromium to the electrode material charge in the proportion of 15–25 % chromium carbide and 75–85 % ferrochrome.

KEY WORDS: flux-cored strip, chromium carbide, ferrochome, carbides, hardness, microstructure, matrix, concentration

INTRODUCTION

Wear-resistant surfacing of parts by flux-cored wires or strips is one of the effective and widely used methods of their strengthening and increasing their service life [1–3]. A steadily growing demand to increase the equipment operability in different industries, makes it necessary to continuously improve the compositions and quality of electrode and filler materials for surfacing.

A wide range of parts of the mining and metallurgical complex are traditionally surfaced, using electrode (filler) materials, which allow producing deposited metal of the type of high-chromium cast iron, resistant to abrasive and gas-abrasive wear [4–6]. The effectiveness of such materials largely depends on the carbide phase concentration in the deposited metal, its orientation, structural components, as well as quality of the alloy matrix [7–9].

The above-mentioned characteristics of the deposited metal can differ essentially, depending on the chemical composition of the electrode and filler materials proper, as well as the composition of the charge of flux-cored wires and strips.

The objective of this work is investigation of the influence of carbide-forming components of the charge of PL-AN180 flux-cored strip on the structure and phase components of the deposited metal and development of optimal composition of the flux-cored strip to produce a coating resistant to abrasive and gas-abrasive wear.

INVESTIGATION PROCEDURES AND EQUIPMENT

Methods of X-ray structural, and metallographic analyses and X-ray microanalysis were used to study the deposited metal of 500Kh30M type. Hardness measurement was conducted in M-400 microhardness meter of LECO Company, and JAMP-9500F and DRON-UM1 instruments were used for X-ray spectral, electronic spectroscopy and X-ray diffraction studies. Microstructural studies were conducted using Neophot-32 microscope.

Sample surfacing was performed by electric arc method, using self-shielded flux-cored strip PL-AN180, which allows producing deposited metal of the following chemical composition, wt.%: 4.5 C; 30 Cr; 1 Mo. PL-AN180 flux-cored strip is used for producing wear-resistant bimetal plates of 5 to 30 mm thickness. Such bimetal plates are readily transformed into a wide range of parts for different metal structures, by laying-out, cutting and bending, thus extending their serviceability. These plates can be used to manufacture hoppers, conveyors, pipelines, dump truck bodies, lining of crushing and grinding

Copyright © The Author(s)

equipment, as well as other parts and structures which are exposed to intensive abrasive wear [10].

In C–Fe–Cr–Mo alloying system mainly chromium carbides are present as the reinforcing phase, and an iron-based alloy is the matrix. It was important to determine how the concentration of carbides and other characteristics of the deposited layer are affected by the form, in which the main carbide-forming element, namely chromium, is added to the charge. High-carbon ferrochrome of grade FKh900 and chromium carbide were used for chromium addition. The latter is close to stoichiometry of Cr_3C_2 carbide in its chemical composition.

EXPERIMENTAL INVESTIGATIONS AND THEIR RESULTS

Flux-cored strips of 16.5×4.0 mm cross-section with different content of chromium and ferrochrome were prepared for experiments:

- sample 1 – 50 % chromium carbide + 50 % FeCr;
- sample 2 – with Cr carbide, but without FeCr;
- sample 3 – with FeCr, but without chromium carbide.

Here, other charge components remained unchanged.

Surfacing was conducted in two layers to eliminate the influence of base metal in the deposited metal

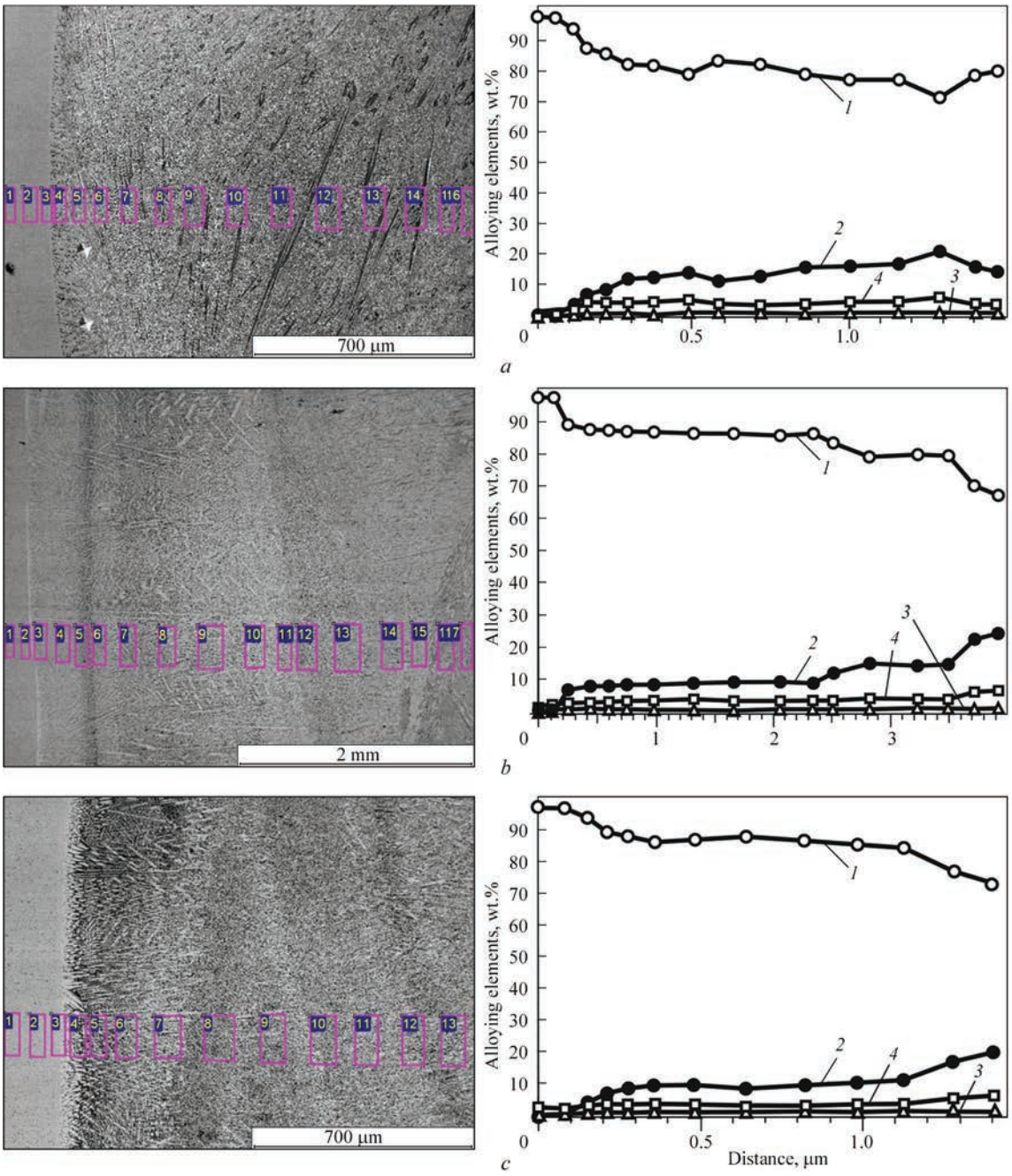

Figure 1. Distribution of alloying elements by deposited layer height: *a* — sample No.1; *b* — 2; *c* — 3 (*1* — iron; *2* — chromium; *3* — molybdenum; *4* — carbon)

working zone. Depending on the composition of the charge used, the ratio of phase components changed, and, thus the integral hardness of the deposited metal near the fusion line in the first and second layer. Carbide dimensions and orientation were also studied. In samples No.1 the volume fraction of the carbides is equal to 63–65 vol.%, integral hardness by the deposited layer height is 5400, 8100, and 9500 MPa, respectively, form factor is 1.32, the carbides are disoriented. Carbide orientation is of lanceolate shape, predominantly directed along the heat dissipation line; carbides are of a hexagonal shape disoriented. In samples No.2 the volume fraction of carbides is 85–90 vol.%, integral hardness is 6100; 7200 and 10800 MPa, form factor is 3.57, carbides are predominantly located along the heat dissipation line. In samples No.3 the carbide volume fraction is equal to 40–45 %, integral hardness by deposition height is 5620; 6860 and 7100 MPa, respectively, form factor is equal to 1.19, carbides of lanceolate shape are oriented predominantly along the heat dissipation line, those of hexagonal shape are disoriented. Form factor grows at increase of chromium carbide content in the flux-cored strip charge.

Figure 1 shows the curves of alloying element distribution by the deposited layer height, which correspond to a change of integral hardness.

An optimum combination of the deposited layer wear resistance and toughness is determined by the type and quantity of the carbide phase, its orientation, as well as matrix structure. At an anomalously large fraction of the carbide phase and coincidence of its orientation with the direction of the abrasive flow, the deposited metal wear resistance decreases, as “washing out” of the carbide component from the matrix takes place which is depleted in alloying elements.

Conducted investigations showed that the transition zone along the line of fusion with the first layer of the deposited metal in all the cases is characterized by formation of the solid solution dendrites and carbide eutectics in the interdendritic space. Dimensions of the zone with dendritic form of crystallization vary as follows: 50–370 μm in sample No.1, 40–120 μm in sample No.2 and 60–308 μm in sample No.3. Typical structure of base metal – deposited layer transition zone of all the studied samples is shown in Figure 2.

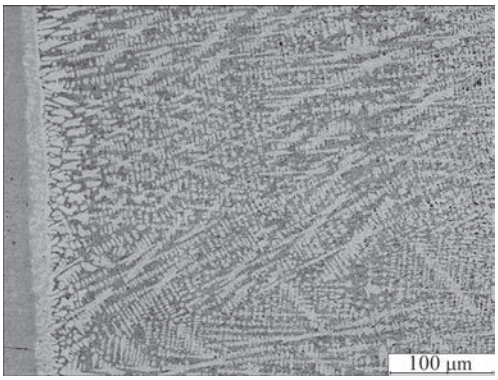

Figure 2. Typical structure of base metal — deposited layer transition zone

The method of X-ray structural analysis was used to determine the quantitative phase composition, type and parameters of the deposited metal crystalline lattice. The structure of the studied types of the deposited metal is an austenitic matrix and carbide phase of Cr_7C_3, as well as carbides with somewhat changed parameters, that suggests complex alloying of the carbide, the formula of which is similar to the calculation formula $(Cr_{2.5}Fe_{4.3}Mo_{0.2})C_3$ from the international base of crystallographic data Pcpdfwin [11]. No Mo carbides were found. It is obvious that independent carbides do not form at Mo addition to the alloy in the quantity of approximately 1 %, and molybdenum liquates into Cr carbides.

The method of X-ray microanalysis was used to conduct investigations of alloying element distribution in the structural components and to determine their chemical composition. At transition from the first to the second layer of the deposited metal the nature of structure formation changes: the second layer structure is an austenitic matrix with carbides of different shape and orientation with their gradual coarsening towards the deposited metal surface.

A typical structure of the deposited metal second layer in sample No.1 is given in Figure 3, *a*, and chemical composition of its phase components — in Table 1; that of sample No.2 — in Figure 3, *b* and

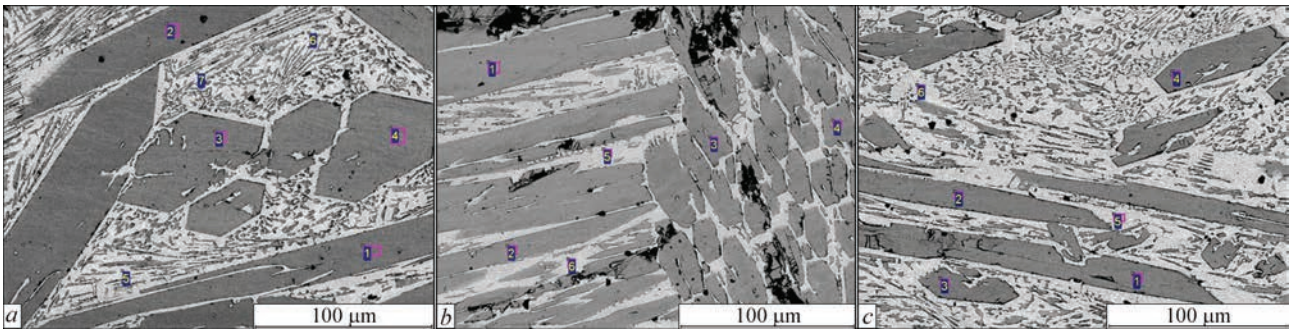

Figure 3. Sample microstructure: No.1 (*a*), No.2 (*b*), No.3 (*c*)

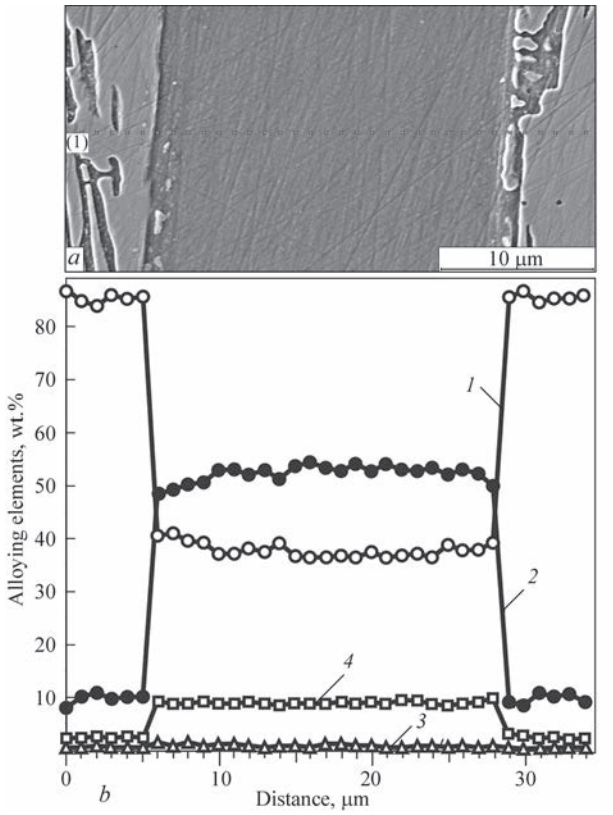

Figure 4. Structure (*a*) and distribution of alloying elements in $(FeCr)_7C_3$ carbide (*b*): *1* — iron; *2* — chromium; *3* — molybdenum; *4* — carbon

in Table 2; of sample No.3 — in Figure 3, *c* and in Table 3.

DISCUSSION OF THE RESULTS

Presented data demonstrate reduction of the carbide-forming element in the austenitic component of the deposited metal, depending on the composition of the charge, used at surfacing.

Table 1. Weight fraction of elements in the points of analysis of sample No.1

Analysis point	C	Al	Si	Cr	Fe	Mo	Total
1	8.94	0.04	0.02	53.56	36.35	1.08	100.00
2	9.23	0.00	0.00	51.37	38.59	0.81	100.00
3	9.00	0.02	0.01	53.75	36.42	0.80	100.00
4	9.16	0.05	0.00	53.66	36.23	0.89	100.00
5	3.16	1.12	0.75	8.75	85.45	0.78	100.00
6	2.58	1.00	0.77	9.75	85.57	0.34	100.00
7	2.11	0.59	0.83	8.15	86.87	1.44	100.00

Table 2. Weight fraction of elements in points of analysis of sample No.2

Analysis point	C	Al	Si	Cr	Fe	Mo	Total
1	8.87	0.00	0.09	53.73	36.38	0.93	100.00
2	8.91	0.00	0.04	53.35	36.81	0.88	100.00
3	9.04	0.04	0.00	54.76	35.39	0.77	100.00
4	9.11	0.05	0.03	54.91	35.18	0.72	100.00
5	2.11	1.31	1.15	7.28	87.10	1.04	100.00
6	2.30	1.32	0.92	7.78	86.62	1.06	100.00

Table 3. Weight fraction of elements in points of analysis of sample No.3

Analysis point	C	Al	Si	Cr	Fe	Mo	Total
1	9.28	0.02	0.04	53.24	36.02	1.40	100.00
2	8.80	0.00	0.01	52.27	38.16	0.75	100.00
3	8.73	0.00	0.05	52.63	37.49	1.10	100.00
4	9.22	0.01	0.00	52.88	36.80	1.10	100.00
5	2.12	0.65	0.60	11.98	83.89	0.75	100.00
6	2.23	0.69	0.64	10.27	85.16	1.01	100.00

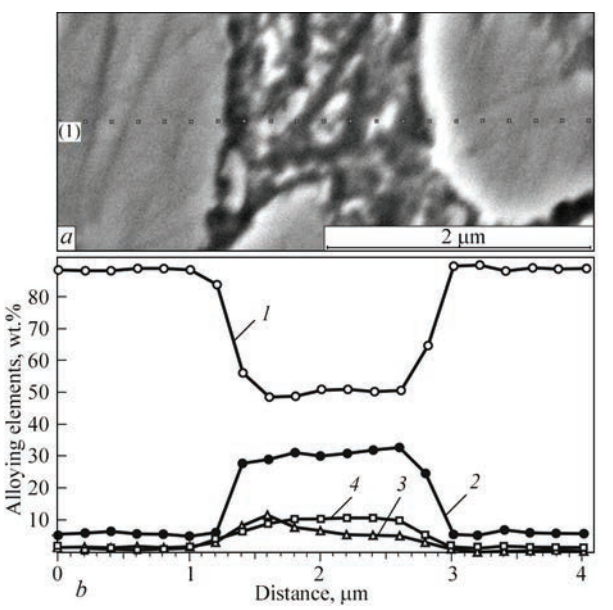

Figure 5. Structure (*a*) and distribution of alloying elements in $(Cr_{2.5}Fe_{4.2}Mo_{0.2})C_3$ carbide (*b*): *1* — iron; *2* — chromium; *3* — molybdenum; *4* — carbon

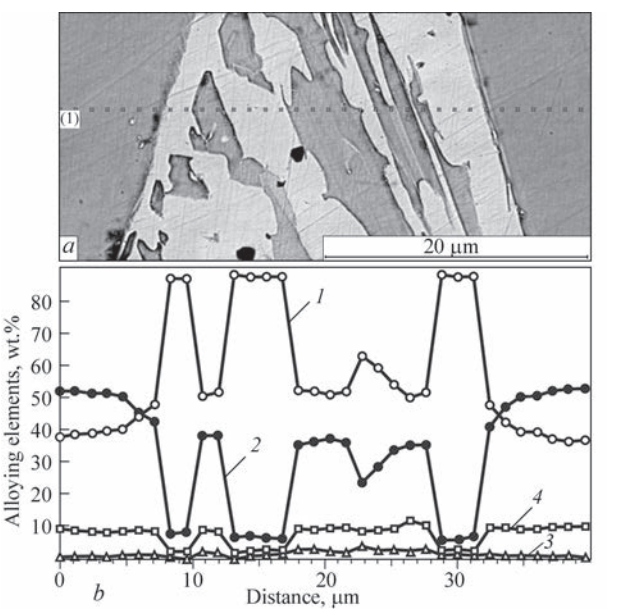

Figure 6. Structure (*a*) and distribution of alloying elements in the deposited metal structural components (*b*): *1* — iron; *2* — chromium; *3* — molybdenum; *4* — carbon

Hardness in structural components (P = 100 g) in the studied types of the deposited metal practically does not change: Aus + fine C — 6100–6700 MPa (it is practically impossible to separate austenite and dispersed carbides); hardness of lanceolate carbides — 16500–16800 MPa, of those of hexagonal shape — approximately 11500–11800 MPa.

The composition and degree of alloying of $(FeCr)_7C_3$ carbides was determined, wt.%: 8.9–9.1 C; 52–53 Cr; 37.2–38.5 Fe; 0.2 Mo, and of those of another composition, wt.%: 9.5 C; 31.5–32.0 Cr; 50.8–52.0 Fe; 2.8–6.0 Mo that practically confirms presence of a carbide, described by $(Cr_{2.5}Fe_{4.2}Mo_{0.2})C_3$ formula. Figures 4 and 5 also show typical curves of linear distribution of alloying elements in $(FeCr)_7C_3$ and $(Cr_{2.5}Fe_{4.2}Mo_{0.2})C_3$ carbides. It should be noted that $(Cr_{2.5}Fe_{4.2}Mo_{0.2})C_3$ carbide is heterogeneous by its structure (sample No.1).

Hard wear-resistant alloys are heterogeneous by their structure. Figure 6 (sample No.2) shows typical curves of alloying element distribution in the deposited metal structural components, which demonstrate the heterogeneity of the structure and composition of phase components, and clearly show the diffusion-induced redistribution of alloying elements in the zone of transition from the matrix to the carbide.

CONCLUSIONS

Investigations showed that the optimum concentration of the carbide phase in the metal, deposited with flux-cored strip of PL-AN180 type, is achieved due to adding carbide-forming element — chromium to the electrode material charge in the proportion of 15–25 % chromium carbide and 75–85 % proportion of ferrochrome. Complex carbides of $(CrFe)_7C_3$ system are mainly present in the deposited metal for all the samples. Molybdenum does not form separate carbide compounds, but is a component in carbides of $(Cr_{2.5}Fe_{4.2}Mo_{0.2})C_3$ type.

REFERENCES

1. Ryabtsev, I.A., Senchenkov, I.K., Turyk, E.V. (2015) *Surfacing. Materials, technologies, mathematical modeling*. Gliwice, Wydawnictwo Politechniki Śląskiej.
2. Ryabtsev, I.A. (2005) High-efficiency wide-layer surfacing using electrode wires and strips (Review). *The Paton Welding J.*, **6**, 36–41.
3. Pokhodnya, I.K., Shlepakov, V.N., Maksimov, S.Yu., Ryabtsev, I.A. (2010) Research and developments of the E.O. Paton Electric Welding Institute in the field of electric arc welding and surfacing using flux-cored wire (Review). *The Paton Welding J.*, **12**, 34–42.
4. Zhudra, A.P., Voronchuk, A.P. (2012) Cladding flux-cored strips (Review). *The Paton Welding J.*, **1**, 34–38.
5. Kuskov, Yu.M., Bogajchuk, I.L., Chernyak, Ya.P., Evdokimov, A.I. (2013) Electroslag surfacing of parts, made of high-chrome cast iron, using cast iron shot. *The Paton Welding J.*, **8**, 46–48.
6. Kuskov, Yu.M., Evdokimov, A.I. (2014) Electroslag surfacing of wear-resistant alloyed cast irons. *Uprochniayushchie Tekhnologii i Pokrytiya*, **10**, 21–24 [in Russian].
7. Livshits, L.S., Grinberg, N.A., Kurkumelli, E.G. (1969) *Principles of alloying of deposited metal*. Moscow, Mashinostroenie [in Russian].
8. Kudinov, V.D., Filimonov, B.V., Shevnov, S.A., Netesa, I.V. (1985) Surfacing with composite alloy of parts of metallurgical equipment. *Avtomatich. Svarka*, **5**, 48–50 [in Russian].
9. Voronchuk, A.P. (2009) Effect of concentration of hard particles on gas-abrasive wear resistance of composite alloy. *The Paton Welding J.*, **8**, 43–44.
10. Zhudra, A.P., Voronchuk, A.P., Petrov, A.V., Kochura, V.O. (2012) Technology, equipment and materials for manufacture of sheet lining elements. *Svarochn. Proizvodstvo*, **11**, 40–43 [in Russian].
11. (1973) Powder Diffraction File Search Manual. *Alphabetical Listing Inorganic*. Publication SMA-23, USA.

CONFLICT OF INTEREST

The Authors declare no conflict of interest

CORRESPONDING AUTHOR

O.P. Voronchuk
E.O. Paton Electric Welding Institute of the NASU
11 Kazymyr Malevych Str., 03150, Kyiv, Ukraine
E-mail: voronchuk@aranei.com

SUGGESTED CITATION

O.P. Voronchuk, O.P. Zhudra, T.V. Kaida, V.O. Kochura, L.M. Kapitanchuk, L.M. Ieremeieva (2022) Influence of the composition of charge components in flux-cored strips of C–Fe–Cr–Mo alloying system on chemical and structural heterogeneity of the deposited metal. *The Paton Welding J.*, **2**, 11–15.

JOURNAL HOME PAGE

https://pwj.com.ua/en

Received: 12.11.2021
Accepted: 31.03.2022

https://doi.org/10.37434/tpwj2022.02.03

ADDITIVE ELECTRON BEAM TECHNOLOGY FOR MANUFACTURE OF METAL PRODUCTS FROM POWDER MATERIALS

V.A. Matviichuk, V.M. Nesterenkov, O.M. Berdnikova

E.O. Paton Electric Welding Institute of the NASU
11 Kazymyr Malevych Str., 03150, Kyiv, Ukraine

ABSTRACT

The aim of the work is to create additive electron beam technology for layer-by-layer manufacture of metal parts from powder materials. To carry out investigations, an experimental model of additive equipment was made, a software and hardware platform for additive manufacturing was designed, technological methods and modes of printing products of a set shape with predicted strength properties were invented. Applying the additive method, 25 experimental samples for further tests were printed. For each of the products, the speed of beam movement, its power and dynamic focusing current were determined. The influence of basic parameters of the technological process of surfacing on the formation and features of the surface structure and chemical composition of the samples were studied. It was found that the chemical composition of products corresponds to the composition of raw materials except for the content of aluminium, which is underestimated by 0.6–1.96 % relative to the chemical composition of the powder. To eliminate this drawback, it is necessary to maintain the aluminium content in titanium alloy powders at the highest level. According to the results of investigations in the created equipment, according to computer models, the products of industrial and medical purpose were printed, the printing modes of which are optimized. From the powders of titanium alloys, the models of stator blades of a gas turbine aircraft engine, human skull implant and bioprosthesis were manufactured.

KEYWORDS: additive technologies; 3D printer, electron beam surfacing, metal powder, titanium alloy, chemical composition, surface microrelief

INTRODUCTION

Innovative technologies of layer-by-layer manufacturing of products by the method of rapid prototyping open up new opportunities for the manufacture of parts of a set shape with predicted properties.

The process of creating products by such a method with the use of an electron beam is relatively new, but it successfully opened up great prospects for the manufacture of a wide range of industrial and medical products. It is based on the operation of layer-by-layer melting of metals in vacuum using electron beam. This approach is distinguished by a quick transition to the manufacture of three-dimensional products directly from the system of automated designing with the ability of using a wide range of metals and alloys, including refractory and chemically active ones [1].

In Ukraine and in the world, creation of additive technologies for growing products by electron beam surfacing is urgent. As far as domestic equipment does not exist, it is relevant to create the equipment and software for it to realize additive manufacturing oriented to be introduced at the enterprises of the aerospace industry and turbine building, and also for the needs of biomedical branch.

The specialists of the E.O. Paton Electric Welding Institute of the NAS of Ukraine carried out investigations on the development of technologies and equipment for additive manufacturing of metallic parts by the method of rapid prototyping.

OBJECT, AIM, TASKS AND RESULTS OF INVESTIGATIONS

The results of previous research works showed the possibility of creating industrial equipment for electron beam melting of metal powder materials, as well as the ability of manufacturing products of a complex shape by an additive method [2].

The authors set the aim of developing additive electron beam technology for manufacturing products of aerospace industry and turbine building and create an experimental model of additive equipment.

The object of investigations was electron beam technologies for growing products using metallic powder materials. The basic tasks are the development of an experimental model of additive equipment and software, creation of printing technology, manufacture of experimental samples, studies of their properties and manufacture of industrial parts.

As a result of the project realization, a unique equipment for realization of additive electron beam manufacturing was created, which is oriented on the introduction at domestic enterprises of aerospace industry and turbine building: JSC “Motor Sich”, SE “LRZ” Motor, “SE EDB “Pivdenne” and “Zorya-Mashproekt” Gas Turbine Research and Devel-

Copyright © The Author(s)

opment Complex. The equipment is also relevant for the needs in the biomedical industry and mechanical engineering.

TECHNOLOGY OF ELECTRON BEAM SURFACING

The technology of electron beam surfacing is similar to the technology of selective laser sintering, which is widely used in industry. Its main difference consists in using an electron beam as a power source instead of a laser. The technology is based on the possibility of using a high-power electron beam for melting of a metal powder in a vacuum chamber with the formation of successive layers that repeat the contours of a digital model of a product. Unlike the technologies of laser sintering, electron beam surfacing allows increasing the efficiency due to a high power of the guns and electromagnetic unlike electromechanical beam scanning [2].

The technology provides an opportunity to maintain a thermostable process of manufacturing parts throughout the whole manufacturing cycle. The temperature in the bed, where a product is created, is maintained as a result of action of electron beam as a power source. Before surfacing, the powder layer is heated to a temperature of about 700–1000 °C, which allows creating parts with lower residual stresses caused by a gradient of temperatures between already cooled and still hot layers. The thermostable process makes it impossible or significantly reduces the formation of cracks and shaping defects.

In addition, a complete remelting of a metal powder allows manufacturing monolithic products, which provides the maximum strength. As to mechanical properties, finished products almost do not differ from cast parts.

In the process of printing, the device reads data from a file, containing a three-dimensional digital model of a product and creates successive layers of the powder material. The contours of layers are formed by a focused electron beam, which melts a metal powder in the collision places. The surfacing is carried out in protected vacuum chambers, which provides an opportunity to work with chemically active metals, sensitive to oxidation, for example, with titanium and its alloys [1].

The technology of layer-by-layer electron beam surfacing in vacuum allows creating dense metal products of a set shape with a high geometric precision [2].

ADDITIVE ELECTRON BEAM EQUIPMENT

Technologies and equipment created by the staff colleagues of PWI, from the very beginning are oriented on the needs of Ukrainian enterprises. For manufacture it is predicted to involve raw materials necessary for the manufacturer. This approach makes it possible to provide a manufacture of parts and assemblies based on the needs of the consumer and in a close contact with him. The developed technologies will allow reducing terms of introduction of new types of products into manufacture, expanding its assortment, and also creating basically new types of products with the properties predicted in advance, the manufacture of which is impossible without application of the methods of 3D printing [1].

In recent years, a noticeable trend is observed in the introduction of additive technologies in the leading domestic companies in the aerospace industry and turbine building: SE EDB “Pivdenne”, JSC “Motor Sich “and SE “Zorya-Mashproekt” Gas Turbine Research and Development Complex [2].

To solve the set problems, investigations were carried out with the use of equipment for 3D printing.

PRINCIPLE OF EQUIPMENT OPERATION

The created equipment operates as a part of the additive electron beam equipment for melting of metal powder materials (Figure 1). The supply and dosing of metal powder takes place directly in the vacuum chamber from the hoppers, from which the metal powder enters the working table under the action of gravity. According to this principle of powder supply, the use of any dosing mechanisms is not provided. After selecting a certain amount, the powder from the hoppers is automatically fed in bulk to maintain a sufficient level on the table.

Metal powder melts under the action of electron beam, which is created by an electron beam gun,

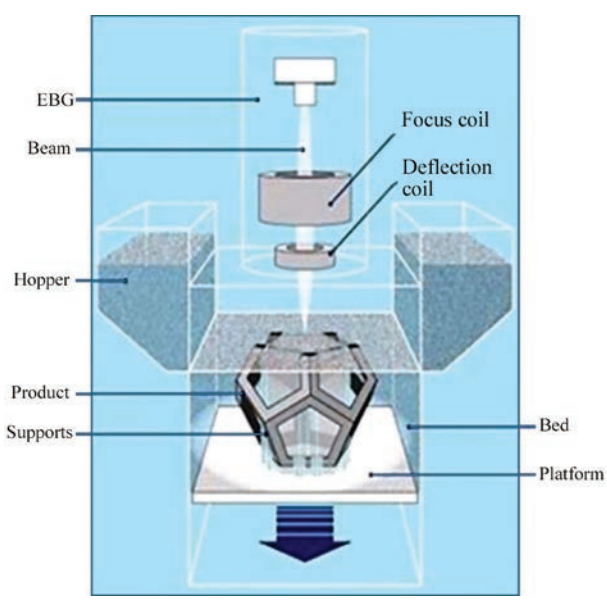

Figure 1. Scheme of additive process

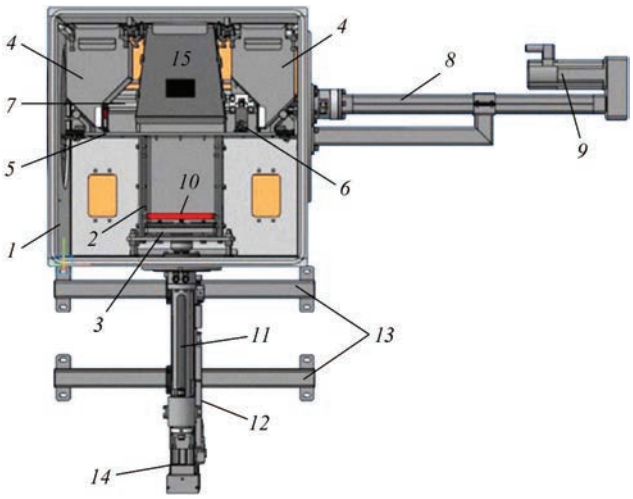

Figure 2. Equipping of vacuum chamber (designations *1–15* see in the text)

where the beam is focused and deflected by appropriate systems.

A product is formed layer-by-layer, while the platform, on which a part is grown, is lowered after the formation of each layer.

TECHNOLOGICAL EQUIPMENT

For investigations, an experimental model of additive equipment based on a small-sized installation of type SV-212M for electron beam welding was designed, manufactured and set up.

The created equipment (Figure 2) consists of vacuum chamber *7*, bed *2*, where platform *3* with pallet *10* is located, on which a product is grown. In the hoppers *4*, a metal powder is located, which is fed in bulk on the table *5*. The rail *6* moves along the table *5* and distributes the metal powder on the surface of the pallet *10*. The rail is fixed on the guides *7*. In a horizontal plane, the rail is moved by the actuator *8* with electric motor *9*.

Platform *3* with pallet *10* are located in the bed *2* and moves along the vertical axis by means of a movable sleeve *11*, which is fixed to the rail *12* mounted on the brackets *13*. The movement is controlled by electric motor *14*.

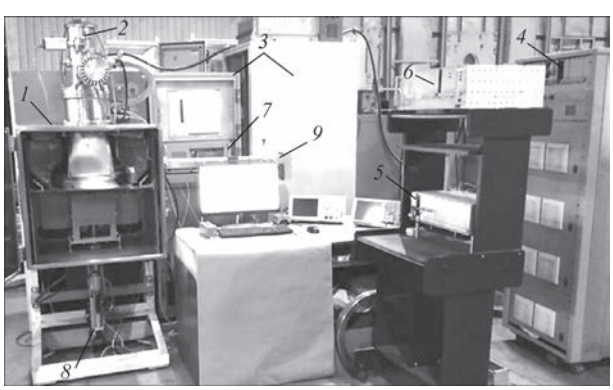

Figure 3. Equipment for electron beam 3D-printing (designation *1–9* see in the text)

Reflector *15* protects the vacuum chamber from the action of a high temperature, that arises on the surface of the layer, where a product is formed.

A photo of the created additive equipment is given in Figure 3.

The equipment (Figure 3) consists of a small-sized vacuum chamber 1 with the mechanisms for moving the platform *8* and the mechanisms for supply and distribution of powder *9*. The power unit includes electron beam gun *2* and high-voltage power source *4*. The electron beam gun *2* is placed on the vacuum chamber. The vacuum system of the equipment provides working pressure in the chamber better than 10^{-4} Torr. The elements of the system for control of the equipment are located in the cabinets *3*, where the units for control of the following units are located: high-voltage source, vacuum system and MCP controller. High-voltage source *4* allows generating a voltage of 60 kV and an electron beam current of up to 100 mA. The amplifiers of scanning waveforms *5* and dynamic focusing *6* form the technological scannings of the electron beam and its focusing. The equipment is controlled by an industrial computer *7*.

ELECTRIC EQUIPMENT

To control the electron beam and technological equipment, the following units were designed, assembled and set up:

- Power unit, consisting of:
  - 60 kV high-voltage source;
  - electron beam gun with a high-voltage cable.
- Scan control system, consisting of:
  - two-channel scanning waveform amplifier;
  - dynamic focusing signal amplifier.
- MCP controller that controls the printing process.
- Electric drive Siemens Sinamics S120 for movement mechanisms with electric motors Siemens Simotics 1FK7.
- Industrial computer with Windows 10 operating system.
- Control cabinet, where switching equipment and MCP controller are located.
- Vacuum system control cabinet.

CONTROL SYSTEM

The system for control of additive equipment (Figure 4) is built on the base of the MCP hardware controller, which controls the current of the electron beam, its scannings, focusing and movement mechanisms. The controller interacts with the industrial PC computer, where models of products are formed and a job-file is created, in which the algorithms of product construction are written. From the computer, a job-file via the Ethernet network goes to the MCP controller, which controls the 3D printer equipment.

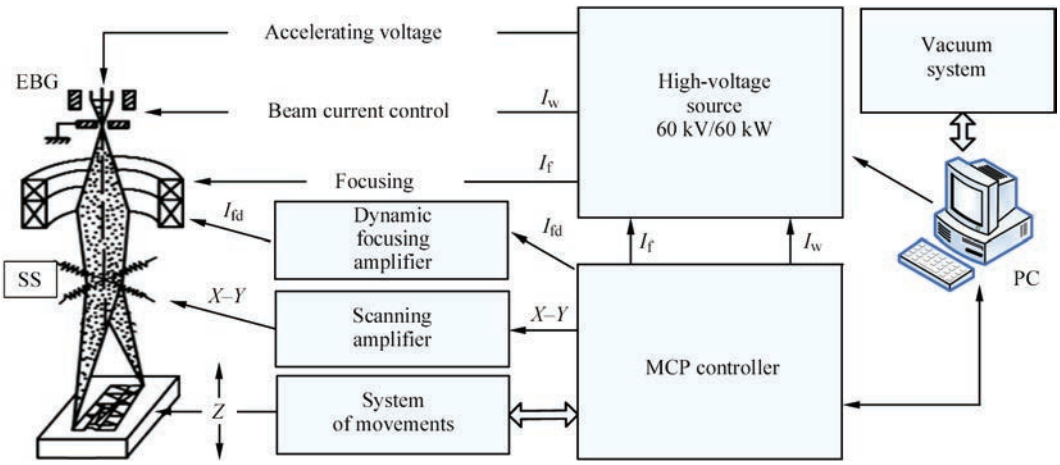

Figure 4. Flow chart of equipment control: EBG — electron beam gun; FC — focus coil; SS — scanning system (other see in the text)

The controller generates analog signals to control the electron beam scannings (Figure 4), coming to the scan amplifiers, to which the deflecting coils of EBG are connected.

The electron beam along the *X* and *Y* axes deflects and creates a surfacing zone of the desired shape. The surfacing process is performed by the program according to the computer model of a product according to preliminary set technological modes.

Electron beam current I_w, currents of static I_f and dynamic I_{fd} focusing are also objects of control.

In addition, the controller controls the system of 3D printer movements, which switches the mechanisms for vertical movement of the platform (*Z* axis) and horizontal distribution of metal powder on the platform.

The industrial computer controls the vacuum system of the equipment and a high-voltage power source.

SOFTWARE AND HARDWARE PLATFORM

To control the additive equipment, in cooperation with Materialise, Belgium, a software and hardware platform was created, which consists of process controller and package of application software for realization of additive manufacturing [2].

The structure of control platform and the state of interactions between its components are given in Figure 5 [2].

SOFTWARE

Creating 3D models of products is possible using any software of CAD type. Analysis and editing of models is performed by the Materialize Magics software.

The ready-to-print computer model of products is further processed by the BuildProcessor software, which allows decomposing models into layers, setting parameters and structure of their formation, specifying power, speed of its movement, focusing and settings of the electron beam for each product. The software also allows choosing the layer thickness, product material and texture variants for filling the layers [2].

BuildProcessor forms a job-file that goes to the MCP controller. Using a job-file, the controller directs the printing process.

For control of the equipment during printing, the MCP Operator interface software is used, where technological parameters of the equipment are set, and also the printing process is controlled and displayed in real time with the possibility of correcting the parameters. The software allows selecting a file of products, determining the start and end time of manufacturing cycle and its stage. The software provides a three-dimensional visualization.

Setting of the MCP controller and calibration of the 3D printer are performed in the Toolbox software (Figure 5).

STAGES OF ADDITIVE MANUFACTURING

The sequence of stages of additive electron beam manufacturing is given in Figure 6 [3].

First, a 3D model of the object is created. This model can be developed using computer-aided design (CAD) systems or reverse engineering methods, such as object laser scanning. The obtained CAD file should be converted into a standard format for addi-

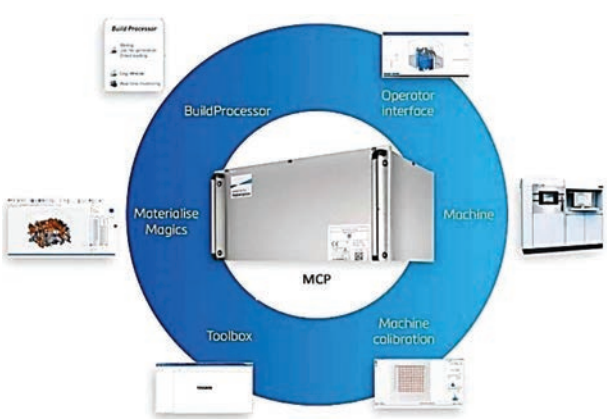

Figure 5. Structure of control platform

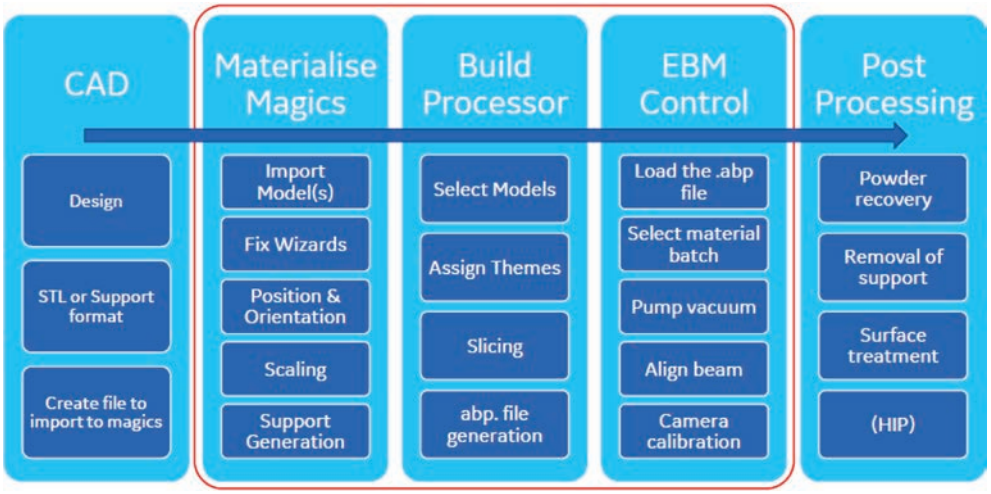

Figure 6. Stages of additive electron beam manufacturing

tive manufacturing, which represents usually a STL file. To maximize cost savings and reduce waste, it is necessary to optimize the location and a number of objects on the assembly platform. Usually, several parts are printed at once. The computer model of assembling products using software is "cut" into layers.

The next stage requires transferring a file to the additive hardware and configure it.

Next, the 3D printer builds products layer-by-layer. The thickness of the layer determines the final quality and depends on the features of printing technology. The size of products depends on the capabilities of the equipment.

After building and cooling, the assembly can be removed from the equipment.

Then, cleaning, polishing and finishing of parts surface is performed. It is also possible to further finish them to the desired standard. This requires using of other machines and tools [4].

SAMPLES OF PRODUCTS AND THEIR INVESTIGATION

On the created experimental model of additive electron beam equipment, experimental products are printed for further testing.

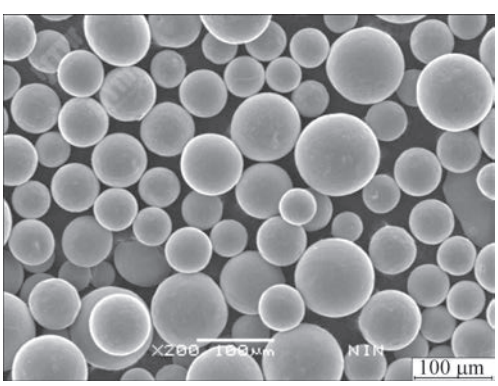

Figure 7. Ti6Al4V ELI powder

The aim of the experiment is to investigate the influence of the basic parameters of the technological process of surfacing on qualitative indices of products [5].

For this purpose, it is expected to print experimental samples and test their properties. It was necessary to investigate: the influence of printing parameters on the formation of surfaces of products; features of the structure of surfaces; chemical composition of samples; based on the results of tests, invent the optimal printing modes.

Ti6Al4V ELI POWDER

To print samples, the powder of the titanium TiAl6Al4V ELI alloy is used, produced by the Chinese company Sino-Euro Materials Technologies of Xi'an Co., Ltd. The powder was produced by the method of plasma melting and centrifugal spraying (PREP technology) [6]. The powder granules have a spherical shape with minimal defects (Figure 7). PREP powder is the best for electron beam additive manufacturing [7].

Technological characteristics and chemical composition of Ti6Al4V ELI powder are provided in Table 1 and Table 2, respectively [8].

Table 1. Technological characteristics of Ti6Al4V ELI powder

Fraction, µm		45–106
Particle-size distribution (PSD), µm	D10	53–58
	D50	85–90
	D90	125–130
Yield, s/50 g		20–25
Density, g/cm^3		2.5–2.7
Oxygen content, ppm		500–1800

Table 2. Chemical composition of Ti6Al4V ELI powder

Composition of alloying elements, wt.% of particles				Composition of impurities, wt.% of particles		
Al	V	Fe	Ti	C	N	H
5.5–6.75	3.5–4.5	≤ 0.3	Base	≤0.08	≤0.05	≤0.015

Table 3. Technological modes of sample surfacing

Number of sample	Beam parameters		Dynamic focusing current, A
	Speed, mm/s	Power, W	
1	780	675	–0.9
2	780	675	–0.61
3	240	270	–0.9
4	540	495	–0.31
5	540	495	–0.61
6	780	675	–1.2
7	540	495	1.27
8	240	270	–0.61
9	780	675	–0.31
10	780	675	0.33
11	540	495	0.96
12	540	495	0.65
13	240	270	–0.31
14	240	270	0.33
15	240	270	0.65
16	780	675	0.65
17	780	675	0
18	240	270	–1.2
19	540	495	–0.9
20	540	495	–1.2
21	780	675	1.27
22	780	675	0.96
23	240	270	0
24	540	495	0
25	540	495	0.33

EXPERIMENTAL SAMPLES

For further tests, from the powder of the titanium Ti6Al4V ELI alloy, experimental samples of products were manufactured (Figure 8).

The produced samples (Figure 9) have a rectangular shape of 24×24 mm and a thickness of 10 mm.

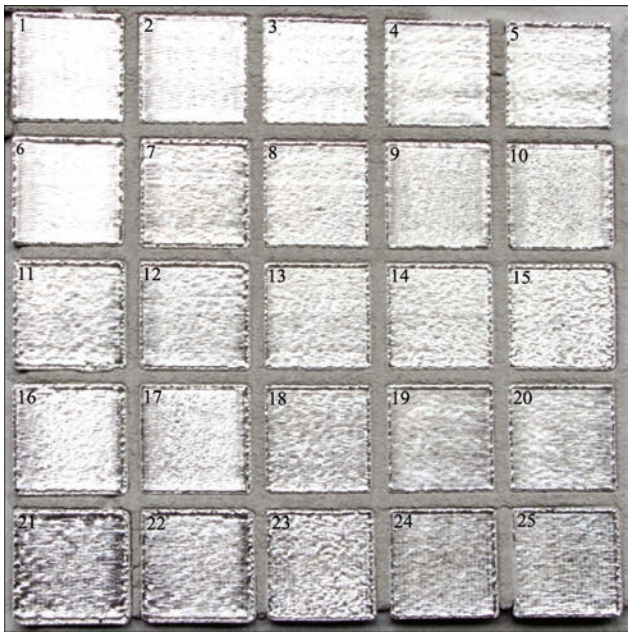

Figure 8. Experimental samples

55 mm from this thickness are technological supports and another 5 mm is the body of a product. A quantity of printed samples is 25 pcs.

For printing samples, the following technological parameters were set:

- beam trajectory shift step is 0.2 mm;
- thickness of the powder layer is 0.1 mm;
- scanning strategy: two-directional with the direction of rotation by 90° for each layer.

For each sample, the speed of movement of the beam and its power and a set dynamic focusing current were determined. The parameters of sample printing are given in Table 3.

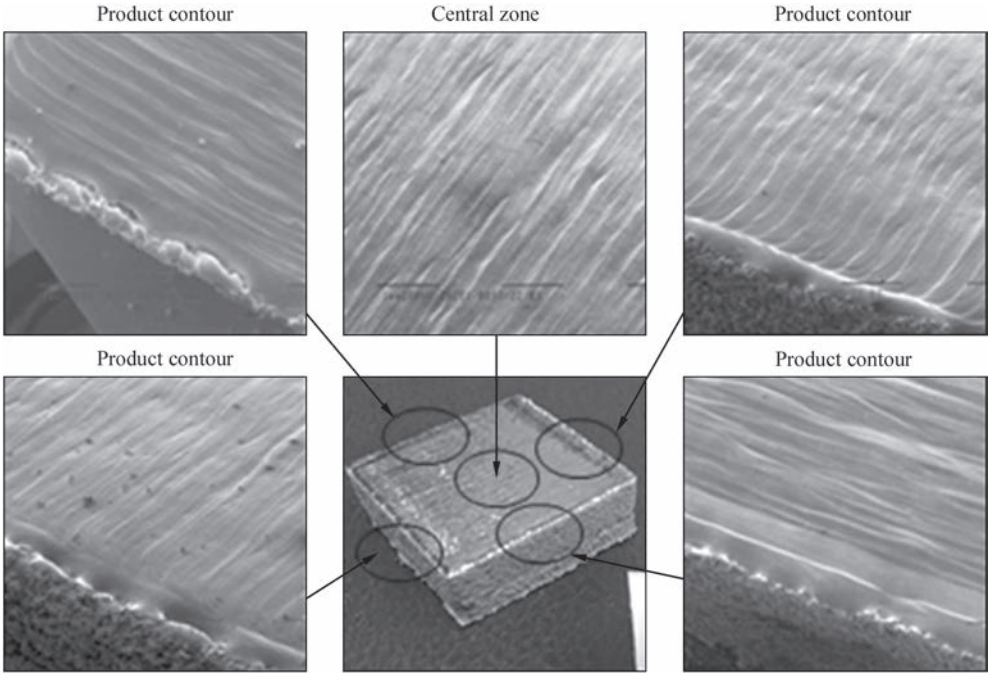

Figure 9. Product sample

Table 4. Chemical composition of samples

Number of measure-ment	Chemical elements, wt.%			
	Al	V	Fe	Ti
Sample No.2				
1	5.04	4.21	0.01	90.75
2	4.85	4.33	0.06	90.76
3	5.09	4.40	0.02	90.48
Sample No.5				
4	4.55	4.32	–	91.13
5	4.32	4.63	–	91.05
6	4.79	4.25	–	90.96
Sample No.8				
7	5.00	4.28	–	90.72
8	5.17	4.04	–	90.79
9	4.90	4.38	–	90.72

INFLUENCE OF TECHNOLOGICAL PARAMETERS ON PRODUCT FORMATION

In order to study the influence of technological parameters on the formation of products of powder of titanium Ti6Al4V ELI alloy, investigations using a method of scanning electron microscopy (SEM, scanning electronic microscope SEM-515 of Philips Company, Netherlands) were conducted. Data on the chemical composition of products were obtained. The samples No.2, No.5 and No.8 were investigated, which were printed on different modes of beam speed and its power: 780 mm/s/675 W (sample No.2); 540 mm/s/495 W (sample No.5); 240 mm/s/270 W (sample No.8), but with the same value of dynamic focusing current I_{df}: –0.61 A. The results of investigations are presented in Table 4.

It was found that the content of aluminium is by 0.6–1.96 % underestimated relative to the chemical composition of powder (see Table 2). The deviation is probable, associated with an increased volatility of aluminium vapour in the conditions of a high vacuum. To eliminate this drawback, it is necessary that in powders of titanium alloys, aluminium content maintained at the highest level. The content of V corresponds to the composition of powder. The peak of Fe in the spectrum (Figure 10) is almost absent (0–0.06 % Fe).

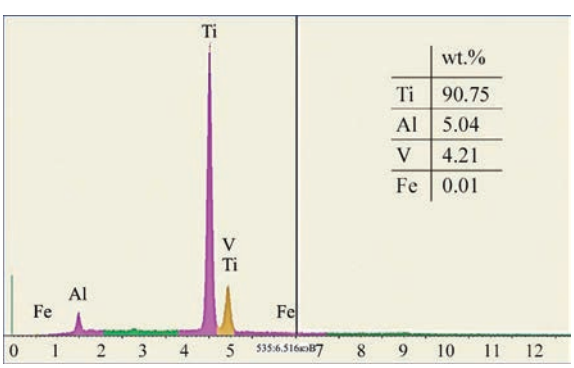

Figure 10. Spectrum of sample No.2

In the course of further studies by SEM method, for each sample, images of surface microrelief were obtained. It was found that products are mostly characterized by a homogeneous profile of microrelief. The structure of the surfaces formed in different zones, differs by its morphology depending on the technological modes.

For example, from Figure 11, it is seen that in the central zone of samples at a beam speed of 780 mm/s and its power of 675 W, depending on the dynamic focusing current (I_{df}), the character of the surface relief and parameters of their roughness are changed.

The surfaces of the produced samples are mostly featured by a banded type in the presence of a clear direction (Figure 11). On some surfaces, the areas with local microroughnesses are observed (Figure 11, *e–g*). Also, changes in the roughness parameters of surface microrelief are observed, namely distances (or step) between roughnesses of the surface profile behind the apexes and the height of the relief (Figure 11, *g–i*).

In addition to the abovementioned structural characteristics of surfaces, depending on the speed of the beam and its power, the general appearance of surface relief also changes. Thus, while reducing the speed of the beam to 240 mm/s and power to 270 W, surfaces are formed with another relief in the absence of a clearly defined banded structure at some coarsening of the step of the roughnesses of the surfaces behind the apexes (Figure 12). Such structural changes can be reduced to the temperature conditions of heating and cooling while producing samples.

Taking into account the abovementioned, it becomes necessary to conduct more detailed studies of the parameters of surface microrelief in the samples produced on different technological modes and compare these structural characteristics, depending on speeds of the beam and power, as well as the dynamic focusing current.

Therefore, the next investigations will be devoted to the study of the structure of surfaces of samples in several zones (central zone and contour of the sample) at different magnifications, including a top view of surfaces and at inclined position of samples; flaws detection (pores, lacks of fusion, microroughnesses, inclusions); measurement of microrelief roughness parameters in the examined areas, namely the distances between the roughnesses of the surface profile behind the apexes and the height of the relief.

EXPERIMENTAL SAMPLES OF PRODUCTS

In the created additive electron beam equipment according to computer models, industrial and medical products were printed, the modes of whose printing were optimized based on the results of previous studies.

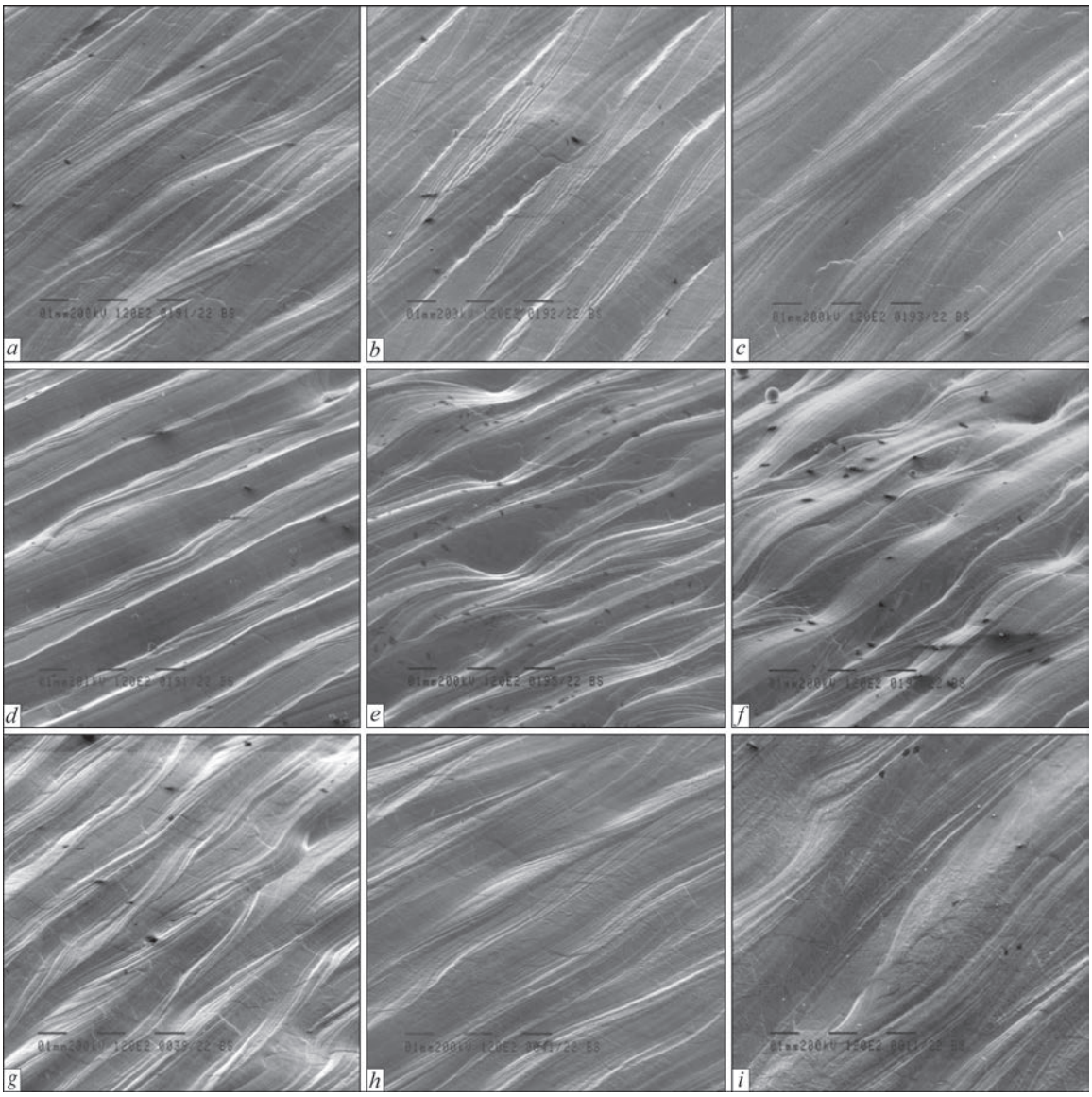

Figure 11. Surface relief (×120) in the central zone of samples at a beam speed being 780 mm/s and power of 675 W, depending on the dynamic focusing current (I_{df}): *a* — I_{df} = –1.2 A (sample No.6); *b* — I_{df} = –0.9 A (sample No.1); *c* — I_{df} = –0.61 A (sample No.2); *d* — I_{df} = –0.31 A (sample No.9); *e* — I_{df} = 0 A (sample No.17); *f* — I_{df} = 0.33 A (sample No.10); *g* — I_{df} = 0.65 A (sample No.16); *h* — I_{df} = = 0.96 A (sample No.22); *i* — I_{df} = 1.27 A (sample No.21)

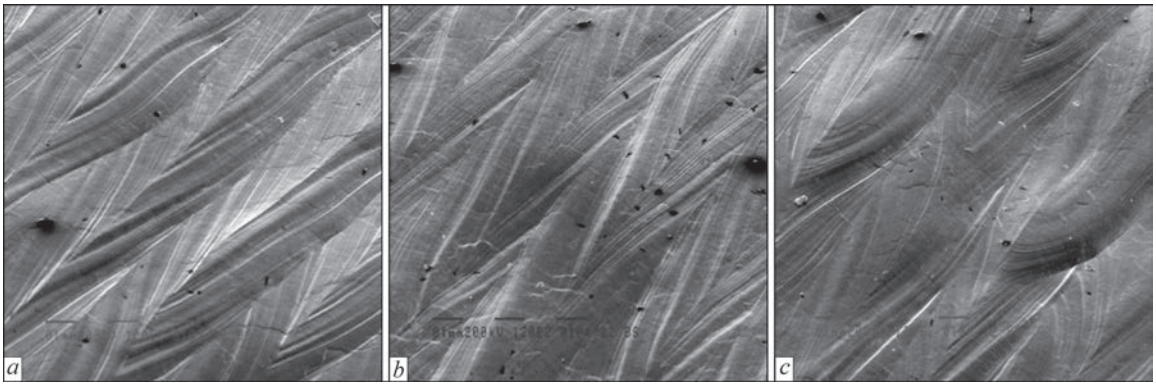

Figure 12. Surface relief (×120) in the central zone of samples at a beam speed of 240 mm/s and the power 270 W depending on dynamic focusing current (I_{df}): *a* — I_{df} = –1.2 A (sample No.18); *b* — I_{df} = –0.31 A (sample No.13); *c* — I_{df} = 0.65 A (sample No.15)

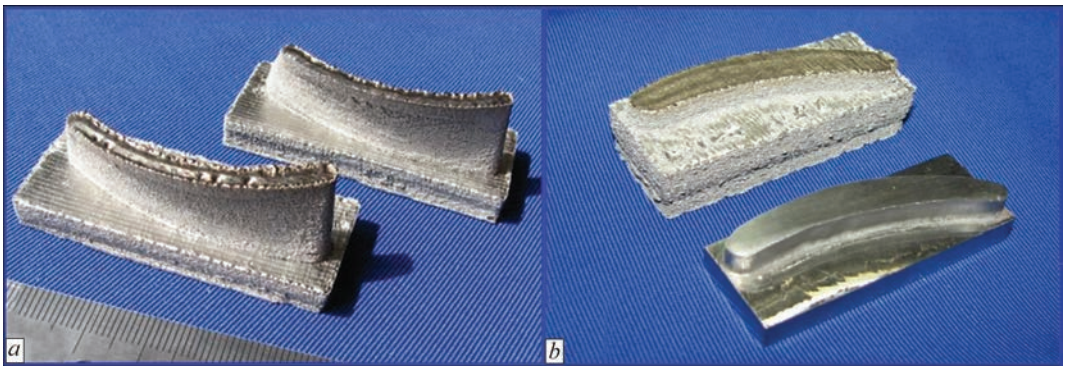

Figure 13. Experimental models of stator blades of gas turbine aircraft engine (description *a*, *b* — see in the text)

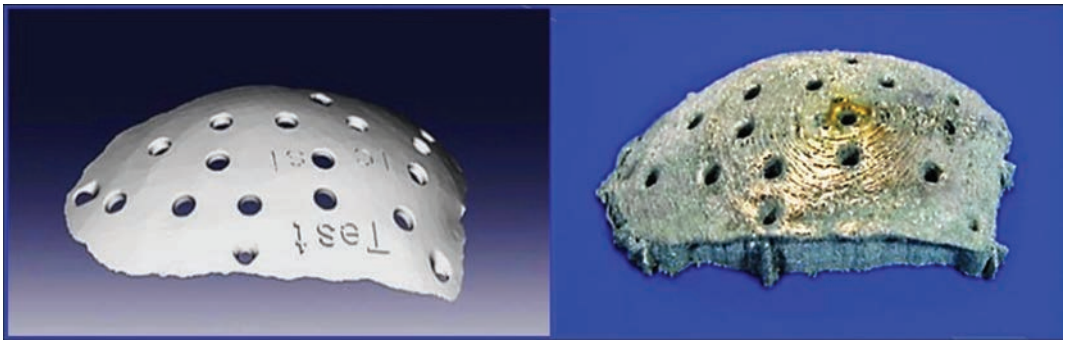

Figure 14. Implant of braincase. Model and printed product

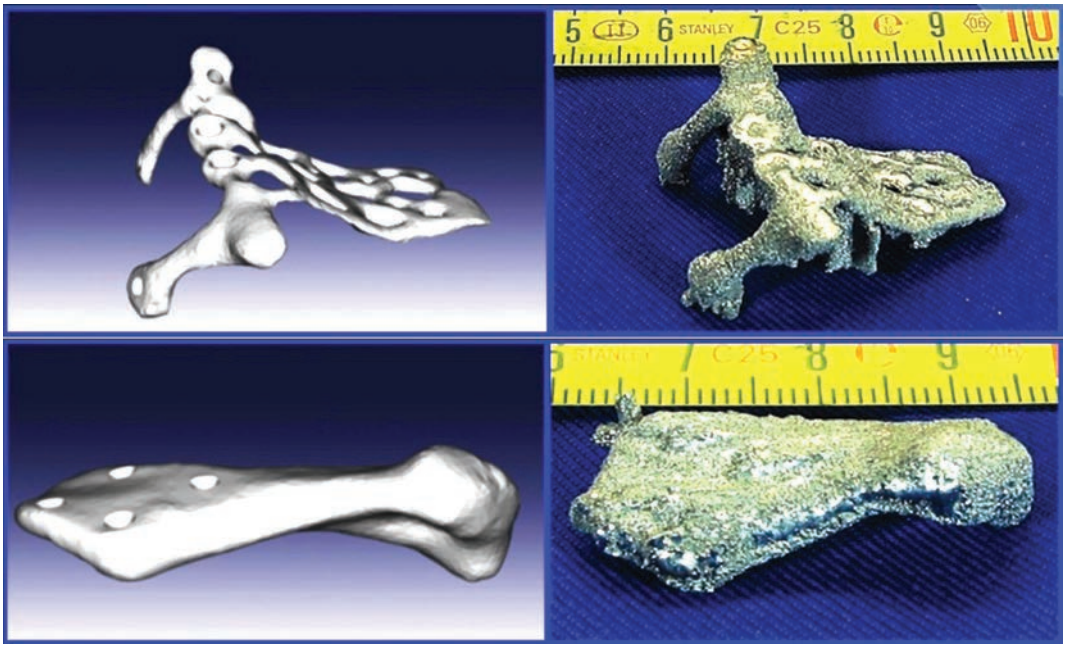

Figure 15. Biopros*thesis. Models and printed products

Figure 13 shows experimental models of stator blades of gas turbine aircraft engine, printed from metal powders of the following titanium alloys:

a) Ti6Al4V ELI, fraction of 45–106 μm, granules of a spherical shape, produced by PREP technology, manufacturer is Sino-Euro Materials Technologies of Xi'an Co., China;

b) VT-20, fraction of 63–160 μm, granules of an arbitrary shape, produced by HDH technology, manufacturer is LLC "Ti Technology", Ukraine.

Figure 14 shows a computer model and a printed implant of a humane braincase, Figure 15 shows bioprosthesis and their models. Products made of powder of titanium Ti6Al4V ELI alloy.

CONCLUSIONS

Based on the results of research works, an experimental model of additive equipment was designed and manufactured, electron beam technology of layer-by-layer surfacing of metal products of powder materials was created, experimental samples of products were printed; laboratory examinations of samples were carried out, industrial and medical products were manufactured.

REFERENCES

1. Nesterenkov, V.M., Matvejchuk, V.A., Rusynik, M.O. et al. (2017) Application of additive electron beam technologies for manufacture of parts of VT1-0 titanium alloy powders. *The Paton Welding J.*, **3**, 2–6. DOI: https://doi.org/10.15407/tpwj2017.03.01
2. Matviichuk, V.A., Nesterenkov, V.M. (2020) Additive electron beam equipment for layer-by-layer manufacture of metal products from powder materials. *The Paton Welding J.*, **2**, 41–46. DOI: https://doi.org/10.37434/tpwj2020.02.08
3. Stolt, R., Heikkinen, T., Elgh, F. (2018) Integrating additive manufacturing in the design of aerospace components. In: *Proc. of 25th Int. Conf. on Transdisciplinary Engineering (TE2018) (Modena, Italy, July 2018)*. DOI: https://doi.org/10.3233/978-1-61499-898-3-145
4. Paria, Karimi (2018) Electron beam melting of alloy 718: Influence of process parameters on the microstructure. *University West, Dept. of Engineering Sci. Division of Subtractive and Additive Manufacturing. Licentiate Thesis*.
5. Günther, J., Brenne, F., Droste, M. et al. (2018) Design of novel materials for additive manufacturing: Isotropic microstructure and high defect tolerance. *Sci. Rep.*, 8(**1**), 1298.
6. Vostrikov, A.V., Sukhov, D.I. (2016) Manufacture of granules by PREP method for additive technologies: Current status and prospects of development. *Trudy VIAM*, 44(**8**), 17–23 [in Russian].
7. Iliyushchenko, A.F. (2019) *Additive technologies and powder metallurgy*. Minsk, Medison [in Russian].
8. Powder Ti6Al4V ELI. *Site: Sino-Euro Materials Technologies*. https://en.c-semt.com/ti/

ORCID

V.A. Matviichuk: 0000-0002-9304-6862,
V.M. Nesterenkov: 0000-0002-7973-1986,
O.M. Berdnikova: 0000-0001-9754-9478

CONFLICT OF INTEREST

The Authors declare no conflict of interest

CORRESPONDING AUTHOR

V.M. Nesterenkov
E.O. Paton Electric Welding Institute of the NASU
11 Kazymyr Malevych Str., 03150, Kyiv, Ukraine
E-mail: nesterenkov@technobeam.com.ua

SUGGESTED CITATION

V.A. Matviichuk, V.M. Nesterenkov, O.M. Berdnikova (2022) Additive electron beam technology for manufacture of metal products from powder materials. *The Paton Welding J.*, **2**, 16–25.

JOURNAL HOME PAGE

https://pwj.com.ua/en

Received: 13.12.2021
Accepted: 31.03.2022

https://doi.org/10.37434/tpwj2022.02.04

DESTRUCTION OF WELDED JOINTS OF SINGLE-CRYSTAL HIGH-TEMPERATURE NICKEL ALLOYS AT TENSILE TESTING

K.A. Yushchenko, B.O. Zaderii, I.S. Gakh, G.V. Zviagintseva, T.O. Aleksiienko

E.O. Paton Electric Welding Institute of the NASU
11 Kazymyr Malevych Str., 03150, Kyiv, Ukraine

ABSTRACT

Mechanical properties were determined and features of destruction of welded joints on single-crystals of high-temperature nickel alloys at tensile testing in the range of temperatures close to working temperatures were studied. Two characteristic temperature ranges of destruction were found: 500–800, 800–1200 °C. In the first temperature range welded sample destruction occurs in the base metal at mixed fracture mode: brittle, quasibrittle and ductile. In the second range destruction takes place in the weld metal, fracture is multicenter, predominantly brittle with presence of secondary cracks. The considered features are related, mainly, to changes of the initial structure of the single-crystal, as a result of solidification and at cooling of the weld metal. These mainly are formation of a multilevel substructure, refinement of dendrites, γ- and γ′-phases, eutectic formations and carbides at reduction of dendrite liquation of the weld metal.

KEY WORDS: single-crystal, high-temperature nickel alloys, welded joint, weld, tensile testing, temperature ranges of destruction, destruction features, microstructure

INTRODUCTION

Improvement of the effectiveness of modern gas turbine engines (GTE) is achieved due to increase of gas temperature at the turbine inlet, which, in its turn, makes certain requirements on the high-temperature strength of materials used to manufacture the components and parts of the hot path [1–3]. Satisfying these requirements through application of high-temperature nickel alloys (HTNA) and multicomponent alloying, optimization of the structure, in particular, single-crystal one, has practically exhausted its potential. Solving this problem due to a change and optimization of the geometry of individual parts often becomes a complex technology and cost problem. This is particularly evident, when growing one of the critical and complex-loaded GTE parts — a single-crystal blade with transpiration and other cooling methods. Here, alongside producing a perfect single-crystal structure of a certain crystallographic orientation, it is necessary to ensure a complex geometry of both the blade outer surface, and inner cooling channels of a certain cross-section and surface finish [3, 4].

Despite the advances of the technology of growing single-crystals by directional solidification method, manufacturing welded parts, made up of individual, more readily adaptable-to-fabrication structural elements, is ever wider used [5–10].

A sufficiently large number of publications are devoted to the subject of both welding and growing HTNA single-crystals. However, there is practically no information about the mechanical properties and destruction features of either welded joints as a whole, or of the welds taken separately.

The objective of this work was studying the properties and destruction features of welded joints of HTNA single-crystals at elevated temperatures, taking into account the need to develop a technology for structure welding.

INVESTIGATION PROCEDURES

HTNA widely applied in industry — ZhS26 was selected as the initial material for work performance. The alloy chemical composition is as follows, wt.%: 4.3–5.6 Cr, 4.5–8.0 Al, 0.8–1.2 Ti, 0.8–1.4 Mo; 10.9–12.5 W, 8.0–10.0 Co, 1.4–1.8 Nb, 0.22–0.27 Mn, 0.9–1.1 Fe, 0.8–1.2 V, 0.13–0.18 C. Welding of 1.5–2.5 mm samples, cut out of blanks, produced by the method of directional high-gradient solidification, was performed by the electron beam, as the most precise and widely accepted method in aircraft construction. The modes and crystallographic orientation of the samples were selected proceeding from the condition of sound formation of the welds, preservation of the initial crystallographic orientation (not more that 10° deviation was allowed), ensuring perfection of the single-crystal structure (absence of high-angle grain boundaries) of the weld metal [7, 11–13]. Samples for welding, testing and investigations were cut out by spark method with subsequent grinding. The cross-section and length of the working part of tensile samples were equal to ~4 mm^2 and 18 mm, respectively.

Mechanical testing was conducted in ALLO-TOO unit of Gleeble type in a chamber with residual pressure of <10^{-2} Pa at load rate of $1.84\cdot10^{-3}$ s^{-1}. The range of testing temperatures was equal to 500–1200 °C,

Copyright © The Author(s)

which corresponded to average operating parameters of GTE blades from ZhS26 alloy. Temperature monitoring, load recording and graphic presentation of the "load-displacement" dependencies were performed using software [14].

Tested were samples of two types: with longitudinal and transverse location of the weld relative to the load direction (Figure 1). As the cross-section of the weld and that of the sample with its longitudinal location (Figure 1, *b*) coincide, their testing allows evaluation of the influence of structural changes resulting from electron beam remelting and solidification at single-crystal welding. Testing samples with a transverse weld location gives an idea about the behaviour of the welded joint as a whole during testing, which consists of a combination of different structural regions: base metal, HAZ, and weld metal.

Crystallographic orientation of the initial samples, welded joints and structural elements was assessed involving the procedure of X-ray diffractometry by analysis of the distribution of intensity of reflections on the pole figures, θ–2θ X-ray patterns ($Iq_{\parallel}$) and in the plane, normal to the diffraction vector q–$Iq_{\perp}$ [15–17]. Structural state of welded joints and fracture pattern were studied by the methods of optical microscopy ("MIM-7", "Neophot-32"), electron scanning microscopy (Camscan-4, SEM-515 PHILIPS), distribution of chemical elements in individual components of the fracture and structure was investigated by EDX analysis in JEOL microscope with JNCO attachment.

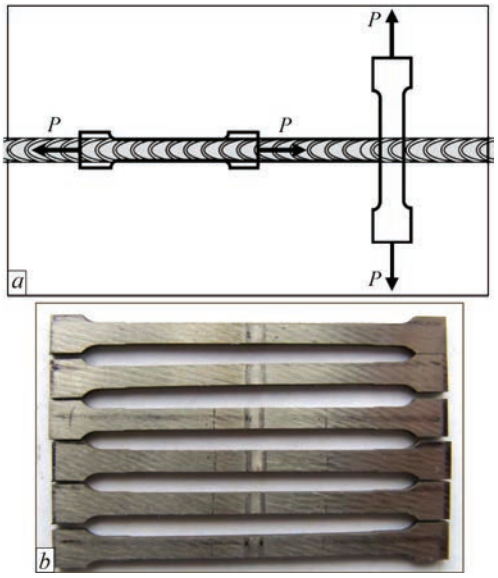

Figure 1. Scheme of cutting out tensile samples from welded joints of HTNA single-crystals and orientation of load *P* at testing (*a*) and general view of tensile samples (*b*)

RESULTS AND DISCUSSION

WELDED JOINT STRUCTURE

The welded alloy (base metal) in the initial condition is characterized by a developed cell-dendrite structure, which includes a finely-dispersed strengthening γ′-phase (Ni_3Al), uniformly distributed in γ-solid solution of the nickel matrix (Figure 2, *a*) with individual inclusions of γ–γ′ eutectic formations and carbide precipitates of a complex composition and topography. Eutectic formations and carbides are predominantly

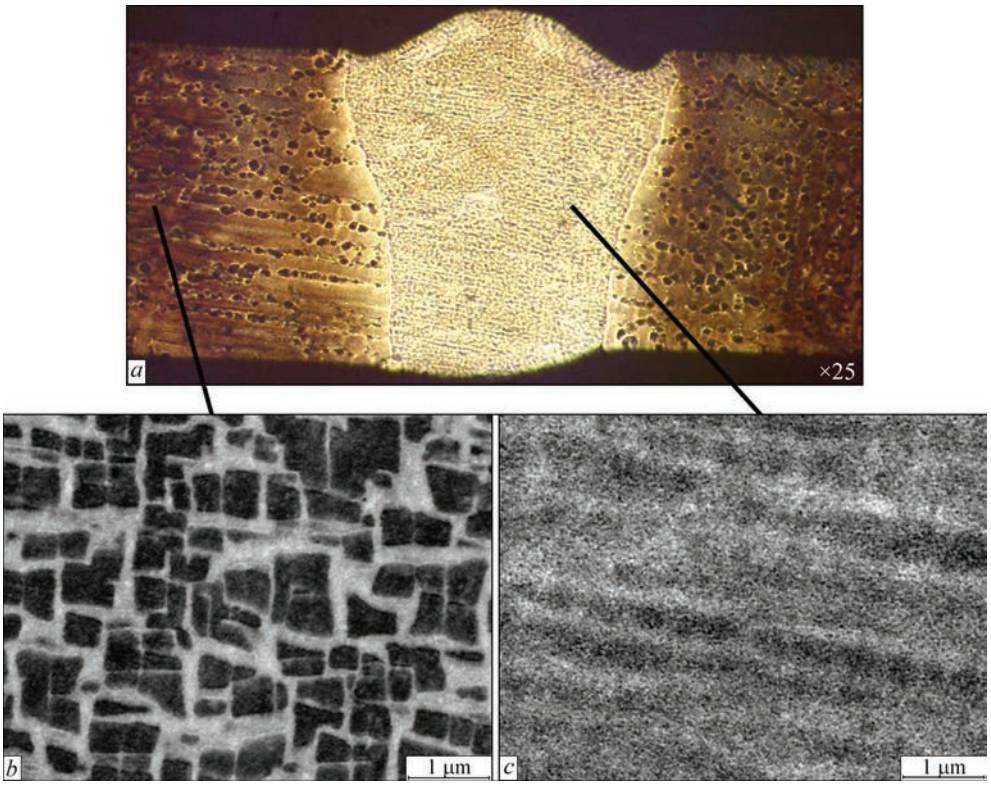

Figure 2. Macrostructure of welded joint (*a*), microstructure (γ/γ′) of initial metal (*b*) and weld (*c*) of HTNA single-crystal

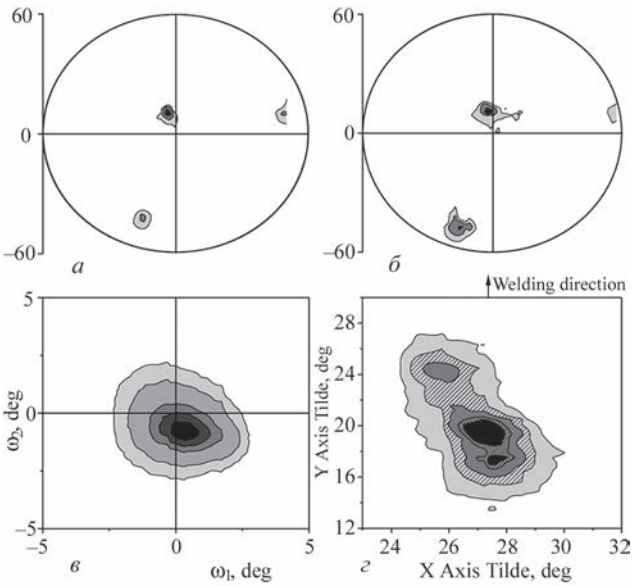

Figure 3. Pole figures {220} (*a*, *b*) and typical 2D distribution of $Iq_{\perp}$ of {220} reflections (*c*, *d*) in the initial growth HTNA single-crystal (*a*, *c*) and in the weld (*b*, *d*), *x*, *y* — angular instrumental coordinates; ω_1 and ω_2 — angular coordinate of reciprocal space

located in the interdendritic, interphase gaps. γ′-phase content in the alloy is equal to ~61 %.

Welded joint structure differs from that of the base metal by noticeably smaller dimensions of the structural components. Thus, if the interdendritic spacing (λ) of the base metal is equal to 200–300 μm, in the weld it decreases to 30–50 μm on the weld axis and to 3–12 μm near the fusion line (Figure 2, *b*). The size of γ′-phase particles ($d\gamma_1$) in the initial metal is 0.3–0.6 μm, in the weld it is by an order of magnitude smaller — 0.04–0.08 μm, and in the HAZ it is 0.3–0.02 μm. In connection with reduction of the dimensions of the structural components the chemical heterogeneity of the weld metal markedly decreases (Table 1).

The selected modes and welding scheme allowed limiting the deviation of crystallographic orientation of the welded joint from the initial value by not more than 7° (Figure 3). The disorientation of the weld metal structure as a result of the influence of the thermodeformational cycle of welding can be more clearly assessed by $Iq_{\perp}$ distribution (Figure 3). Distribution of $Iq_{\perp}$ and its fragmentation according to [15–19] corresponds to formation of a substructure with a multilevel directional disorientation of the metal by the dislocation boundaries that does not exceed 2°. Formation of a multilevel structure leads to the conclusion about the existence of residual stresses in the weld. The found shifting of the peak of $Iq_{\parallel}$ distribution in "θ–2θ" X-ray patterns (Figure 4)* towards the smaller angle of 2θ reflection points to the presence of tensile stresses in the direction along the weld [15–17]. Calculation, made using the Hooke's law and allowing for shifting of $Iq_{\parallel}$ peak showed that for welds of (110) orientation can reach 397 MPa, and for (111) it is 520 MPa.

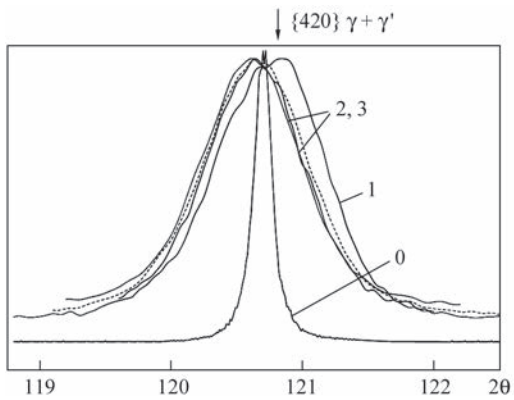

Figure 4. "θ–2θ" distribution of $Iq_{\parallel}$ of {420} reflections in the standard (0), in the initial metal (*1*) and along the axis of weld metal (*2, 3*) of single-crystal ZhS26

DESTRUCTION FEATURES OF SAMPLES WITH TRANSVERSE LOCATION OF WELDS (WELDED JOINTS)

In the generalized form, the results of rupture testing of the welded samples are given in Figure 5 as σ_t and $\sigma_{0.2}$ dependencies on temperature. They can be conditionally subdivided into two regions. The first region (testing temperature $T_{test} \leq 800$ °C) is characterized by a smaller dependence of σ_t and $\sigma_{0.2}$ on temperature, more noticeable influence of the crystallographic orientation and sample fracture in the base metal. In the second region ($T_{test} > 800$ °C) an intensive lowering of σ_t and $\sigma_{0.2}$ values, leveling of the influence of the initial crystallographic orientation are observed, and sample fails through the weld.

The above-mentioned fracture features of the welded joints can be explained as follows. Welded joints are a composite material, which consists of regions of different structure: base metal, HAZ and weld. Owing to more than an order higher dispersity of the structural components, according to Hall–Patch

Table 1. Dendritic liquation $k_l = C_d/C_{int.sp}$ of the main chemical components of initial ZhS26 alloy and weld metal (k_l — liquation coefficient, C_d — concentration on dendrite axis, $C_{int.sp}$ — concentration in interdendritic space)

Region	Al	Ti	V	Cr	Co	Nb	Mo	W
Initial metal	0.7	0.55	1.28	1.98	1.2	0.6	1.6	1.89
Weld metal	0.94	0.7	1.2	1.04	1.02	0.9	1.08	1.24

*O.P. Karasevska took part in word performance.

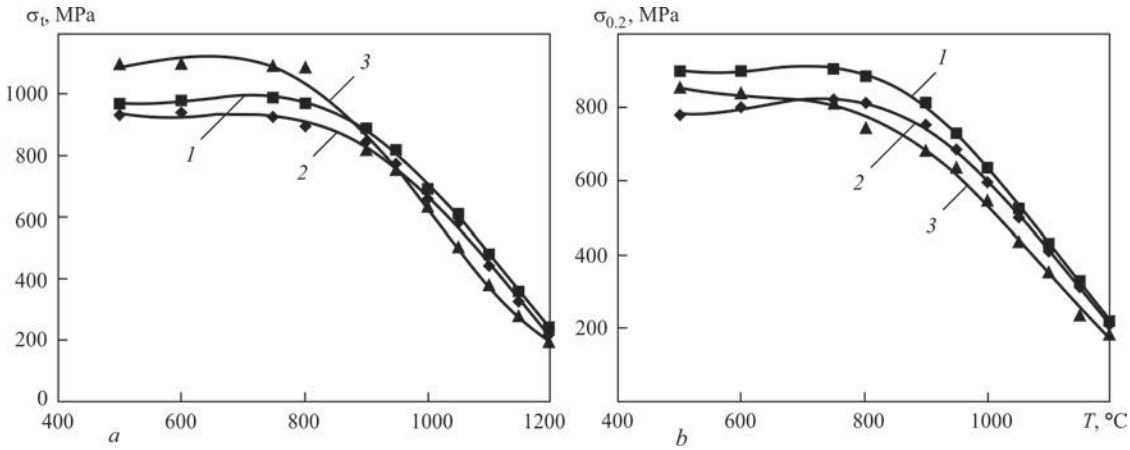

Figure 5. Dependence of ultimate strength σ_t (*a*) and yield limit $\sigma_{0.2}$ (*b*) on testing temperature of welded samples of ZhS26 alloy single-crystals in the transverse (*1*, *2*) and longitudinal (*3*) position of the welds. Load orientation: ~<100> (*1*, *3*) and ~<110> (*2*)

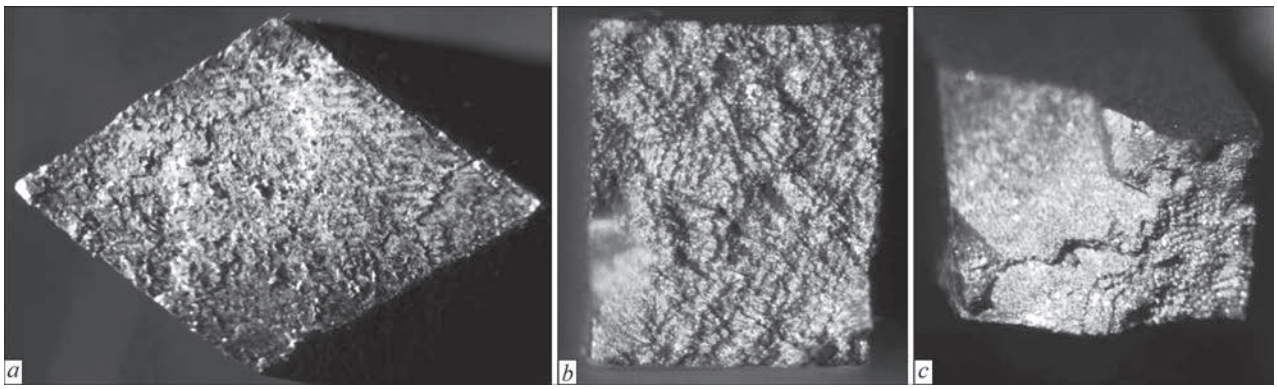

Figure 6. Appearance of fractures in welded joint of ZhS26 alloy single-crystal of orientation close to [011], after testing for uniaxial tension at the temperature of: *a* — 600 °C; *b* — 1050; *c* — 900

law [19–21], the weld metal is in a more strengthened state. Strengthening is also related to the observed increase of the density of unpinned chaotic dislocations in the weld metal (see Figure 4).

At increase of testing temperature to 800 °C and higher, fracture shifts into the HAZ and the weld, as a result of weakening of the strengthening effect of the finely-dispersed structure, as well as a result of increase of defect mobility [21, 22] on the low-angle boundaries of the weld metal.

Fractures of samples tested at moderate (≤600 °C) temperatures, are characterized by quasicleavage topography, combined with presence of regions of fine-cellular tear with weakly manifested elongation (Figures 6, 7). At increase of test temperature to 800 °C, the fractures develop a mixed fracture mode — a combination of brittle (30–35 %), quasibrittle (20–25 %) and ductile variants (45–50 %). Accordingly, the fracture surface microrelief is represented by sites of low-ductility shear in metal and quasicleavage facets of 50–60 μm size, steps of 1–20×20–100 μm of brittle banded appearance, and shallow dispersed pits (0.5–1.5 μm) of ductile fracture (Figure 7). As the temperature approaches 800 °C, the ductile fracture fraction rises up to 50–60 %, fracture takes the pit-ductile form, and brittle fracture elements are gradually replaced by relief pits, fringed by tear ridges. Investigations of the side surfaces of

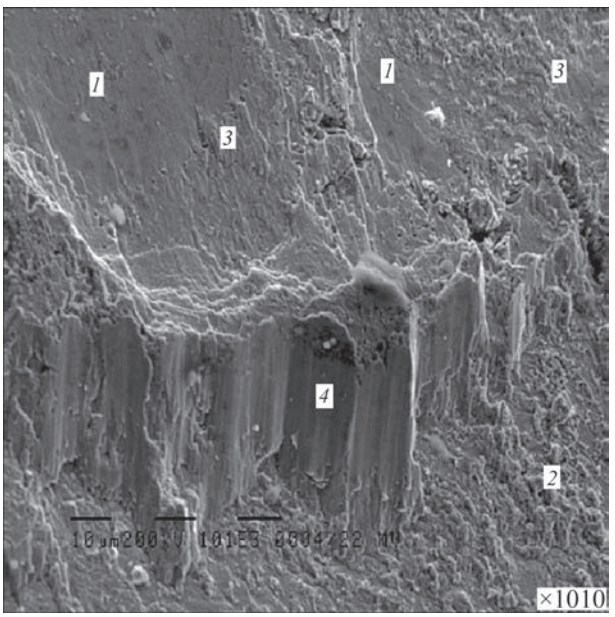

Figure 7. Fragment of fracture surface of the welded joint. Testing temperature of 600 °C (*1* — steps with brittle banded relief; *2* — dispersed pits of ductile fracture; *3* — shear facets, quasibrittle failure areas; *4* — banded relief, brittle fracture mode, band width Δ_b = 10 – 20 μm)

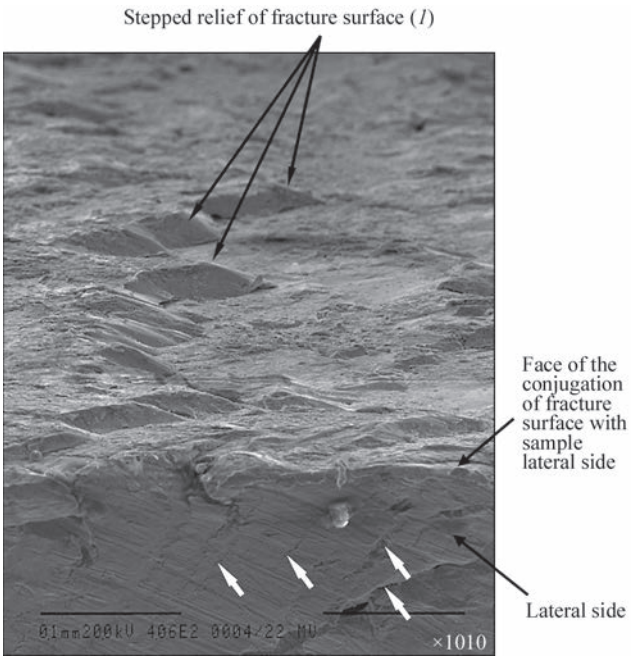

Figure 8. Conjugation of the sample lateral side and fracture surface. Light arrows mark the microcracks on the sample side surface, formed by plastic shear mechanism along the easy slip planes {111} <110>. Test temperature of 600 °C (*1* — steps with brittle banded relief)

samples, broken in this temperature range (Figure 8), revealed the presence of slip bands, relief shear areas and microcracks which pass at a small angle to fracture plane, which illustrates the shear mode of fracture along the most loaded slip systems [18, 19, 23].

Welded joint fracture in the temperature range of 900–1200 °C runs in the weld, and is characterized by multicellularity (Figure 9). The fractures are represented by such elements as: cleavage facets — of ~10–20 μm size and quasicleavage facets of ~8–15 μm, carbide type phase precipitates (0.3–0.4×3.0–7.0 μm) on cleavage facets, secondary microcracks (20–100 μm) and coarse delaminations (100–350 μm). Individual local areas of the ductile component (5–7 %) allow us assuming that fracture runs with a certain fraction of plastic deformation. The general fracture mode is brittle (~90–93 %).

DESTRUCTION FEATURES OF SAMPLES WITH A LONGITUDINAL LOCATION OF WELDS

At testing with longitudinal loading in the temperature range of 500–600 °C, the destruction of the welds occurs in the ductile mode with pit size of ~2–9 μm in the fracture (Figure 10). At increase of testing temperature up to 800 °C the failure mode changes to a mixed one, areas of quasibrittle failure of ~3.0–9.5 μm are observed in the fracture near the pits. At further increase of temperature up to 1200 °C, the mixed failure is characterized by increase of the fraction of quasibrittle component, secondary cracks

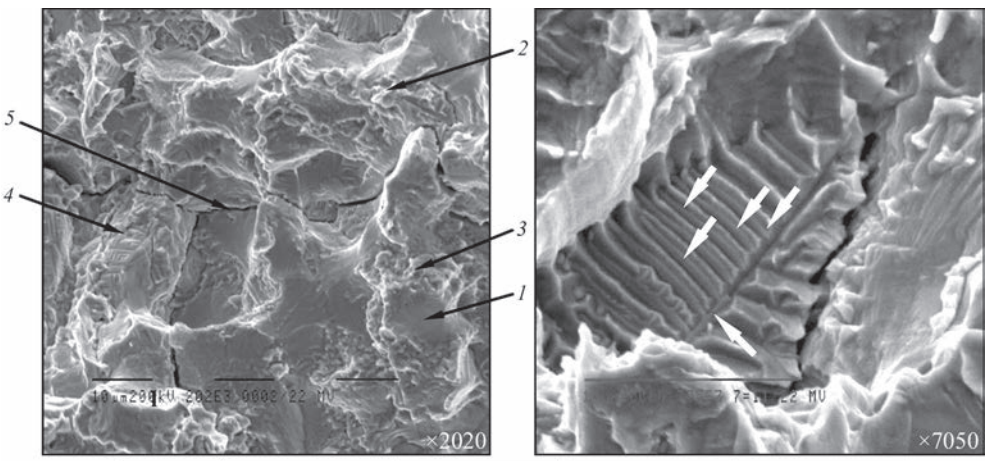

Elements	1 Brittle	2 Quasibrittle	3 Ductile	4 PP
Al	2.64	2.86	1.92	3.01
Ti	1.66	1.22	1.58	3.77
V	0.35	0.34	0.41	0.45
Cr	4.45	5.63	5.75	4.7
Co	9.31	9.47	9.61	6.92
Ni	69.86	62.72	68.58	50.75
Nb	1.47	1.78	1.75	12.05
Mo	1.67	2.66	2.06	5.3
W	8.6	13.32	8.35	13.05

Figure 9. Fragments of fracture surface in different regions of weld metal at welded joint testing for uniaxial tension and chemical element content in the fracture (wt.%). Testing temperature was 1050 °C. Welded joint orientation was [100]. *1* — brittle fracture: size of cleavage facets d_f = 10–20 μm; *2* — quasibrittle fracture; *3* — local regions of ductile fracture: dispersed pits of size d_p = 1–2 μm; *4* — phase precipitates (PP); *5* — secondary cracks l_{cr} ~ 20–100 μm (light arrows — PP)

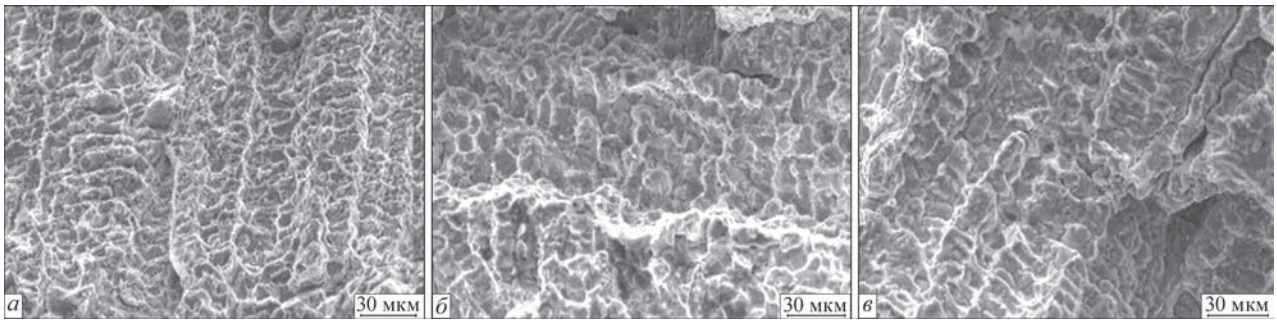

Figure 10. Fragments of fracture surface of a weld of ZhS26 alloy single-crystal. Testing for uniaxial tension in the longitudinal direction at temperatures of: 600 °C (*a*), 1050 (*b*), 1200 (*c*)

are observed (Figure 10), and the size of failure elements on the fracture surface is equal to 3.5–10.0 μm (1050 °C) and 4.5–10.5 μm (1200 °C). The fractures inherit the dendrite morphology of the microstructure of the weld, and of structural formation defects, developing during solidification.

A certain difference in fracture morphology, as in the properties of welds, tested in the longitudinal and transverse directions, is most probably, associated with different orientation of the weld metal dendritic structure relative to the direction of the applied load.

Note the complexity and multifaceted nature of the fractures, nonuniformity of the relief that reflects the heterogeneity of the structure and crystallographic orientation of individual regions of the welded joints.

Proceeding from analysis of the results of the above studies, features of destruction, mechanical properties and structure, we can conclude that the established difference in the properties and characteristic deformations and failure of welded joints of ZhS26 single-crystals in the high- and low-temperature range is largely determined by the nature of structural changes, occurring as a result of welding.

CONCLUSIONS

1. When assessing the destruction features and properties of nickel alloy welded joints, they should be regarded as a composite material, consisting of areas of different structure.

2. As a result of welded joint testing for uniaxial tension in the temperature range of 500–1200 °C, two destruction regions were determined: 500–800 °C in the base metal and 800–1200 °C — in the weld metal.

3. The destruction nature and type, properties of welded joints of HTNA single-crystals, which are a composition of structural regions, are determined by the structural features of these regions, alongside the initial crystallographic orientation.

4. Failure of welded joints in 500–800 °C temperature range, considering the higher strength of the welds, which differ by a higher dispersity of the structure, takes place in the base metal. The fracture is mixed — brittle, quasibrittle, and ductile. At increase of testing temperature, the fraction of elements of brittle fracture (in the base metal) decreases with increase of the number of ductile fracture pits.

5. Failure of welded joints in the temperature range of 800–1200 °C, occurs in the weld, in connection with reduction of the strengthening effect of the finely-dispersed structure, dissolution of γ′-phase, activation of the diffusion processes and unblocking of dislocations. The fractures differ by multicellularity and are predominantly of a brittle nature with presence of local secondary microcracks and delaminations.

6. The type of fracture of welds, tested in the longitudinal direction in the temperature range of 500–800 °C, is characterized by prevalence of the ductile component with local areas of quasibrittle failure, at 800–1200 °C — the failure is mixed, with increase of volume fraction of the quasibrittle component with temperature rise, and presence of secondary cracks on the fracture surface. Unlike the welded joints in the transverse direction, the welds are characterized by a more homogeneous structure along their length.

7. Analysis of the properties and destruction features of welded joints, leads to the conclusion that development of the technology of fabrication of welded structures from single-crystal HTNA should be based on the need to preserve a homogeneous structure and properties of individual areas of the joint, along with taking into account the physical and technological conditions of preservation of the single-crystal structure.

REFERENCES

1. Hurada, H. (2003) High temperature materials for gas turbines. The present and future. In: *Proc. of Int. Gas Turbine Congress-2003 (Tokyo, November 2–7)*.
2. Kablov, E.N., Petrushin, N.V., Svetlov, I.L., Demonis, I.M. (2007) Cast high-temperature nickel alloys for promising aviation gas-turbine engines. *Tekhnologiya Lyogkikh Splavov*, **2**, 6–16 [in Russian].
3. Kablov, E.N., Petrushin, N.V., Elyutin, E.S. (2011) Single-crystal high-temperature alloys for gas turbine engines. *Vestnik MGU, Ser. Mashinostroenie*, 38–52 [in Russian].
4. (2006) *Cast blades of gas turbine engines (alloys, technology, coatings)*. Ed. by E.N. Kablov. 2nd Ed. Moscow, Nauka [in Russian].

5. Kopelev, S.Z., Galkin, M.N., Kharin, A.A., Shevchenko, I.V. (1993) *Thermal and hydraulic characteristics of cooled gas turbine blades.* Moscow, Mashinostroenie [in Russian].
6. Fitzpatrick, G.A., Broughton, T. (1986) «Rolls-Royse Wide Chord Fan Blade». In: *Proc. of Int. Conf. on Titanium Products and Applications (San Francisco, California, USA, October 1986).*
7. Yushchenko, K.A., Zadery, B.A., Gakh, I.S. et al. (2018) Prospects of development of welded single-crystal structures of high-temperature nickel alloys. *The Paton Welding J.*, **11–12**, 83–90.
8. Wang, N., Mokadem, S., Rappaz, M., Kurr, W. (2004) Solidification cracking of superalloy single- and bi-crystals. *Acta Materialia*, **52**, 3137–3182.
9. Park, J.W., Vitec, J.M., Bobu, S.S., David, S.A. (2004) Stray grain formation, thermomechanical stress and solidification cracking single crystal nickel base superalloy weds. *Sci. and Technol. of Welding and Joining*, 9(**6**), 472–482.
10. Anderson, T.D., DuPont, J.N. (2011) Stray grain formation and solidification cracking susceptibility of single crystal Ni-base superalloy CMSX-4. *Welding J.*, **2**, 27–31.
11. Yushchenko, K.A., Zadery, B.A., Zvyagintseva, A.V. et al. (2008) Sensitivity to cracking and structural changes in EBW of single crystals of heat-resistant nickel alloys. *The Paton Welding J.*, **2**, 6–13.
12. Yushchenko, K.A., Zadery, B.A., Gakh, I.S. et al. (2013) On nature of random orientation of grains in welds of single crystals of high-temperature nickel superalloys. *Metallofizika i Novejshie Tekhnologii*, 35(**10**), 1347–1357 [in Russian].
13. Yushchenko, K.A., Zadery, B.A., Gakh, I.S. et al. (2013) Influence of weld pool geometry on structure of metal of welds of high-temperature nickel alloy single crystals. *The Paton Welding J.*, **5**, 45–50.
14. Zvyagintseva, A.V. (2007) *Structural and phase transformations in high-temperature nickel alloys and their role in formation of cracks in welded joints*: Syn. of Thesis for Cand. of Tekh. Sci. Degree. Kyiv [in Russian].
15. (1961) *Radiography in physical materials science.* Ed. by Yu.A. Bagryansky. Moscow, Metallurgizdat [in Russian].
16. Krivoglaz, M.A. (1983) *Diffraction of X-ray beams and neutrons in abnormal crystals*. Kyiv, Naukova Dumka [in Russian].
17. Karasevskaya, O.P. (1999) Orientation X-ray experimental method of phase analysis. *Metallofizika i Novejshie Tekhnologii*, 21(**8**) [in Russian].
18. Panin, V.E., Egorushkin, V.E., Panin, A.V. (2006) Physical mesomechanics of deformable solid body as the multilevel system. I: Basic physics of multilevel approach. *Fizicheskaya Mezomekhanika*, 9(**3**), 9–22 [in Russian].
19. Rybin, V.V. (2002) Fundamentals of formation of mesostructures during developed plastic deformation. *Voprosy Materialovedeniya*, 29(**1**), 11–33 [in Russian].
20. Hall, E.O. (1951) The deformation and ageing of mild steel. III: Discussion of results. *Proc. Phys. Soc. B.*, **64**, 747–753.
21. Petch, N.J. (1953) The cleavage strength of polycrystals. *J. Iron Steel.*, **174**, 25–28.
22. Trefilov, V.I., Milman, Yu.V., Firstov, S.A. (1975) *Basic physics of strength of refractory metals*. Kyiv, Naukova Dumka [in Russian].
23. Jin-lai, Liu et al. (2011) Influence of temperature on tensile behavior and deformation mechanism of Re-containing single crystal superalloy. *Transact. Nonferrous Met. Soc. China*, **21**, 1518−1523.

ORCID

K.A. Yushchenko: 0000-0002-6276-7843,
I.S. Gakh: 0000-0001-8576-4234,
G.V. Zviagintseva: 0000-0002-6450-4887,
T.O. Aleksiienko: 0000-0001-8492-753X

CONFLICT OF INTEREST

The Authors declare no conflict of interest

CORRESPONDING AUTHOR

I.S. Gakh
E.O. Paton Electric Welding Institute of the NASU
11 Kazymyr Malevych Str., 03150, Kyiv, Ukraine
E-mail: gakh@paton.kiev.ua

SUGGESTED CITATION

K.A. Yushchenko, B.O. Zaderii, I.S. Gakh, G.V. Zviagintseva, T.O. Aleksiienko (2022) Destruction of welded joints of single-crystal high-temperature nickel alloys at tensile testing. *The Paton Welding J.*, **2**, 26–32.

JOURNAL HOME PAGE

https://pwj.com.ua/en

Received: 02.12.2021
Accepted: 31.03.2022

https://doi.org/10.37434/tpwj2022.02.05

STUDIES OF COATINGS PRODUCED BY HIGH-VELOCITY OXY-FUEL SPRAYING USING CERMET POWDER BASED ON FeMoNiCrB AMORPHIZING ALLOY

Yu.S. Borysov, N.V. Vihilianska, I.A. Demianov, A.P. Murashov, O.P. Gryshchenko

E.O. Paton Electric Welding Institute of the NASU
11 Kazymyr Malevych Str., 03150, Kyiv, Ukraine

ABSTRACT

The process of producing composite powders based on amorphizing Fe-alloy with the additives of refractory compounds by the method of high-velocity oxy-fuel spraying was investigated. For spraying composite powders FeMoNiCrB–(Ti, Cr)C, FeMoNiCrB–ZrB_2 were used, produced from a mixture of powders of the compositions by mechanical alloying in a planetary mill. As a result of spraying, dense coatings (porosity is less than 3 %) were produced, which were formed from partially deformed particles with a multiphase structure and a uniform distribution of structural components. The results of X-ray diffraction phase analysis indicate the formation of amorphous-crystalline structure in the produced composite coatings. On the X-ray patterns, the maximum peak amplitude from the crystalline phase against the background of the amorphous halo corresponds to the TiCN phase in the coating FeMoNiCrB–(Ti, Cr)C and the ZrB_2 phase in the FeMoNiCrB–ZrB coating. The size of the measured microhardness for the composite coating FeMoNiCrB–(Ti, Cr)C amounts to — 5.5±0.25 GPa, and for the coating FeMoNiCrB–ZrB_2 it is 5.9±0.29 GPa.

KEY WORDS: high-velocity oxy-fuel spraying, amorphous phase, amorphous iron-based alloy, composite powder, composite coating, microstructure, microhardness

INTRODUCTION

Amorphous metallic iron-based materials are widely used in industry due to their advantages, such as high strength and hardness, excellent corrosion and wear resistance, good magnetic properties, as well as relatively low cost of material [1–3]. However, a disadvantage of amorphous compact materials is their low ductility and excessive brittleness at room temperature, as well as low efficiency of equipment and high production costs, which significantly limits their practical application as structural materials [4]. To eliminate these disadvantages, materials based on amorphous alloys are used on the surface of products in the form of protective coatings, which are produced by thermal spraying. The basis for the scientific and practical interest of the use of amorphous iron-based coatings and amorphous composite coatings in order to increase the stability of the surface of products is the cooling rate in thermal spraying of the powder melt particles, which is 10^5–10^6 K/s and is sufficient for amorphization of the coating material. In addition, amorphous metal coatings can be applied on large-sized and complex parts. This allows expanding the scope of their practical application.

For deposition of coatings from amorphizing iron-based alloys, the methods of plasma, detonation, electric arc and high-velocity oxy-fuel (HVOF, HVAF) spraying are used. The produced coatings are used to increase the corrosion stability of containers for storage and transportation of spent nuclear fuel as an alternative replacement of expensive nickel and titanium alloys [5]; on parts operating in the conditions of corrosion, corrosion-erosion and abrasive wear for replacement of galvanic chrome plating [6, 7]; on parts of mobile warehouses [8]; to strengthen and restore the pipes of industrial boilers, operating in the conditions of high-temperature erosion wear [9]. The process of HVOF spraying is most widely used to produce coatings with an amorphous structure due to the use of a relatively low temperature and high jet velocity in this method, which results in the formation of a coating with a high density and adhesion strength with the base.

Along with the use of iron-based alloys, composite coatings with an amorphous matrix are developed, which was strengthened by the second phase. As reinforcing additives, TiN nitrides, B_4C and WC carbides, CrB_2 borides, Al_2O_3 oxides, as well as stainless steel, NiCr, etc. are used [10–14]. These composite coatings show a significant increase in hardness, wear resistance and corrosion resistance as compared to the basic analogue.

In this paper, a study of the structure formation and phase composition of composite coatings, produced by HVOF based on Fe-alloy, which is amorphised, with reinforcing additives of refractory compounds (Ti, Cr)C, $ZrBr_2$, was carried out.

Copyright © The Author(s)

Table 1. Characteristics of powders for oxy-fuel spraying of coatings

Composition, wt.%	Particle size, μm	Method of producing
FeMoNiCrB (36.2Fe–29.9Mo–23.6Ni–7.6Cr–2.7B)	<40	Spraying of melt by nitrogen
77 FeMoNiCrB–23 (Ti, Cr)C	<40	MA in PM 1.5 h
75 FeMoNiCrB–25 ZrB_2	<80	

MATERIALS AND PROCEDURES OF INVESTIGATIONS

For HVOF coatings with an amorphous structure, powders based on amorphous alloy FeMoNiCrB were used, produced by mechanical alloying (MA) in a planetary mill (PM) [15]. The characteristics of powders are shown in Table 1.

The spraying was performed in the installation (HVOF) UVShGPN-M1 on the following technological parameters of the process: propane-butane pressure is 4 atm, oxygen pressure is 7 atm, air pressure is 6 atm, nitrogen pressure is 5 atm, spraying distance is 120 mm. The coatings FeMoNiCrB–(Ti, Cr)C and FeMoNiCrB–ZrB_2 were deposited to the substrate NiCr (thickness is 50–100 μm), which was sprayed by electric arc method (wire diameter is 2 mm).

In metallographic examinations, an optical microscope Neophot-32 with a digital photography device was used; measurement of microhardness was carried out in a PMT-3 device. X-ray diffraction analysis (XRD) of coatings was carried out in the installation DRON-UM-1, CuK_α radiation, monochromatic.

RESULTS OF INVESTIGATIONS

Metallographic analysis revealed that coatings produced from all the studied materials have a dense,

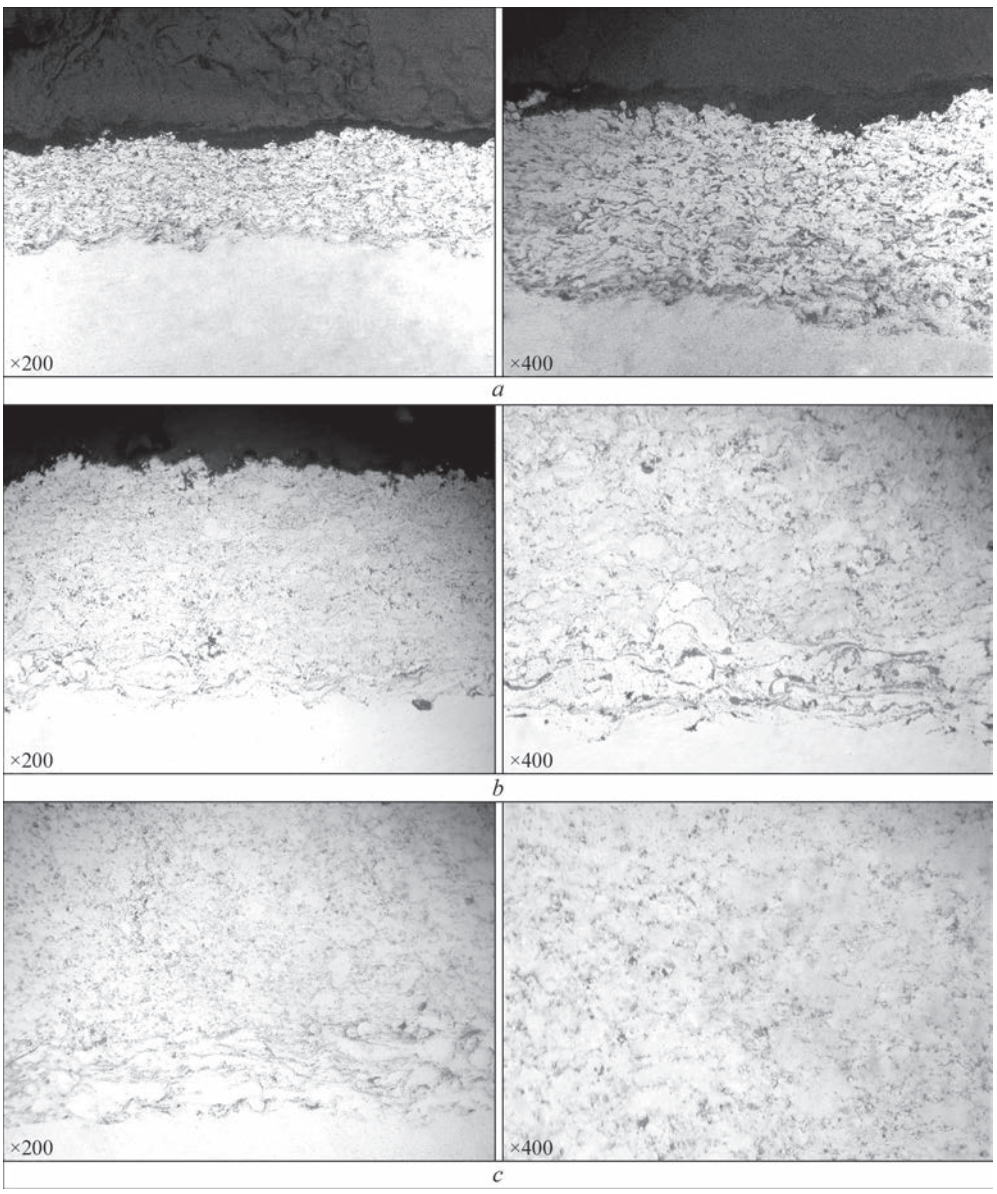

Figure 1. Microstructure of HVOF-coatings: *a* — FeMoNiCrB; *b* — FeMoNiCrB–(Ti, Cr)C; *c* — FeMoNiCrB–ZrB_2

Table 2. Results of investigations of HVOF-coatings based on FeMoNiCrB

Coating material	Thickness, μm	Microhardness $HV_{0.05}$, MPa	Phase composition
FeMoNiCrB	200–250	4390±290	АФ; Mo_2FeB_2; Fe_2B; FeCr; Fe_3O_4; Cr_7Ni_3
FeMoNiCrB–(Ti, Cr)C	300–350	5510±250	АФ; Fe_2Ti; Cr_7Ni_3; $TiC_{0.3}N_{0.7}$; $TiC_{0.2}N_{0.8}$; $Fe_{15.1}C$; Ni_3Fe; phases in small quantities: Ni_3C; MoC; $FeMoO_4$; FeO; FeC_8
FeMoNiCrB–ZrB_2	900–950	5880±290	АФ; ZrB_2; Fe; (Fe, Ni) solid solution; Cr_7Ni_3; $MoNi_4$; Ni_2Zr; phases in small quantities: ZrO_2; Fe_2B; Ni_2B; MoB_2; FeO; $Ni_{0.4}Fe_{2.6}O_4$

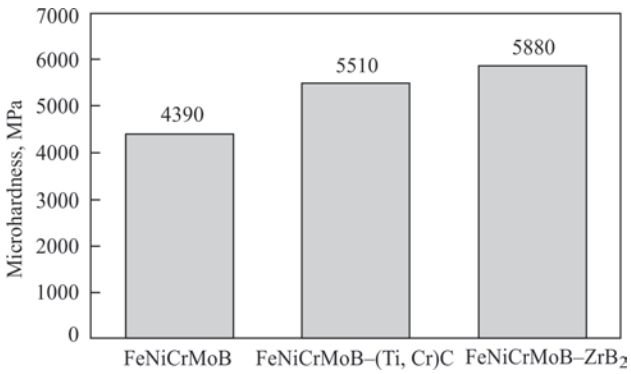

Figure 2. Microhardness of coatings with an amorphised structure produced by the method of HVOF-spraying

fine-grained structure, homogeneous over the whole structure area, which is formed from partially deformed spherical particles (Figure 1). Porosity of the coatings does not exceed 3 vol.%; the coatings FeMoNiCrB–(Ti, Cr)C and FeMoNiCrB–ZrB_2 tightly adhere to the nichrome sublayer and the coating FeMoNiCrB — to the steel base.

Measurement of microhardness of HVOF coatings (Figure 2) showed that the use of reinforcing additives (Ti, Cr)C and ZrB_2 leads to an increase in microhardness of composite coatings by 1120 and 1490 MPa as compared to the coating of the initial FeMoNiCrB powder.

X-ray diffraction analysis revealed (Figure 3) that in the investigated HVOF-coatings, the amorphous phase (APh) is present.

Data from XRD indicate that as a result of HVOF-spraying of powders based on FeMoNiCrB alloy, multiphase coatings were produced, having an amorphous crystalline structure. All the coatings have additional crystalline peaks against the background of halo from the amorphous phase. On X-ray patterns, the maximum peak on the amplitude from the crystalline phase against the background of the amorphous halo corresponds to the phases of Fe_2B and FeCr in the coating FeMoNiCrB; $TiC_{0.3}N_{0.7}$ in the coating FeMoNiCrB–(Ti, Cr)C and the phase ZrB_2, in the coating FeMoNiCrB–ZrB_2. In all the coatings, the intermetallide phase $Cr_7Ni_3$was recorded, having a tetragonal crystalline structure. Iron, as the main ele-

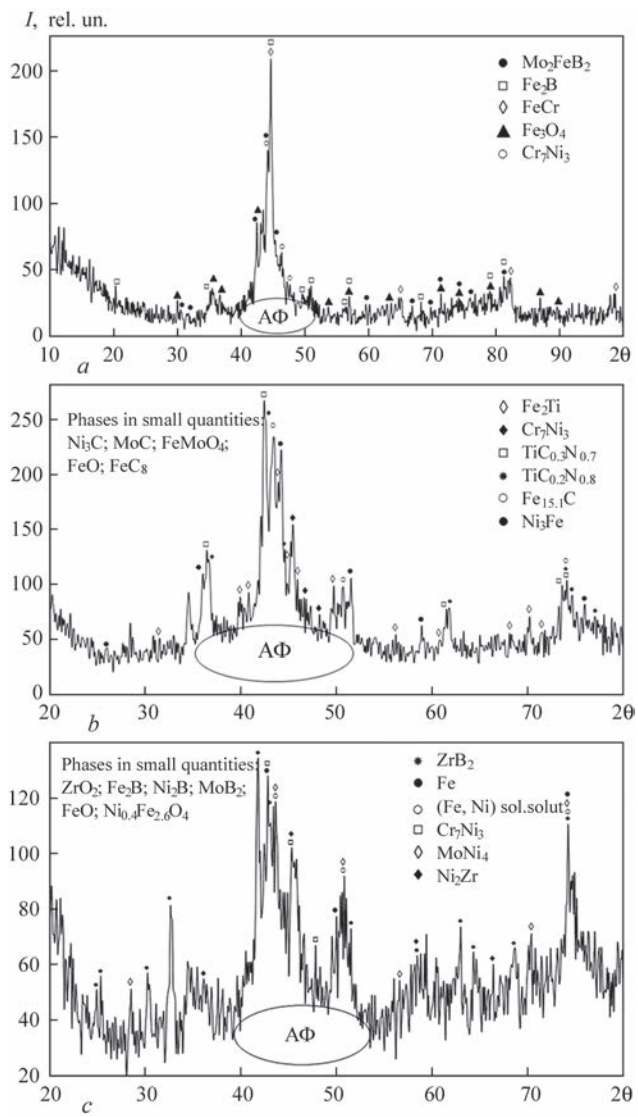

Figure 3. X-ray patterns of HVOF-coatings: *a* — FeMoNiCrB; *b* — FeMoNiCrB–(Ti, Cr)C; *c* — FeMoNiCrB–ZrB_2

ment of the initial alloy, is presented in the coatings in the form of oxides (Fe_3O_4, FeO, $FeMoO_4$,$Ni_{0.4}Fe_{2.6}O_4$), borides (Mo_2FeB_2, Fe_2B), intermetallides (FeCr, Fe_2Ti, Ni_3Fe), carbides ($Fe_{15.1}C$, FeC_8) and (Fe, Ni)-solid solution. In the coating FeMoNiCrB–ZrB_2, iron in a pure form was also revealed.

The obtained results of the study of HVOF-coatings based on the FeMoNiCrB alloy are shown in Table 2.

CONCLUSIONS

Applying the method of high-velocity oxy-fuel spraying using composite powders produced by mechanical alloying based on Fe-alloy that is amorphised, the coatings FeMoNiCrB–(Ti, Cr)C and FeMoNiCrB–ZrB_2 with an amorphous crystalline structure were produced.

The produced coatings are characterized by a uniform distribution of structural components, have a structure, that is homogeneous over the entire area, which is formed from partially deformed spherical particles. The porosity of coatings does not exceed 3 %.

It was revealed that the presence of reinforcing components (Ti, Cr)C, ZrB_2 leads to an increase in microhardness of coatings as compared to the coating of the initial FeMoNiCrB powder by 1120 and 1490 MPa, respectively.

REFERENCES

1. Kim, S.W., Namkung, J., Kwon, O. (2012) Manufacture and industrial application of Fe-based metallic glasses. *Mat. Sci. Forum*, **706–709**, 1324–1330. DOI: https://doi.org/10.4028/www.scientific.net/msf.706-709.1324
2. Yuting, D., Guofeng, M. (2020) Research progress of Fe-based amorphous/nanocrystalline alloys. In: *IOP Conf. Series: Earth and Environmental Science*, **565**, 012048. DOI: https://doi.org/10.1088/1755-1315/565/1/012048
3. Li, H.X., Lu, Z.C., Wang, S.L. et al. (2019) Fe-based bulk metallic glasses: Glass formation, fabrication, properties and applications. *Progress in Mater. Sci.*, **103**, 235–318. DOI: https://doi.org/10.1016/j.pmatsci.2019.01.003
4. Guo, S.F., Liu, L., Li, N., Li, Y. (2010) Fe-based bulk metallic glass matrix composite with large plasticity. *Scripta Materialia*, 62(**6**), 329–332. DOI: https://doi.org/10.1016/j.scriptamat.2009.10.024
5. Blink, J., Farmer, J., Choi, J., Saw, C. (2009) Applications in the nuclear industry for thermal spray amorphous metal and ceramic coatings. *Metallurgical and Materials Transact. A*, **40**, 1344–1354. DOI: https://doi.org/10.1007/s11661-009-9830-4
6. Branagan, D.J. et al. (2006) Wear and corrosion resistant amorphous/nanostructured steel coatings for replacement of electrolytic hard chromium, ITSC. Ed. by B. Marple. In: *Proc. of the 2006 ITSC, ASM Intern., Materials Park, OH.*
7. Lu, W., Wu, Y., Zhang, J. et al. (2010) Microstructure and corrosion resistance of plasma sprayed Fe-based alloy coating as an alternative to hard chromium. *J. of Thermal Spray Technology*, 20(**5**), 1063–1070. DOI: https://doi.org/10.1007/s11666-010-9611-z
8. Artemchuk, V.V., Astakhov, E.A. (2012) Structure and properties of amorphous renewable iron-based coatings. Visnyk NTU KhPI. *Series: New Solutions in Modern Technologies*, **26**, 10–15 [in Ukrainian].
9. Cheng, J.B., Liang, X.B., Chen, Y.X. et al. (2012) High-temperature erosion resistance of FeBSiNb amorphous coatings deposited by arc spraying for boiler applications. *J. of Thermal Spray Technology*, 22(**5**), 820–827. DOI: https://doi.org/10.1007/s11666-012-9876-5
10. Yugeswaran, S., Kobayashi, A., Suresh, K., Subramanian, B. (2013) Characterization of gas tunnel type plasma sprayed TiN reinforced Fe-based metallic glass coatings. *J. of Alloys and Compounds*, **551**, 168–175. DOI: https://doi.org/10.1016/j.jallcom.2012.09.111.
11. Yoon, S., Kim, J., Kim, B.D., Lee, C. (2010) Tribological behavior of B_4C reinforced Fe-base bulk metallic glass composite coating. *Surface and Coatings Technology*, 205(**7**), 1962–1968. DOI: https://doi.org/10.1016/j.surfcoat.2010.08.07
12. Yasir, M., Zhang, C., Wang, W. et al. (2015) Wear behaviors of Fe-based amorphous composite coatings reinforced by Al_2O_3 particles in air and in NaCl solution. *Materials & Design*, **88**, 207–213. DOI: https://doi.org/10.1016/j.matdes.2015.08.142
13. Lampke, T., Wielage, B., Pokhmurska, H. et al. (2011) Development of particle-reinforced nanostructured iron-based composite alloys for thermal spraying. *Surface and Coatings Technology*, 205(**12**), 3671–3676. DOI: https://doi.org/10.1016/j.surfcoat.2011.01.00
14. Wang, S., Cheng, J., Yi, S.-H., Ke, L. (2014) Corrosion resistance of Fe-based amorphous metallic matrix coating fabricated by HVOF thermal spraying. *Transact. of Nonferrous Metals Society of China*, 24(**1**), 146–151. DOI: https://doi.org/10.1016/s1003-6326(14)63040-5
15. Borysov, Yu.S., Borysova, A.L., Burlachenko, O.M. et al. (2021) Composite powders based on FeMoNiCrB amorphizing alloy with additives of refractory compounds for thermal spraying of coatings. *The Paton Welding J.*, **11**, 38–47. DOI: https://doi.org/10.37434/tpwj2021.11.07

ORCID

Yu.S. Borysov: 0000-0002-6019-8464,
N.V. Vihilianska: 0000-0001-8576-2095,
I.A. Demianov: 0000-0003-4536-9971,
A.P. Murashov: 0000-0002-0357-9068,
O.P. Gryshchenko: 0000-0003-2640-8656

CONFLICT OF INTEREST

The Authors declare no conflict of interest

CORRESPONDING AUTHOR

Yu.S. Borysov
E.O. Paton Electric Welding Institute of the NASU
11 Kazymyr Malevych Str., 03150, Kyiv, Ukraine
E-mail: borisov@paton.kiev.ua

SUGGESTED CITATION

Yu.S. Borysov, N.V. Vihilianska, I.A. Demianov, A.P. Murashov, O.P. Gryshchenko (2022) Studies of coatings produced by high-velocity oxy-fuel spraying using cermet powder based on FeMoNiCrB amorphizing alloy. *The Paton Welding J.*, **2**, 33–36.

JOURNAL HOME PAGE

https://pwj.com.ua/en

Received: 22.11.2021
Accepted: 31.03.2022

https://doi.org/10.37434/tpwj2022.02.06

DESIGN FEATURES OF MOBILE RAIL WELDING MACHINES FOR FLASH BUTT WELDING

D.I. Malysheva, N.A. Vynogradov, V.Yu. Sysoyev

E.O. Paton Electric Welding Institute of the NASU
11 Kazymyr Malevych Str., 03150, Kyiv, Ukraine

ABSTRACT

The design features of mobile rail welding machines for flash butt welding produced by the companies, operating at the modern world market were studied. The studies provide an opportunity of highlighting the trends of further improvement of equipment with the growth of technological innovations.

KEY WORDS: seamless track, flash butt welding of rails, rail welding machine, upsetting, upsetting force, clamping, clamping force, continuous flashing, pulsating flashing, flash remover, current supply

INTRODUCTION

Seamless track is the most advanced and reliable design of a track for modern operating conditions. Rails, being a part of such a track, have no butt joints and this allows increasing the admissible speeds of trains to 160–200 km/h and more. At laying of seamless tracks and also during their repair, rails are welded in lengthy strings. Standard documents allow using only flash butt welding for joining rails in the main line, which provides an equal strength of welded joints with the base metal, including as well the values of fatigue strength [1]. Strings are welded either by stationary machines at rail welding plants and then delivered to the site of assembly, or on the track — by mobile rail welding complexes.

The global market of flash butt welding machines amounts to thousands of units of equipment and the profit market is millions of US dollars.

In 2020, the consulting Company QY Research published the report “Global rail welding machines market insights and forecast to 2027” [2]. According to the report, during the forecast period, the revenue of the mobile sector of rail welding machines will be about 70 % of the market share, and of a stationary is only 30 %. The use of stationary rail welding machines is constantly decreasing. Therefore, by 2027 the global market of mobile rail welding machines will reach 82 mln USD as compared to 54 mln USD in 2020 at an average annual growth rate of 2.9 % during 2021–2027.

From the point of view of the market, seamless railway tracks should be safe, and the costs of their laying and maintenance should be minimized. This issue sets increased requirements to the reliability of the equipment design, so it is relevant to carry out the analysis of the technical capabilities of mobile rail welding machines. The authors propose to analyze the design differences of mobile rail welding machines of different manufacturers.

Copyright © The Author(s)

QY Research focuses on the activities of the following companies that are represented at the market of mobile rail welding equipment: Chengdu Aigre Technology (China), Holland LP, Schlatter Group (Switzerland), Goldschmidt (Germany), Mirage Ltd (England), PJSC KZESO (Kakhovka Plant of Electric Welding Equipment) (Ukraine), Progress Rail (Caterpillar) (USA), Geismar (France), Gantrex (Belgium), BAIDIN GmbH (Germany), Vossloh (Germany), Plasser@Theurer (Austria), “Pskovelektrosvar” Company (Russia), Contrail Machinery (Romania), VAIA CAR SPA (Italy).

According to the design, mobile rail welding machines consist of fixed and movable clamps which fix rails with the help of clamping cylinders. The movable clamp can be moved relative to the fixed clamp by means of upsetting cylinders. Welding current from power sources, mounted on the machine, heats rails until a ductile state. Due to the rapid movement of clamped and heated rails, their joining — welding occurs. In this case, a part of the molten metal (flash) remains along the contour of welded rails. Standard documents [3], which determine the requirements for the method of flash butt welding in mobile rail welding machines, do not allow the presence of flash after welding, so in each machine, a device for its removal is provided.

We will not consider the products of Goldschmidt Company, as far as it is specialized on termite and arc welding, as well as Vossloh Company, because the welding head is very similar to the machine of Schlatter Group production.

The PJSC KZESO (Kakhovka Plant of Electric Welding Equipment) produces a wide assortment of mobile rail welding machines, designed at the PWI [1] for construction and repair of seamless high-speed main railways, tram and subway lines in field conditions [4]. The enterprise supplies to the market both welding machines K900 with a lever clamping scheme (Figure 1) as well as machines K920 (Fig-

Figure 1. Mobile rail welding head K900

ure 2), K922-1, K945 and K950 with a horizontal arrangement of clamping cylinders to generate a constant force, that does not depend on wear of tongs. According to the standard documents [5], welding of rails can be carried out in two ways: with a tension of rail string and with a preliminary bending. In welding rails with a preliminary bending, a part of a string is loosen, raised and bent in a horizontal plane until alignment of the ends. In the process of welding, the bend of a string is straightened under the action of longitudinal force, created by a welding machine. Machines K922 (Figure 3), K945, K950 generate an upsetting force of 1200 kN. This makes it possible to eliminate the bend by performing welding of rails into a track with the tension of a string and minimizing the length of a rail, which is removed from sleepers. This simplifies the process of welding, as well as enables the operation of "last welding", that is, welding and equalization of stresses in rails per one operation. Machines [6] consist of two tong clamping devices, manufactured in the form of two double levers, which are mounted on a common central axis and isolated from each other. Two tong clamping devices are made with the possibility of moving along the axis relative to each other using two hydraulic upsetting cylinders, the rods of which bind them. As a source of heating rails, two AC transformers are used, which are built into the machine. An original design of the welding circuit, where as a conductive elements, the power units of the machine are used, which allows reducing the power consumed during welding. Clamping is

Figure 3. Welding machine K922-1

carried out behind the web of rails. If in the machine K900 a flash is removed by travel of the moving column (a throw-on flash remover is used), then in the machines K922, K945 (Figure 4) and K950, in addition to the throw-on, a flash remover with a drive from built-in autonomous hydraulic cylinders is provided. This allows removing flash in a clamped state and maintaining the butt during the period required for cooling. The designing feature of these machines is the presence of clamping multipliers built into the cylinders that increase the pressure, and, accordingly, the clamping force by 2 and more times (the maximum clamping force at the highest working pressure is 2900 kN) to avoid slipping of columns during upsetting. Machines K945 and K950 have an increased travel of upsetting cylinders being 400 and 250 mm, respectively, which eliminates the possibility of a tear in a heated butt during unclamping [7]. All the machines are designed and manufactured, taking into account the features of a pulsed flashing technology, developed at the PWI. The weight of the welding head does not exceed 3500 kg.

Machines are included in a mobile rail welding complex in the form of a 20-foot container, designed for mounting on a base of a cargo car and a railway platform.

It should be noted that the key players at the market of mobile rail welding machines, such as Chengdu Aigre Technology (China), Holland LP, Progress Rail (Caterpillar), Geismar, Gantrex, Contrail Machinery,

Figure 2. Rail welding head K920-1

Figure 4. Welding machine K945

Figure 5. Container system Multiflex for welding rails with welding head AMS60

VAIA CAR SPA, as a welding head in their machines use the equipment that was in different years designed at the PWI and manufactured at the PJSC KZESO.

Schlatter Company offers mobile rail welding machines AMS60, AMS100 and AMS200 in different configurations, that differ with each other by a rail alignment (centering) system and operating range [8].

The AMS60 and AMS200 machines contain a body and a slider that have the ability of linear movement. Clamping systems are mounted in the body and the slider. The eccentric clamping system, activated by clamping cylinders has an ability of self-slipping, which allows increasing the clamping force while adding upsetting force. Clamping is carried out behind the web of rails. By means of the double lever, the upsetting cylinder, located over the axis of rail clamping, can move the slider. Before clamping, an integrated lifting hydraulic device clamps both ends of rails until the rests to carry out vertical alignment (centering) of rails along the rolling surface.

During designing of the AMS60 machine (Figure 5), the main attention was paid to centering — an accurate combination of ends of the rails on the side edge (it is possible to choose from left or right) and the rolling surface. Therefore, this machine is the best used in the situations, where accurate alignment is required, for example for high-speed railways (for rails of up to 68 kg/m). AMS60 has an upsetting force of 6000 kN. The weight of AMS60 is about 6200 kg.

The AMS100 machine (Figure 6) is designed for welding rails of a large cross-section. AMS100 has an upsetting force of 1000 kN and can weld heavy and even tram groove rails. It is often used for welding track of cargo transportation with an axle load of up to 75 kg/m. However, AMS100 was also used for welding high-speed railways. As to kinematic scheme, the welding head AMS100 is identical to K920 machine (design of the PWI).

AMS200 (Figure 7) [9] is a mobile rail welding machine of a new generation that allows performing welding and tension without an additional stretching

Figure 6. Welding head AMS100

device, as well as the operation “last welding”. The tension and upsetting forces are 1400 kN. The machine has a necessary force to pull up rails to the required calculation length. A full travel of clamping cylinders is 300 mm. If necessary, checking and adjustment of accurate side alignment of rails is carried out using an electronic measurement system. The current supply is completely independent of clamping and is carried out on the outer side of the head of rails and their foot. The mass and dimensions of the AMS200 machine does not exceed the mass of AMS60 machine.

The presented machines are available in two variants:

- Supra Road flex is a self-travelling system based on a cargo car, which is designed for fully autonomous operation with the possibility of moving from one site to another by the track or outside it;
- Supra Multiflex allows all equipment to be placed in a container and mounted on the railway platform. For standard complete set, a compact 30-foot container is used.

As an alternative, a system consisting of two 20-foot containers is also available.

Mobile rail-welding machines of the Austrian **Plasser@Theurer** Company of APT500 series are based on the welding head of the PWI design. The new development of the company is a fully automated robot APT 1500R [10]. This means that a welding robot needs only to be lowered to the welding zone, and then the process

Figure 7. Mobile machine AMS200

Figure 8. Welding machine of container type ART1500RC

runs automatically. The design of APT 1500R provides a separate application of welding current and clamping of rails. Rails are lifted from sleepers with the help of lifting devices, centered as to their height and aligned relative to the working edge, and the special measurement system is constantly monitoring this process. Upsetting cylinders clamp the web of a rail until the rests with the force of 3500 kN. Clamping cylinders, upsetting cylinders are located in a one plane passing through a neutral axis of a rail [11]. Such a design solution protects the machine from undesirable loads. The design of the machine allows tension and upsetting of rails — the tension force is 1500 kN. The travel of upsetting cylinder is 200 mm.

The feature of the welding robot is the fact, that it uses an AC source with a frequency of 1000 Hz. The power source consists of AC transformers, whose voltage is rectified by diodes, and then a direct voltage is transformed by inverters back to the alternating but with a frequency of 1000 Hz. This allows using compact transformers, and on the other hand, such a welding voltage has a low residual pulsation, which positively affects the quality of welding [10]. Current conductors are clamped to rails with the use of separate hydraulic cylinders. Current supply is carried out on the bottom part of the head and the top side of the foot of a rail. In the design of the robot, a flash remover with hydraulic cylinders is built-in. Cylinders load a welded butt joint in the direction of compression of a butt (according to the requirements of the standard EN14587-2 [3]) and do not need unclamping. A continuous contactless measurement of temperature of rails provides a precise cooling of a rail in accordance with a set temperature characteristic using pulses of repeated heating. The weight of the welding head is 5500 kg.

Figure 9. Machine B120AC

The welding robot welds rails laid in a string, and can produce closing and final welded butt joints.

There are three modifications of a welding robot:

- Machine for flash butt welding APT 1500 RA. This four-axle machine is built into a railway rolling stock of a standard design;
- ART1500RC is a container-type welding machine (Figure 8);
- ART 1500RL is a welding robot on the automobile platform. Moreover, the limit mass of the structure does not exceed 32 t for transportation on the roads of Europe.

The German Company **BAIDIN GmbH** produces rail welding machines for flash butt welding of rails [12]. The main products of this company is a container complex on the base of welding heads K355AM, which as to the kinematic scheme is identical to the machine K900A and B120AC (Figure 9), which as to its design is the same as K920. All these machines are based on the developments of PWI. For power supply of welding transformers, in this case power inverter transformers are used, which transform a three-phase voltage of a diesel generator into a single-phase sinusoidal voltage with a frequency of 50 Hz. According to the manufacturer, this solution provides a uniform load (without voltage unbalance) on a diesel generator plant and stabilizes the voltage of welding transformers. The upsetting force is 1200 kN, and the maximum clamping force is 2800 kN. The weight of the welding head is 3800 kg.

As to its design, the universal head A150DC for welding rails resembles a welding head ART1500R of the Plasser@Theurer Company and differs by the fact that it has eight clamping cylinders, which are arranged opposite one another relative to the longitudinal axis. Such a layout allows performing an accurate centering of rails during clamping, because the piston cavities of the counter cylinders are joined in pairs. Flashing of rails in it is carried out by a direct current using two rectified units. The travel of clamping cylinders is 250 mm, which allows performing the operation of “last welding”. The maximum clamping force is 4000 kN, the upsetting force is 1500 kN. The weight of welding head is 4200 kg.

In 2019, at the exhibition RailLive 2019, an induction welding machine of **Mirage Rail** Company was demonstrated, which was designed for Nerwork Rail, Great Britain [13]. Unlike flash butt welding, in induction welding, the ends of rails are not heated until a molten metal and maintained in a solid state. Heating

Figure 10. Induction welding robot of Mirage Rail Company

of rails is carried out throughout the whole perimeter by the currents of magnetic induction with the help of inductors. The power consumption is 150 kVA.

The device consists of a support [14], where two modules are built-in: movable and fixed. Each module includes three separate clamping heads and two heads of vertical lifting. Clamping and lifting heads are of a lever type with double levers. When designing the device, the attention was paid to the accurate alignment of rails in three projections. This is necessary to reduce the stress in welded rails during the process. After welding, flash remover built into the device is moved using two autonomous hydraulic cylinders and removes a flash.

The device is designed for welding rails CEN 56 and 60. The time of welding is 6 min, the mass of the device is 2200 kg (Figure 10).

Russian Company **"Pskovelektrosvar"** [15] is represented at the market by two mobile machines: MSR-80.01 (Figure 11) and MSR-12001A (Figure 12), designed for continuous or pulsating flash butt welding of rails R50 and R65.

Machine MRS-80.01 [16] consists of fixed and movable bodies. Each body contains power and electrode levers with different leverage systems. Power levers perform clamping of rails. The clamping force is 2100 kN. Electrode levers perform centering of rail ends and supply current to the web of a rail. The upsetting force is 800 kN. The weight of the machine is 3800 kg.

Figure 12. Mobile machine MSR-12001.01

Unlike MRS-80.01, in MRS 12001A [17] between the power and electrode levers, the combination mechanism is located, the levers of which are joined to the power levers, and the electrodes have the ability to rotate in two projections with self-positioning over the web of a rail and provide a reliable electrical contact. The mechanism of combination is designed to increase the accuracy of rail centering. Machine MSR-12001A can perform welding of rails with a tension with the flash removal directly after welding. The rated clamping force is 2800 kN, and the upsetting force is 1200 kN. The weight of the welding head is 3750 kg.

These machines are designed for operation in the composition of complexes of type PRSM.

The authors would like to draw the attention of readers to the new development of the PWI (Figure 13) [18]. The design feature of this machine is the fact that a number of axes joining clamping tong-type devices between each other was reduced from three to one. This allowed reducing a number of upsetting cylinders to one. The upsetting force of the machine is 65 kN. The machine is positioned as a machine for welding rails in hard-to-reach places, as well as for welding rails in the string in field conditions and on mobile rail welding plants. This machine requires

Figure 11. Mobile machine MSR-80.01

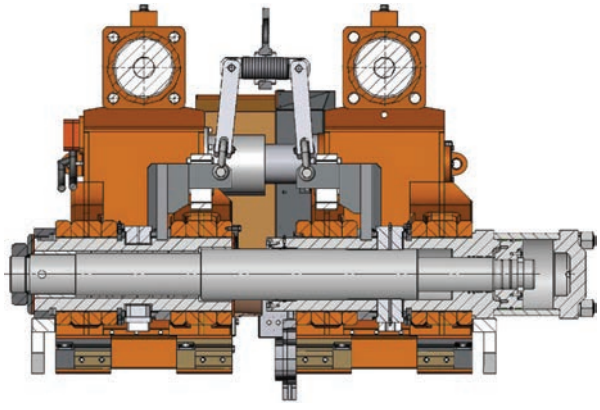

Figure 13. Universal rail welding machine

only a 215 mm gap to the nearest rail, which allows using it even for welding of switching transfers.

All mobile machines independently of the manufacturer have control systems that are manufactured based on an industrial computer and provide tasks and control of welding process parameters, providing the operator with up-to-date information on the technological process of welding with a subsequent issuing passport for each welded butt joint. Simultaneously in the built-in PC, the results of welding works are archived.

Therefore, modern technical products acquire the features of the investment project and a designer has a task not only to create the new equipment, but also to optimize expenses for all stages of manufacturing products, such as designing, development and manufacturing. The analysis of the gained experience of design and operation of welding machines allows outlining the further ways of improving and developing equipment designs, taking into account also economic components.

CONCLUSIONS

1. The trend of the development of the world market of rail welding machines is featured by an increase in the share of mobile equipment for using in field conditions during construction and repair of railways.

2. Mobile machines for welding rails vary by a kinematic scheme, according to which clamping and upsetting by centering and heating method of rails are performed. Each technical solution has its advantages and disadvantages.

3. Basic designing solutions of mobile rail welding machines, presented at the market, are developed at the PWI and used by domestic and foreign manufacturers of this industry, each of which improves individual assemblies and mechanisms in order to expand the technological characteristics.

4. The latest development of the PWI in the field of mobile rail welding machines is positioned as a machine for welding rails in hard-to-reach places, as well as for welding rails in the string in field conditions and at mobile rail welding plants.

REFERENCES

1. Kuchuk-Yatsenko, S.I., Didkovsky, A.V., Shvets, V.I. et al. (2016) Flash-butt welding of high-strength rails of nowadays production. *The Paton Welding J.*, **5–6**, 4–12 DOI: https://doi.org/10.15407/tpwj2016.06.01
2. *Report "Global rail welding machines market insights and forecast to 2027"*. https://www.qyresearch.com/index/detail/2731611/global-rail-welding-machines-market/toc
3. EN 14587-2:2009: *Railway applications — Track — Flash butt welding of rails.* Pt 2: New R220, R260, R260Mn and R350HT grade rails by mobile welding machines at sites other than a fixed plant. European Committee for standardization.
4. *Kakhovsky Plant of Electric Welding Equipment*: Catalog of Products. https://kzeso.com
5. TsP-0266: *Technical instructions for the arrangement, repair and maintenance of seamless track on the railways of Ukraine* [in Ukrainian].
6. Kuchuk-Yatsenko, S.I., Sakharnov, V.O., Kryvenko, V.G., Porkhun, F.K., Bogorskyi, M.V. *Machine for flash-butt welding of rails*. Pat. Ukraine UA56986C2 [in Ukrainian].
7. Kuchuk-Yatsenko, S.I. (2018) Technologies and equipment for flash-butt welding of rails: 60 years of continuous innovations. *The Paton Welding J.*, **11–12**, 25–40. DOI: https://doi.org/10.15407/tpwj2018.12.03
8. *Schlatter Company: Catalog of Products*. https://www.schlattergroup.com/en/welding-machines/flashbutt-welding-machines-for-rails
9. *Flash butt welding facility.* Hansrudof Zollinger, Geroldswil, Switzerland, assignor to H. A. Schlatter AG, Schlieren, Switzerland. USA Pat. US5,389,760.
10. *Plasser @ Theurer Company: Catalog of Products*. https://www.plassertheurer.com/en/machines-systems/infrastructure/industrial-railways/infrastructure/save
11. Fheurer, J., Zichtberger, B., Mühlleither, H. *Welding rails of a track.* USA Pat. US8735761B2.
12. *Baidin GmbH Company: Catalog of Products*. https://baidin-gmbh.com/
13. *Design and Build House "Mirage": Catalog of Products.* https://www.mirageservices.co.uk
14. Birks, Kevin Finnemore, Mark Ross Mountford, Nicholas John. *Railway rail induction-welding device*. USA Pat. US2019330805A1.
15. *"Pskovelektrosvar" Company: Catalog of Products*. http://pskovelectrosvar.ru/products/0_30/
16. Krizsky, V.M., Zhuravlev, S.I., Sudarkin, F.Ya. *Suspended flash-butt rail welding machine*. Russia Pat. RU2748185C1.
17. Krizsky, V.M., Zhukov, S.A., Zimin, I.N. et al. *Suspended flash-butt rail welding machine*. Russia Pat. RU2321478C2 [in Russian].
18. Kuchuk-Yatsenko, S.I., Krivenko, V.G., Didkovskiy, A.V. et al. *Machine for flash-butt welding of rails*. USA Pat. US 10,131,014 B2.

ORCID

D.I. Malysheva: 0000-0001-9058-1053

CONFLICT OF INTEREST

The Authors declare no conflict of interest

CORRESPONDING AUTHOR

D.I. Malysheva
E.O. Paton Electric Welding Institute of the NASU
11 Kazymyr Malevych Str., 03150, Kyiv, Ukraine
E-mail: dep26kb@paton.kiev.ua

SUGGESTED CITATION

D.I. Malysheva, N.A. Vynogradov, V.Yu. Sysoyev (2022) Design features of mobile rail welding machines for flash butt welding. *The Paton Welding J.*, **2**, 37–42.

JOURNAL HOME PAGE

https://pwj.com.ua/en

Received: 24.12.2021
Accepted: 31.03.2022

https://doi.org/10.37434/tpwj2022.02.07

STRUCTURE AND CORROSION PROPERTIES OF COPPER- AND TUNGSTEN-BASED COMPOSITE MATERIALS, PRODUCED BY HIGH-RATE EVAPORATION-CONDENSATION

M.I. Grechanyuk[1], **V.G. Grechanyuk**[2], **I.M. Grechanyuk**[3], **V.O. Chornovol**[2]

[1]I.M. Frantsevich Institute for Problems of Materials Science of the NAS of Ukraine
3 Krzhizhanovskyi Str., 03142, Kyiv, Ukraine
[2]Kyiv National University of Construction and Architecture
31 Povitroflotskyi Ave., 03037, Kyiv, Ukraine
[3]NVP «ELTEKHMASH»
25 Vatutin Str., 21011, Vinnytsya, Ukraine

ABSTRACT

Structure, corrosion resistance, and mechanical properties of Cu–W composite materials used for various-purpose electric contacts were studied. Shown is the influence of tungsten concentration in Cu–W composite material on these properties. Gravimetric dependencies of Cu–W composite materials with different tungsten content are given and composition of the corrosive environment before and after corrosion testing is determined.

KEY WORDS: structure; corrosion resistance; mechanical properties; composite materials; tungsten; copper

INTRODUCTION

In economic terms, the main materials for electric contacts of various purposes are available, for example, those used in construction machines and devices (elevators, building cranes, lifting machines, cutoff switches, etc.). They are based on copper and alloys and have high strength characteristics. Such contacts are made either of cast as well as of rolling materials (plates, sheets, rods, wires), or from materials produced by the methods of powder metallurgy. Cast alloys have a number of significant drawbacks, such as low strength characteristics, stability to bridging, arc-extinguishing properties, etc. Contacts made by the methods of powder metallurgy, are characterized by high strength characteristics and higher electric contact properties, but their significant disadvantage is the complexity of their manufacturing technology, which includes several operations: producing powders of the required composition; compacting these powders; sintering or their gas-static pressing at high temperatures in a controlled environment; formation of required sizes, etc. [1].

In producing condensed composite materials for electric contacts, it is economically substantiated to use the method of a high-rate electron beam evaporation and condensation of metals and nonmetals in vacuum [2–7]. The technological advantages of this method consist in the fact that by evaporation of simultaneously several substances, by mixing of their steam flows and condensation on the substrate, such ratios of components can be obtained and such structures can be created that are very difficult or almost impossible to be produced by traditional ways.

Copyright © The Author(s)

A great importance in the development of means of switching high-power currents, especially in high-voltage switches belongs to composite materials based on copper and refractory metals — tungsten or molybdenum. For copper-tungsten contacts, such properties are typical as refractoriness, hardness, arc resistance, resistance against welding-on, mechanical strength at room and elevated temperatures, good heat removal and electric conductivity [8]. Today, the information about the structure and mechanical properties of contacts from composite materials based on copper and tungsten is available [9–11]. However, the information about the corrosive stability of composite Cu–W materials (CM) and its relation with the structure is not available at all.

Proceeding from the abovementioned, the aim of this work is to study the structure, physico-mechanical properties and corrosion resistance of copper-tungsten composite materials for electric contacts of various purposes, produced by the method of electron beam evaporation-condensation in vacuum.

PROCEDURE OF INVESTIGATIONS

Composite Cu–W materials were produced on a stationary substrate manufactured of St3, 250×220×10 mm in size at 900 ± 30 °C (temperature remained unchanged for all experiments) by electron beam evaporation and subsequent condensation in vacuum [2–5].

Corrosion resistance of condensates was investigated by gravimetric method [12]. After preliminary treatment, the specimens with an area of 100 mm^2 were immersed in a corrosive environment (water)

Table 1. Chemical composition of CM copper-tungsten, used for investigations, wt.%

Specimen	W	Cu
1	0.64	Rest
2	3.57	
3	8.27	
4	15.23	
5	20.39	
6	32.98	

per 100 h. The control of the change in the mass of the specimens was carried out every 20 h. The investigations were carried out in a static mode. To study the structure of the produced condensates, macro- and microstructural analyses by optical and electronic scanning microscopy were used [13].

The corrosion resistance and structure of copper-tungsten condensates were studied for six compositions of specimens with a tungsten content from 0.64 to 32.98 wt.% (Table 1).

RESULTS OF INVESTIGATIONS

The carried out investigations of microstructure of Cu–W condensates showed that the structure of the latter varies from homogeneous at a concentration of tungsten to 1 % to laminated with an increase in tungsten concentration in composite materials to 32.98 wt.%.

It should be noted that the higher the concentration of tungsten in the specimens, the lamination appears to be more expressive. For example, let us consider a structure of CM at a concentration of tungsten in it being 20.39 wt.% (Figure 1).

With the increase of tungsten content in the condensate, its distribution in layers is nonuniform (Figure 2).

For composite Cu–W materials, the predominant morphological type of layer structure is polygonal (equiaxial grains). For layers enriched with copper, near the substrate a column structure is characteristic (Figure 3).

Such a nonuniform nature is manifested in the form of concentration clusters, which, as can be assumed, are nuclei for the formation of a new column structure. In the composites with tungsten content of up to 20.39 wt.%, these columns have a conical shape and spheroidal apexes. With an increase in tungsten content, in the condensate with the mass of up to 32.98 wt.%, they become continuous, their share in the section of the specimens grows, and the height is comparable with the thickness of macrolayers.

According to the experimental data [14], electric conductivity of the specimens with an increase in tungsten content in them naturally falls, for example, with a tungsten content of about 10 wt.%, it amounts to 80 % of the electric conductivity of a pure copper.

Mechanical properties during tests of the condensate on tension are also changing. The yield and tensile strength are growing, the characteristics of ductility decrease with an increase in tungsten content in composite materials (Figure 4).

As is seen from Figure 4, the dependence between the tensile (σ_t) and yield strength ($\sigma_{0.2}$), as well as relative elongation (δ) from the concentration of tungsten, have a monotonous nature. An increase in the values

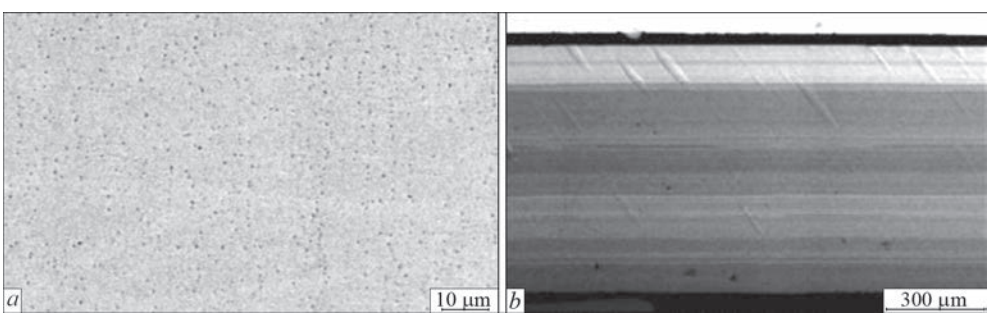

Figure 1. Microstructure of composite Cu–W materials at a concentration of W, wt.%: *a* — 0.64; *b* — 20.39

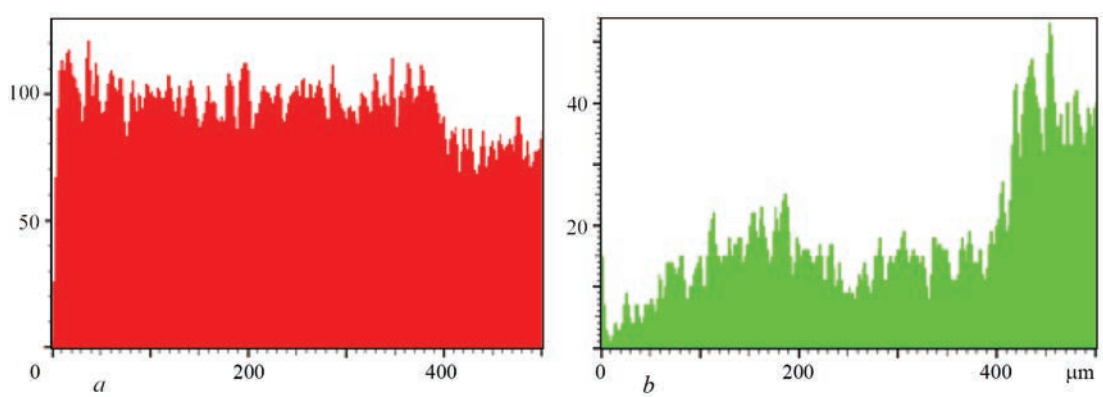

Figure 2. Distribution of copper (*a*) and tungsten (*b*) components in CM Cu — 20.39 % W

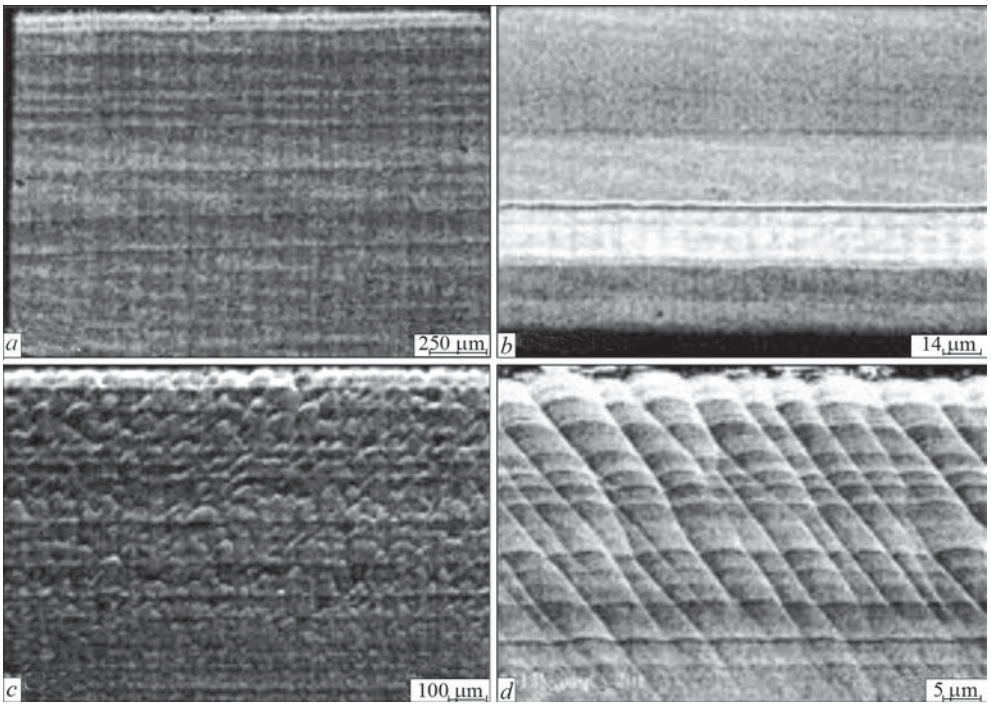

Figure 3. Structure of CM Cu–W specimens with different content of tungsten, wt.%: *a* — laminated (3.57); *b* — laminated with traces of local enrichment (8.27); *c* — cone-shaped (15.23); *d* — column (32.98)

of σ_t and $\sigma_{0.2}$ with an increase in the content of W and a reduction in δ from 30.2 to 2.2 % at a concentration of the latter being 32.98 wt.% is observed. Reducing the ductility, which is observed for the specimens with a significant tungsten content, is predetermined by the influence of defects of "rods" type, which penetrate the entire thickness of the condensate, as was shown in preliminary studies [14].

The fall in ductility with an increase in tungsten content (above 20.39 %) correlates with the peculiarities of the structure of condensates. A macrolayer enriched in copper, formed on the substrate, on which vapours of metals are condensed, is subjected to viscous fracture. The change in properties affects also by weakened impurities of the boundary interface of macrolayers and rods, that serve either as origins of fracture, or determine the direction of a fracture movement [14].

Since the fracture of contacts occurs not only during operation in switching on/off mode, but also in the non-working condition at the action of the environment, gravimetric corrosive studies of composite materials copper-tungsten in water, simulating 100 % moisture in accordance with GOST 25927–81 were carried out.

X-ray analysis showed that for the process of corrosion of Cu–W composites in the atmospheric conditions, on the surface copper and tungsten oxides are formed.

According to the results of previous studies it is known that in case of using the contacts of the Cu–W system, the oxidation products are most often WO_3 and Cu_2O oxides. The study of the surface before and after corrosion tests showed the presence of oxygen content from 10 to 31 % on the surface of condensates after corrosion tests. At the same time, the presence of oxygen on the surface of the specimens before corrosion tests was not recorded.

The mechanism of electrochemical corrosion consists in arising of short-circuited microgalvanic elements with different micro-EMF (electromotive force) values on the surface of metals, which arises as a result of the difference in electrode potentials of copper and tungsten. The areas of surfaces of metals are characterized by different potentials not only in the presence of different electrode potentials of metals, but also as a result of various concentrations of structural defects, various treatments (roughness) of the surface, concentrations of impurities, thickness of adsorbed moisture films, dissolved oxygen concentrations in moisture films, etc. Therefore, for composite materials copper-tungsten, the presence of microgalvanic couples between copper and tungsten in areas

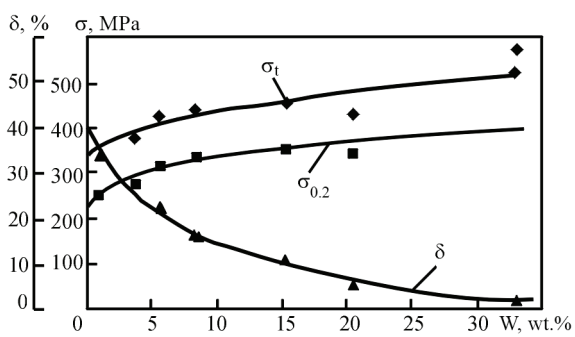

Figure 4. Dependence of tensile strength (σ_t), yield strength ($\sigma_{0.2}$) and relative elongation (δ) of Cu–W composites from tungsten content (after vacuum annealing 1173 K, 1 h) at a temperature of 293 K

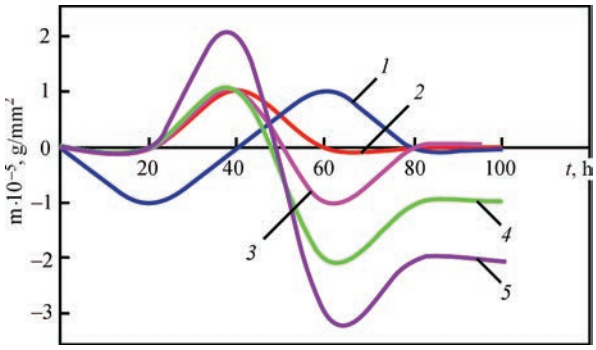

Figure 5. Gravimetric dependencies of Cu–W composites with a different content of tungsten, wt.%: *1* — 0.64; *2* — 8.27; *3* — 15.23; *4* — 20.39; *5* — 32.98

enriched with tungsten is possible. In this case, an anode ionization of more active metal — tungsten occurs. On the rest of the surface areas, formation of galvanic couples between copper with copper ionization and the transition of its ions into a solution is possible. This is evidenced by the analysis of the environment carried out before and after corrosion tests (Table 2).

As is seen from the given data, in the corrosive environment, ions of copper and tungsten are present.

With an increase in the content, in the Cu–W composites of tungsten, the concentration of tungsten ions in the environment increases and that of copper ions remains approximately the same. As it should be expected, the highest concentration of copper is present in the solution at a lower content of tungsten in the specimens.

Gravimetric studies showed that in the initial moment of corrosion tests, a slight decrease in the mass of the specimens occurs regardless of their composition, which is predetermined by ionization and transition to the solution of copper and tungsten ions. After 20 h of tests, an increase in the mass of the specimens begins. With an increase in the concentration of tungsten in the Cu–W composites, the process becomes more intense (Figure 5).

This is connected with the impossibility of the unlimited increase in the concentration of metal ions in the solution in connection with the formation of soluble compounds — copper and tungsten oxides.

Table 2. Composition of corrosion environment before and after the corrosion tests

Composition of composites, wt.%		Content of components in water after corrosion investigations, mg/l	
W	Cu	Cu	W
0.64	Rest	1.299	0.003
3.57		0.924	0.006
8.27		0.788	0.014
15.23		0.687	0.016
20.39		0.704	0.018
32.98		0.750	0.209
Initial water — 0.014			0

In addition, with an increase in the concentration of tungsten in the composites, also the formation of low-soluble salts of copper tungstates is possible.

Thus, the growth of the film formed from low-soluble compounds becomes more intense with an increase in the concentration of tungsten in the composites and the weight of the specimens respectively becomes higher. The formed film shields the metal surface, diffusion limitations of anode reaction in this case are deepened and the rate of corrosion is reduced. During the fracture of metals in natural atmospheric conditions, an oxygen depolarization reaction proceeds on the cathode. Taking into account a small solubility of oxygen in water (approximately 0.008 g/l), diffusion limitations occur during this reaction. Therefore, the rate of corrosion with oxygen depolarization is limited by the rate of supply of oxygen molecules to the surface of the corroded metal. This is also one of the reasons for inhibiting the corrosion process.

Reduction in the rate of running corrosion processes is indicated by studying the structure of the specimens with different tungsten content before and after corrosion tests (Figure 6).

The nature of fracture of the composites with molybdenum content of up to 3.57 wt.% is the same for all the specimens. The corrosion processes are observed mainly in those regions where structural defects are present. At the concentrations of tungsten being 15.23–32.98 wt.%, corrosion was not recorded (Figure 6, *b*).

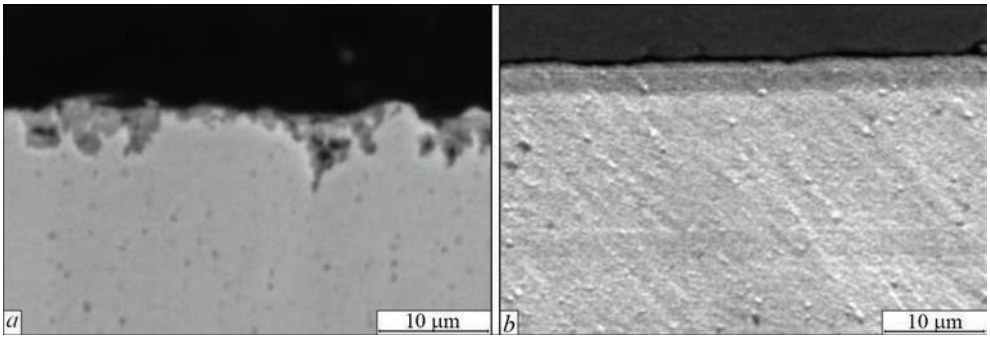

Figure 6. Destruction of composites with different content of tungsten, wt.%: *a* — 3.57; *b* — 15.23

CONCLUSIONS

1. The study of chemical composition, structure and properties of composite materials copper-tungsten, produced by the method of electron beam evaporation-condensation in vacuum, was carried out.

2. It was shown that copper-tungsten condensate is a laminated gradient material, the morphological features of which vary with an increase in tungsten content in it (from 0.63 to 32.98 wt.% in it).

3. Characteristics of the condensate strength during the test on tension are increased, and ductility decreases from 30.2 to 2.2 % with an increase of tungsten content from 0.63 to 32.98 wt.% in it.

4. Gravimetric analysis and microscopic examinations revealed that corrosion resistance of composite materials based on copper and tungsten is increased with an increase in tungsten concentration in the specimens from 0.63 to 32.98 wt.%.

REFERENCES

1. Zatovskyi, V.G., Khomenko, O.V., Khomenko, O.I. (2018) Modern powder composite materials for switching and welding equipment. In: *Transact. electric contacts and electrodes*. Kyiv, IPMS, NASU, **14**, 139–150 [in Ukrainian].
2. Grechanyuk, M.I., Grechanyuk, I.M., Zatovskyi, V.G., Grechanyuk, V.G. (2017) *Composite material for electric contacts and method of its realization*. Ukraine, Pat. 114451 [in Ukrainian]. https://sis.ukrpatent.org/media/INVENTIONS/2015/a201510758/published_description.pdf
3. Grechanyuk, N.I., Grechanyuk, V.G., Khomenko, E.V. et al. (2016) The new condensed from vapor phase composite materials based on copper and their applications. *Electrotechnica & Electronica (Bulgaria)*, **5–6**, 199–205. https://epluse.ceec.bg/wp-content/uploads/2018/09/20160506-34.pdf
4. Grechanyuk, N.I., Grechanyuk, V.G., Khomenko, E.V. et al. (2016) Modern composite materials for switching and welding equipment. Information 2: Application of high-rate vacuum evaporation methods for manufacturing electric contacts and electrodes. *The Paton Welding J.*, **2**, 34–39. DOI: https://doi.org/10.15407/tpwj2016.02.06
5. Bogdan, M., Marcin, H., Grechanyuk, I.N. et al. (2014) The actual state and prospects of a high power electron beam technology for metallic and non-metallic compositions used in electric contacts and electrodes. *Advanced Materials Research*, **875–877**, 1437–1448. DOI: https://doi.org/10.4028/www.scientific.net/AMR.875-877.1437
6. Grechanyuk, N.I., Minakova, R.V., Vasilega, O.P. et al. (2010) Modern state-of-the-art and prospects of application of technology of high-rate vacuum evaporation and subsequent condensation in vacuum of metals and nonmetals for producing of electric contacts and electrodes. Series: Composite laminated and gradient materials and coating. *Transact. of IMPS, NASU*, 54–67 [in Russian]. http://www.materials.kiev.ua/issue/39/article/462
7. Grechanyuk, N.I., Minakova, R.V., Grechanyuk, I.N. et al. (2014) Current state and prospects for application of a high power electron beam technology to produce metallic and nonmetallic components for electric contacts and electrodes. *Transact. of IMPS, NASU*, 233–245 [in Russian]. http://www.materials.kiev.ua/issue/72/article/1157
8. Denesenko, V.O., Minakova, R.V., Grechanyuk, V.G., Grechanyuk, I.M. (2008) Structure and physicochemical properties of composite materials based on copper and tungsten produced by electron beam evaporation method. *Nauk. Visnyk Chernivetskogo Un-tu*, **422**, 26–33 [in Ukrainian]. http://library.chnu.edu.ua/res//library/elib/visnyk_chnu/visnyk_chnu_2008_0422.pdf
9. Minakova, R.V., Grechanyuk, I.N., Bukhanovsky, V.V. et al. (2010) Structure, electric conductivity and mechanical characteristics of copper-tungsten composite obtained by electron beam physical vapour deposition (EB-PVD) technique. *Transact. of Famena*, 34(**2**), 37–46. https://www.scimagojr.com/journalsearch.php?q=20325&tip=sid
10. Bukhanovskii, V.V., Minakova, R.V., Grechanyuk, I.N. et al. (2011) Effect of composition and heat treatment on the structure and properties of condensed composites of the Cu–W system. *Metal Sci. and Heat Treatment*, 53 (**1–2**), 14–23. DOI: https://doi.org/10.1007/s11041-011-9334-x
11. Grechanyuk, N.I., Grechanyuk, I.N., Osokin, V.A. et al. (2008) Structure, physicochemical, mechanical, and operational characteristics of condensed composite materials of the Cu–W system for electric contacts. In: *Proc. of 8th Intern. Symp. of Croatian Metallurgical Society SHMD-2008 (June 2008, Sibenik, Croatia)*, 232.
12. (1980) *Unified procedure for laboratory tests of effectiveness of corrosion inhibitors in water systems*. Riga, I-t of Inorganic Chemistry, Litov. SSR [in Russian].
13. Geller, Yu.A., Rakhshtadt, A.G. (1983) *Materials science, methods of analysis, laboratory works and problems*. Moscow, Metallurgiya [in Russian]. https://www.twirpx.com/file/403315/
14. Chornovol, V.O. (2011) *Structure and corrosion resistance of Cu–Mo, Cu–W composite materials produced by electron beam evaporation-condensation*: Syn. of Thesis for Cand. of Tech. Sci. Degree [in Ukrainian].

ORCID

M.I. Grechanyuk: 0000-0002-2609-6018

CONFLICT OF INTEREST

The Authors declare no conflict of interest

CORRESPONDING AUTHOR

M.I. Grechanyuk
I.M. Frantsevich Institute for Problems of Materials Science of the NAS of Ukraine
E-mail: eltechmash@ukr.net

SUGGESTED CITATION

M.I. Grechanyuk, V.G. Grechanyuk, I.M. Grechanyuk, V.O. Chornovol (2022) Structure and corrosion properties of copper- and tungsten-based composite materials, produced by high-rate evaporation-condensation. *The Paton Welding J.*, **2**, 43–47.

JOURNAL HOME PAGE

https://pwj.com.ua/en

Received: 08.11.2021
Accepted: 31.03.2022

https://doi.org/10.37434/tpwj2022.02.08

CALCULATED ESTIMATION OF LOAD-CARRYING CAPACITY OF THE MAIN SPAN BEAMS OF THE E.O. PATON BRIDGE ACROSS THE DNIPRO IN KYIV BY NONDESTRUCTIVE TESTING RESULTS

O.O. Makhnenko, O.V. Makhnenko

E.O. Paton Electric Welding Institute of the NASU
11 Kazymyr Malevych Str., 03150, Kyiv, Ukraine

ABSTRACT

The paper deals with of the features of the design and loading parameters of the main longitudinal beams of the E.O. Paton Bridge across the Dnipro. It is shown that by the results of examinations, the welded joints are in a satisfactory condition, no inadmissible defects or fatigue cracks were detected in them, but rather considerable local corrosion damage appeared as a result of water flowing through the beam structures. The constructed finite element model of the main span beam was used to perform a calculated estimation of its loading and of the change of load-carrying capacity in the presence of local corrosion defects in the zone of the web and lower flange joint. Results of numerical modeling showed that the presence of these defects does not cause any significant increase of stresses in the span beam. Analysis of load-carrying capacity revealed that although the welded structure of the main span beams of the bridge has a rather high static strength margin under the action of normative distributed loading, presence of local corrosion defects of material discontinuity of rather large size considerably lowers the fatigue resistance of welded joints with detected defects that is dangerous in terms of span structure reliability and, therefore, requires immediate performance of repair operations.

KEY WORDS: bridge welded structure, main span beam, load-carrying capacity, corrosion defect, normative load, stressed state, numerical methods

INTRODUCTION

The Kyiv city E.O.Paton Bridge across the Dnipro, built and commissioned in 1953, is a unique engineering structure [1]. During its construction, the then advanced welding technologies were used, in particular those of mechanized submerged-arc welding. The bridge consists of 24 span structures of 58 m length in the non-navigable portion and 87 m length in the navigable portion, its total length is 1543 m. In the cross-section each of the bridge structures has four main longitudinal I-beams. The beam consists of a vertical web 3600 mm high and 14 mm thick and girths of different thickness from 30 to 80 mm at up to 1000 mm width (Figure 1, *a*). The beam web strength is additionally ensured by longitudinal and vertical stiffeners. In the 6-span structures in the bridge navigable part the height of the web above the intermediate supports was increased up to 6200 mm, due to adding the haunches (Figure 1, *b*). The beams are made from M16S carbon steel, which corresponds to VSt3sp (killed) steel by its characteristics.

During inspection of the main longitudinal beams of the bridge in 2020, it was determined [2] that the welded joints of the main beams are in a satisfactory condition, no inadmissible defects or fatigue cracks formed in them during long-term service. However, rather significant corrosion damage developed in the beam structure as a result of seepage of water from rain and thawing snow, particularly in the lower girths, lower horizontal ribs and in the lower parts of the webs, which is also due to accumulation of debris in these areas, which retains moisture. Through-thickness corrosion damage was detected in some trusses of the main beams (Figure 2).

In order to perform the calculated estimation of the load level, as well as of the change of the load-carrying capacity of the beam span structure in the presence of local corrosion defects, a geometrical and finite element model of the main 6-span beam was constructed, in keeping with the design documentation. The model 43.5 m long consists of one span, from the haunch middle to the middle of the span structure, under the condition of symmetry at both ends (Figure 3). Boundary conditions for displacement are assigned on the haunch reference plane, the vertical component of which is equal to zero that corresponds to the conditions of the span beam resting on the bridge supports.

The bridge load-carrying structures are designed for the action of continuous loading and unfavourable combinations of temporary loading, specified in Section 2 of SBN V.1.2-15.1.2 norms [3]. Calculations are made by the limit states in compliance with the requirements of 4.3 DNB V. 2.3-22:2009 [4]. In keeping with item 8.3.1 [4], the load from motor vehicles for each lane is assumed in the form of uniformly distrib-

Copyright © The Author(s)

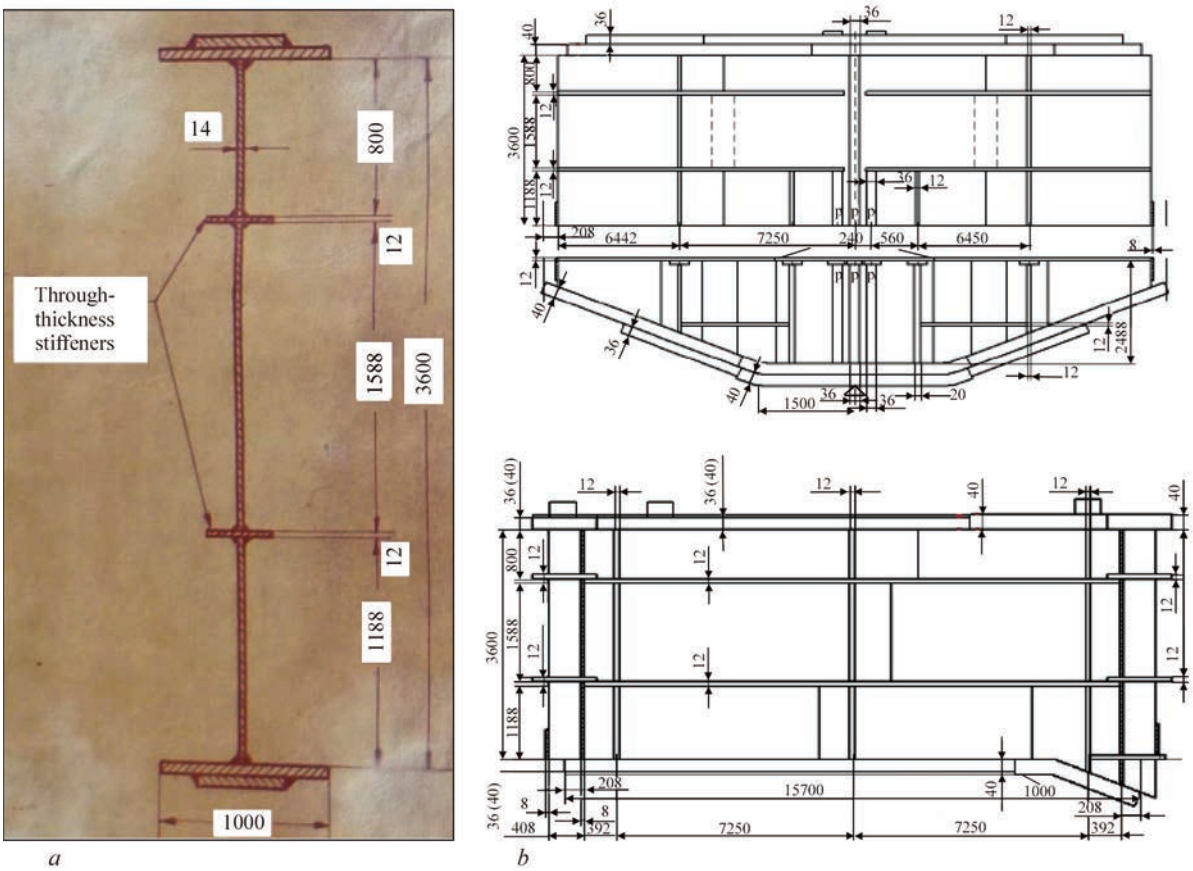

Figure 1. Transverse section of the main longitudinal I-beam (*a*) and drawings of fragments of the main longitudinal I-beam (*b*)

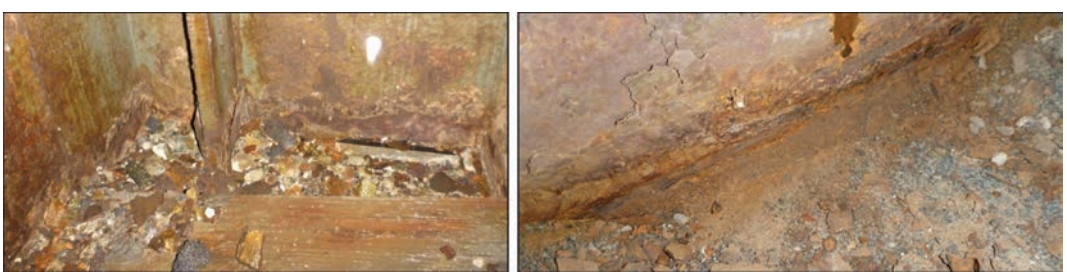

Figure 2. Ulcerative corrosion of the lower flange and the web in the span structure

uted load of intensity v = 0.98.K kN/m (0.1·K T/m), where K is the load class specified in keeping with 8.3.2 [3]. In the highways of categories I, II, III, in the main streets of general city significance, as well as in more than 200 m long bridges and roads of categories IV and V, K= 15. The E.O. Paton bridge has 6 lanes for passage of motor vehicles, so that the intensity of uniformly distributed load on the bridge is v = = 0.98·15·6 = 88.2 kN/m. Considering the presence of four main longitudinal beams in the bridge cross-section, in the developed model of 6-span beam a distributed load of magnitude P = 88.2 kN/m/(4·1 m) = = 22.05 kN/m^2 = 0.022 MPa is applied to the upper flange of 1 m width. The model also takes into account the force of the weight of the span beam structure as a constant load.

To determine the influence of typical corrosion damage of the beam in the zone of welded joint of the lower girth and the web, through-thickness discontinuities of metal 500 mm long were introduced into the finite-element model in different points along the lower girth (Figure 4) and the web (Figure 5).

Results of numerical determination of SSS in the 6-span beam showed that the longitudinal stress component prevails as a result of the action of a distributed force (0.22 MPa), applied to the upper flange. The maximum of longitudinal stresses, located in the up-

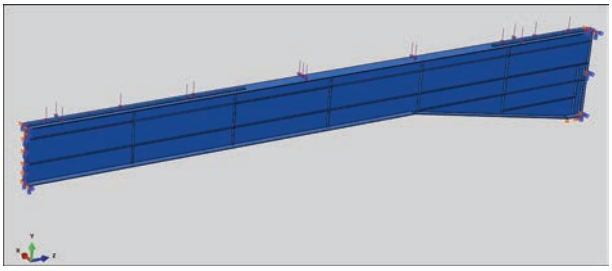

Figure 3. 3D model of the main 6-span beam

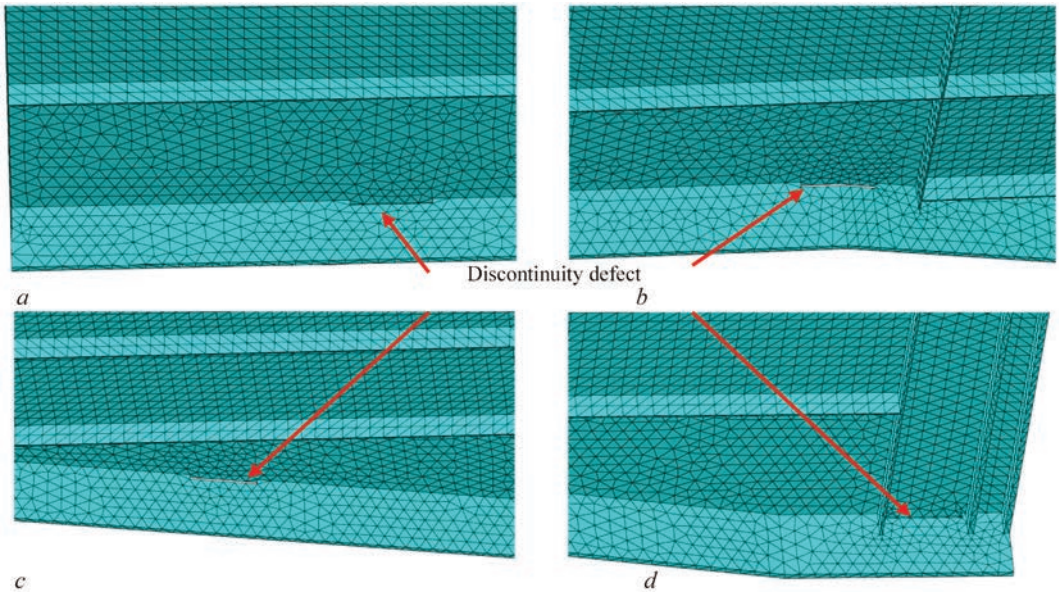

Figure 4. Discontinuity defects in the flange (local corrosion defect 500 mm long and 40 mm deep) in the zone of the joint of the web with the lower flange of the main 6-span beam: in the span central part (*a*); in the point of transition of the constant height beam into the haunch (through the thickness) (*b*); in the inclined part of the haunch (through the thickness) (*c*); in the central part of the haunch (*d*)

per girth above the haunch, does not exceed 65 MPa, and in the zone of the lower flange in the span central part it reaches 47 MPa (Figure 6). Presence of a local corrosion defect in this zone does not cause any significant increase of longitudinal stresses (maximum up to 50 MPa) (Figure 7).

Similar results of the influence of corrosion defects are presented also for other characteristic zones along the length of the 6-span beam, namely in the point of the haunch location and beam support, where the longitudinal tensile stresses change to compressive stresses in the lower girth zone (Figures 8–10). In the zone of transition of the constant height beam into the haunch (Figure 8), the level of maximum longitudinal stresses in the defectfree beam in the lower girth zone does not exceed 50 MPa, presence of the considered discontinuity defects causes an increase of the compressive stresses in the web up to 65 MPa (Figure 8, *a*), and in the flange in the zone of transition of constant height beam into the haunch the longitudinal compressive stresses decrease and become tensile stresses on the level of 20–37 MPa (Figure 8, *b*).

Vertical component of stresses is on a much lower level than the longitudinal component, and does not

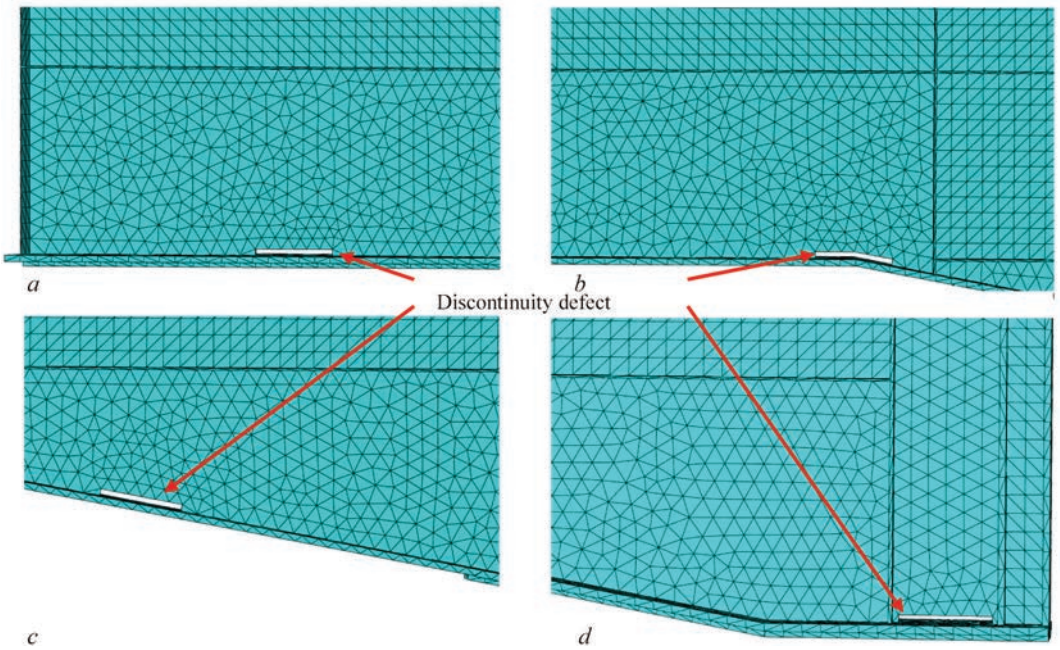

Figure 5. Through-thickness discontinuity defects in the web (local corrosion defect 500 mm long and 14 mm deep) in the zone of the joint of the web with the lower flange of the main 6-span beam: in the span central part (*a*); in the point of transition of the constant height beam into the haunch (*b*); in the inclined part of the haunch (*c*); in the central part of the haunch (*d*)

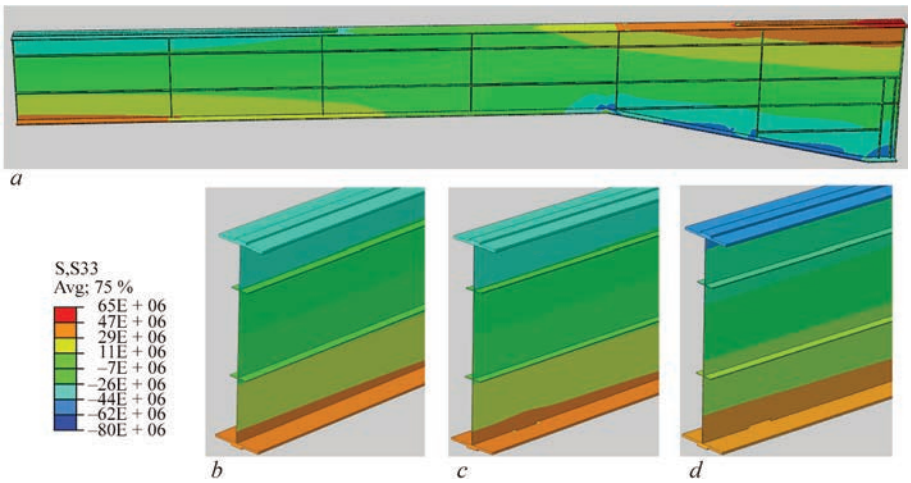

Figure 6. Distribution of longitudinal stresses over the span from distributed force (P = 0.022 MPa), applied to the upper flange: over the entire beam (*a*); in the central part without a defect (up to 34 MPa) (*b*); with a defect in the flange (up to 37 MPa) (*c*); with a defect in the web (up to 35 MPa) (*d*)

exceed 5 MPa in its greater part, and locally in the zone of transition into the haunch and in the support zone the vertical compressive stresses reach 20 MPa.

In the haunch inclined part (Figure 9) and in its central part (Figure 10) in the defectfree beam in the lower girth zone the longitudinal compressive stresses do not exceed 50 MPa. Presence of the considered discontinuity defects may lead to a slight increase of stresses in the web and the flange up to 55 MPa.

Thus, the welded structure of the main span beams of the E.O. Paton Bridge has a rather significant strength margin (not lower than 3) in the case of ac-

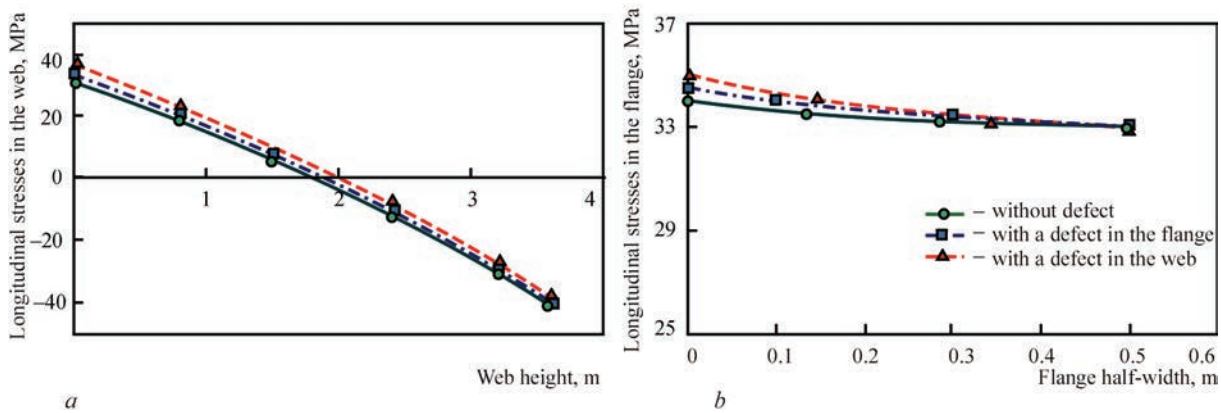

Figure 7. Distribution of longitudinal stresses in the central part of the span from distributed force (P = 0.022 MPa), applied to the upper flange, in a defectfree beam and beam with a local through thickness defect 500 mm long in the lower flange and the web: by the beam web height (*a*); by the lower flange width (*b*)

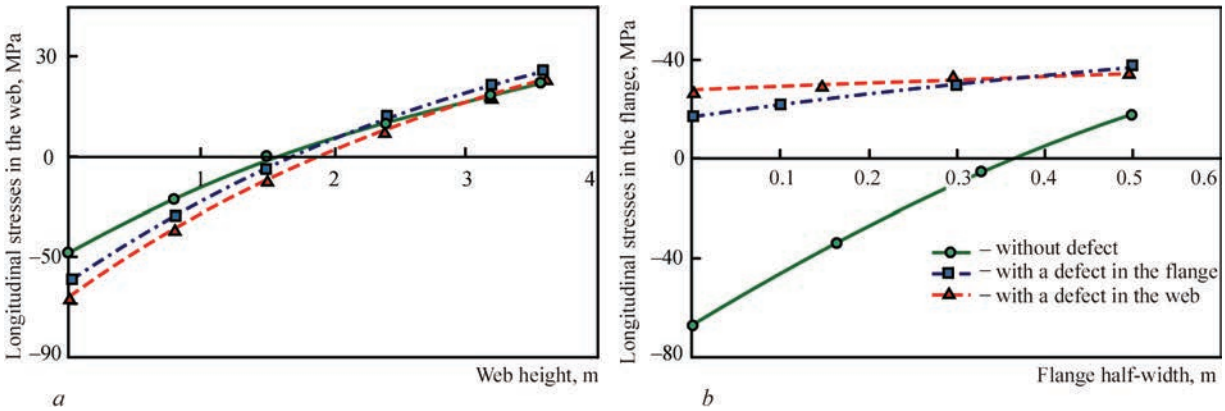

Figure 8. Distribution of longitudinal stresses in the zone of transition of constant height beam into the haunch from distributed force (P = 0.022 MPa), applied to upper flange, in a defectfree beam and beam with a local through-thickness corrosion defect 500 mm long in the lower flange and the web: by the beam web height (*a*); by the lower flange width (*b*)

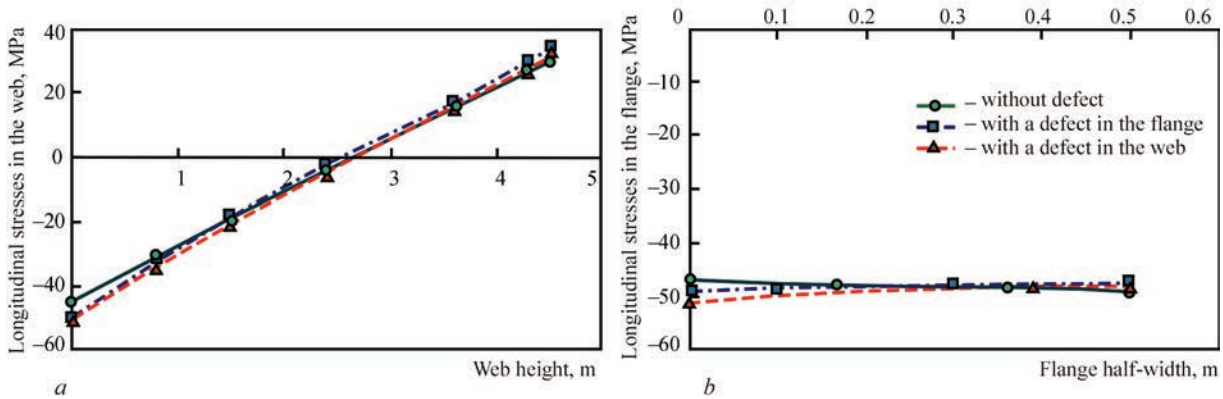

Figure 9. Distribution of longitudinal stresses in the haunch inclined part from distributed force (P = 0.022 MPa), applied to upper flange, in a defectfree beam and beam with a local through-thickness corrosion defect 500 mm long in the lower flange and the web: by the beam web height (*a*); by the lower flange width (*b*)

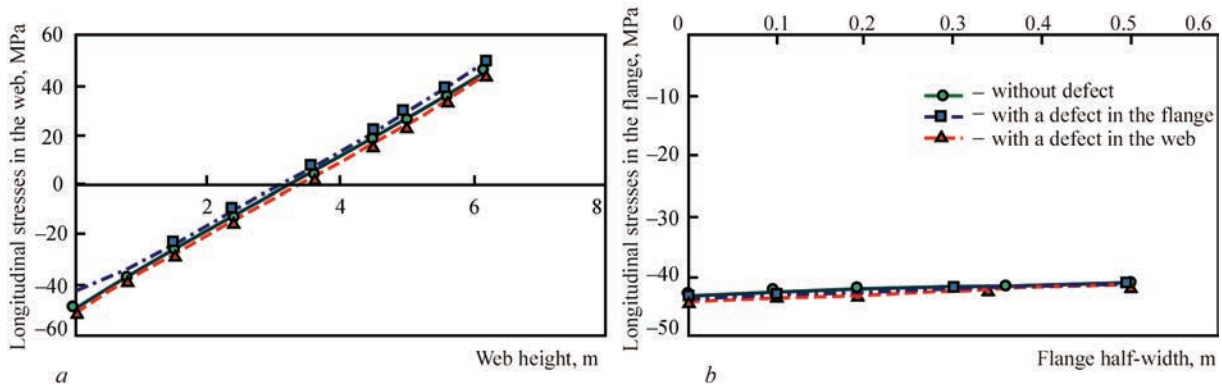

Figure 10. Distributions of longitudinal stresses in the haunch central part from distributed force (P = 0.022 MPa), applied to upper flange, in a defectfree beam and beam with a local through-thickness corrosion defect 500 mm long in the lower flange and the web: by the beam web height (*a*); by the lower flange width (*b*)

tion of the normative distributed load, applied to the upper flange of the I-beam. Presence of local corrosion defects of material discontinuity of a rather large size in the zone of the joint of the web and the lower flange (500 mm long and through-thickness) causes a slight change of the stressed state.

Strength of bridge structures should be considered under the impact of cyclic loads during long-term service. In keeping with IIW recommendations on assessment of welded structure fatigue resistance [5], the longitudinal continuous welded joint of the beam lower girth with the web with K-shaped groove produced by continuous automatic welding with NDT performance, can be assigned to class FAT = 125 MPa (No.312 in the Table 1), where FAT is the minimum range of nominal stresses. Thus, to ensure fatigue resistance to macrocrack formation after $2{\cdot}10^6$ cycles, the maximum admissible range of longitudinal stresses in the flange should not exceed 125 MPa. In the case of formation of through-thickness corrosion defects in the welded joint of the flange and the web, such a welded joint can be regarded as intermittent (No.324 in the Figure 11), for which the admissible range of longitudinal stresses decreases to 80 MPa and lower, in the presence of shear stresses.

Table 1. Classification of typical; elements of welded joints based on limiting range of normal stresses [5]

No.	Part sketch	Description	FAT, MPa	
			Steel	Aluminium
321	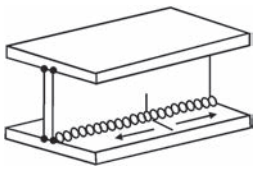	Longitudinal continuous welds with K-shaped reinforcement, automatic welding. No stops, NDT (stresses in the flange)	125	50
324	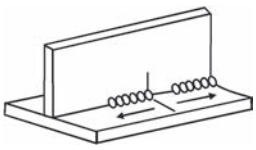	Longitudinal intermittent filler welds (normal stresses in the flange and shear stresses in the weld at the joint ends)		
		$\tau/\sigma = 0$	80	32
		0–0.2	71	28
		9.2–0.3	63	25
		0.3–0.4	56	22
		0.4–0.5	50	20
		0.5–0.6	45	18
		0.6–0.7	40	16
		> 0.7	36	14

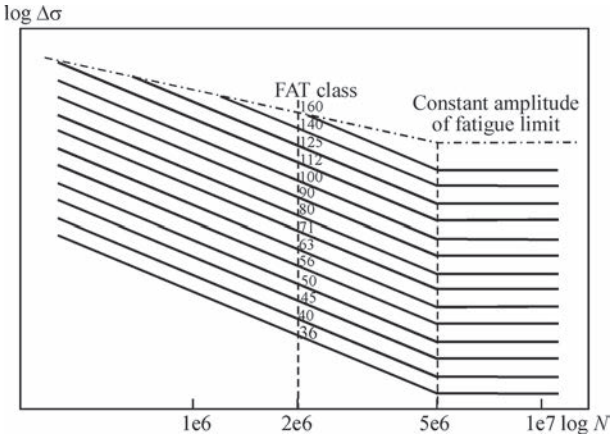

Figure 11. σ–*N* curves of fatigue resistance for different classes of welded joints (steel) for normal stresses [5]

Considering the rather long service life of bridge structures, it is rational to ensure such conditions that the effective stress ranges in the welded joints were below the endurance limit σ_{-1}, then the structure can be in service for an unlimited period of time. In keeping with σ–*N* curves (Figure 11) of fatigue resistance for different classes of welded joints for normal stresses [5], the endurance limit σ_{-1} for the considered welded joints is equal to:

- without defects (No.321, FAT = 125 MPa) σ_{-1} = = 92 MPa;
- in the presence of defects (No.324, FAT ≤ ≤ 80 MPa) $\sigma_{-1} \leq 57$ MPa.

Thus, in the defect free beam the maximum ranges of effective longitudinal stresses (up to 50–65 MPa) are much lower than the endurance limits of the welded joint of the flange and the web. Such a level of longitudinal stresses corresponds to the modern concepts of ensuring a sufficient fatigue resistance of defect free elements and components of welded bridge structures [6, 7]. In the presence of corrosion defects, the endurance limit of the welded joint of the flange and the web of the span beam is on the level or even below the effective ranges of longitudinal stresses from normative load.

CONCLUSIONS

Even though the welded structure of the main span beams of the E.O. Paton bridge has a rather significant static strength margin from the impact of normative distributed loading, applied to the upper flange of the I-beam, the presence of local corrosion defects of material discontinuity of a rather large size in the zone of the joint of the web and the lower flange essentially lowers the fatigue resistance of welded joints with detected defects that is dangerous in terms of reliability of the span structure and thus requires immediate performance of repair operations.

REFERENCES

1. Lobanov, L.M., Kyrian, V.I. (2013) The E.O. Paton all-welded bridge is sixty years old. *The Paton Welding J.*, **12**, 33–38.
2. Poznyakov, V.D., Dyadin, V.P., Davydov, Ye.O., Dmytrienko, R.I. (2021) Evaluation of damage of all-welded longitudinal main beams of the E.O. Paton bridge across the Dnipro river. *The Paton Welding J.*, **7**, 30–38. DOI: https://doi.org/10.37434/tpwj2021.07.06
3. (2009) DBN V. 2.3-22:201Kh: *Bridges and pipes. Basic design requirements.* Kyiv, Ministry of Regional Development of Construction, Housing and Communal Services of Ukraine [in Ukrainian].
4. (2009) DBN V.1.2-15:2009: *Bridges and pipes. Loading and effects.* Kyiv, Minregionbud Ukrainy [in Ukrainian].
5. (1996) *Recommendations for Fatigue Design of Welded Joints and Components*. IIW Doc. XIII-1539–96/XV-845–96.
6. Berthellemy, J. (2015) Maintenance of road bridges and road equipments optimized by a good fatigue design. Procedia Engineering, **133**, 255–264. DOI: 10.1016/j.proeng.2015.12.666.
7. (2005) EN *1993-1-9*: *Eurocode 3*: Design of steel structures. Pt 1–9: Fatigue.

ORCID

O.O. Makhnenko: 0000-0002-8583-0163,
O.V. Makhnenko: 0000-0003-2319-2976

CONFLICT OF INTEREST

The Authors declare no conflict of interest

CORRESPONDING AUTHOR

O.O. Makhnenko
E.O. Paton Electric Welding Institute of the NASU
11 Kazymyr Malevych Str., 03150, Kyiv, Ukraine
E-mail: makhnenko@paton.kiev.ua

SUGGESTED CITATION

O.O. Makhnenko, O.V. Makhnenko (2022)
Calculated estimation of load-carrying capacity of the main span beams of the E.O. Paton bridge across the Dnipro in Kyiv by nondestructive testing results. *The Paton Welding J.*, **2**, 48–53.

JOURNAL HOME PAGE

https://pwj.com.ua/en

Received: 11.10.2021
Accepted: 31.03.2022

Correction to:

https://doi.org/10.37434/tpwj2022.01.04

IMPROVEMENT OF THE MECHANICAL PROPERTIES AND CORROSION RESISTANCE OF LASER WELDS ON THICK DUPLEX PLATES BY LASER CLADDED BUTTERING

A. Straße, A. Gumenyuk, M. Rethmeier

Bundesanstalt für Materialforschung und -prüfung (BAM)
Unter den Eichen 87, 12205 Berlin, Germany

The Paton Welding Journal, No. 1, Pages 18–21 (2022).
The Original Article was Published on January 2022.

The original version of this article, unfortunately, contained an mistakes. Figures 5, 6, 7 were missing. The Figuress should look like the one below.

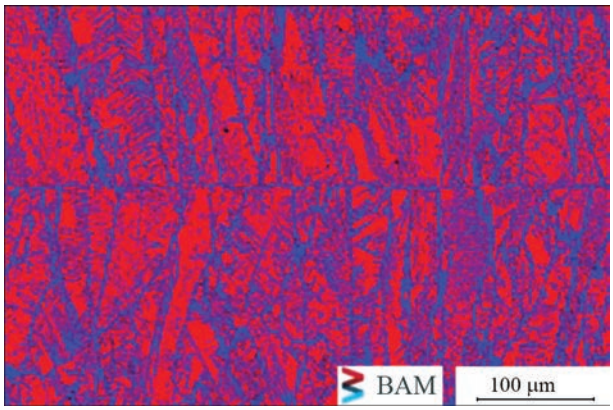

Figure 5. EBSD-analysis of weld seam with argon as root shielding gas (blue (light): austenite, red (dark): ferrite)

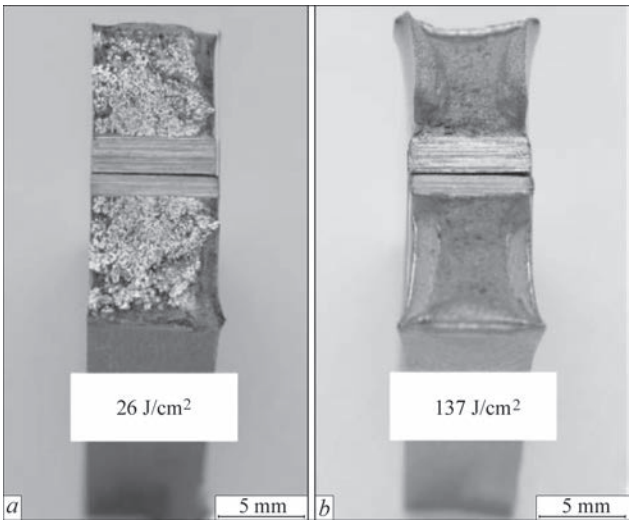

Figure 6. Broken impact testing specimen; with coated edges (*a*), without coating (*b*)

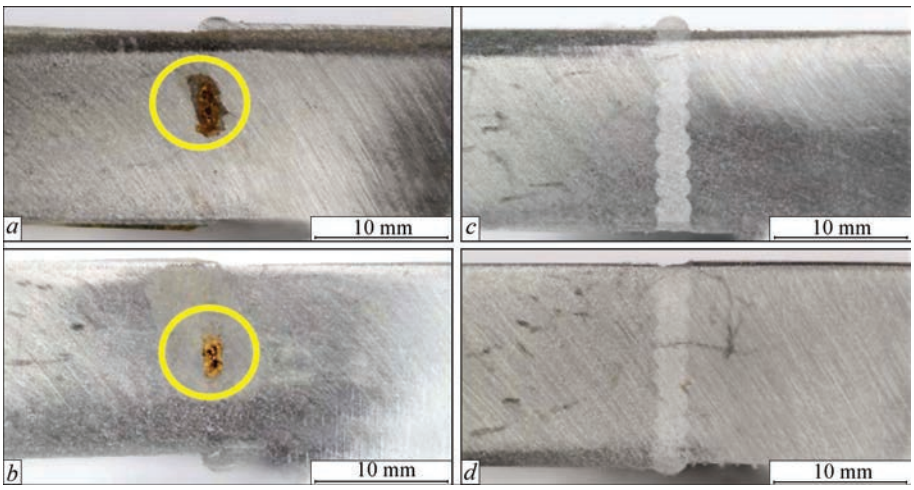

Figure 7. Corrosion specimens; without coated edges (*a*) and (*b*), with coating (*c*) and (*d*)